INSTITUTE OF PHYSICS
POLISH ACADEMY OF SCIENCES

Sergiy Trushkin

High-Pressure Spectroscopy of $ZnX:Cr^{2+}$ (X=S, Se, Te) Crystals and InP-based Multiple Quantum Wells

Ph.D. Thesis

Scientific advisor
Prof. dr hab. Andrzej Suchocki,
Institute of Physics
Polish Academy of Sciences

Warsaw 2010

Dedication

This Ph.D. Dissertation is dedicated to my Parents.

It is also dedicated to all my Close People and Friends, who were sincerely anxious for this Thesis to come into being, and heartened me greatly always and everywhere.

Podziękowania

Składam serdeczne podziękowania na ręce wszystkich osób, które przyczyniły się do powstania tej pracy.

Przede wszystkim, chciałbym szczególnie podziękować swojemu promotorowi, Panu prof. dr hab. Andrzejowi Suchockiemu za opiekę nad przebiegiem pracy, cenne wskazówki podczas wykonywania pomiarów oraz za owocne dyskusje w trakcie omawiania wyników. Jestem bardzo wdzięczny za to, że drzwi promotora były dla mnie otwarte.

Serdecznie dziękuję Pani dr Agacie Kamińskiej za wprowadzenie mnie w tajniki pomiarów wysokociśnieniowych, za niesamowitą życzliwość, bezcenne rady i wsparcie na każdym odcinku drogi przygotowania tej pracy doktorskiej.

Pragnę podziękować Panu dr Le Van Khoi z Zespołu Fizyki Półprzewodników $A^{II}B^{VI}$ ON.1.1 IF PAN za przekazanie badanych materiałów ZnSe:Cr^{2+} i ZnTe:Cr^{2+} oraz Panu prof. Markowi Hopkinsonowi z Uniwersytetu w Sheffield za udostępnienie struktur kwantowych InAsP/InGaP, InAsP/InGaAsP, InAsP/InP.

Jestem bardzo wdzięczny Pani prof. Irynie Sorokinie z Norweskiego Uniwersytetu Nauki i Technologii w Trondheim oraz Panu prof. Evgenijowi Sorokinowi z Uniwersytetu Technologicznego w Wiedniu za udostępnienie kryształu ZnS:Cr^{2+} oraz wsparcie mojego pobytu w Instytucie Fotoniki w Wiedniu.

Pragnę wyrazić swoją wdzięczność dla Świętej Pamięci Pana doc. dr hab. Sławomira Biernackiego za nieocenioną pomoc w interpretacji uzyskanych wyników pomiarowych na kryształach ZnX:Cr^{2+} (X=S, Se, Te) i opracowanie modelu teoretycznego opisującego uzyskane wyniki.

Panu prof. dr hab. Witoldowi Trzeciakowskiemu z Instytutu Wysokich Ciśnień PAN oraz Panu prof. dr hab. Grzegorzowi Karczewskiemu z IF PAN serdecznie dziękuję za życzliwe podejście i owocne dyskusje wyników eksperymentalnych dot. struktur kwantowych.

Badania, przedstawione w niniejszej rozprawie były przeprowadzone przy wsparciu Polskiego Komitetu ds. UNESCO (stypendium przeznaczony w 2008 r.) oraz Ministerstwa Nauki i Szkolnictwa Wyższego (projekt badawczy Nr N N202 204634). Jestem bardzo wdzięczny za pomoc finansową, która umożliwiła skończenie tej pracy.

Panu Mgr Krzysztofowi Kolwasowi z SL 2.2 IF PAN dziękuję serdecznie za bezwzględną pomoc w czasie spisywania tej pracy doktorskiej, jak również – za niezmierną życzliwość i Przyjacielskie wsparcie, na które zawsze mogłem liczyć w każdej sytuacji życiowej.

Dziękuję również moim licznym polskim znajomym i kolegom, którzy – w godzinach pracy i w czasach podróży, w momentach radości i smutku – zawsze stwarzali życzliwą atmosferę w moim otoczeniu oraz zawsze duchowo wspierali mój Naród i Kraj (Ukraina), z którego pochodzę. Nie wyobrażam sobie, żeby ta praca doktorska mogła powstać bez owego przyjaznego otoczenia.

Acknowledgements

I would like to express my deepest gratitude to all the persons, who contributed to the preparation of the present Thesis.

First of all, I especially acknowledge my Scientific Advisor, prof. dr. hab. Andrzej Suchocki for his continuous tutorship of the work progress, valuable guidance during the measurements and for the fruitful discussions of the results. I am grateful to my Supervisor for his door was open for me.

I would heartily thank dr Agata Kamińska from IF PAS, who initiated me into the details of the high-pressure measurements, for the amazing kindness, invaluable advice and support on every part of the way of this Ph.D. Thesis preparation process.

I am very gratitude to dr. Le Van Khoi from the Division of Physics of Semiconductors ON 1.1 of the IF PAS for the granting of the studied samples of ZnSe:Cr^{2+} and ZnTe:Cr^{2+}. I'm also grateful to prof. Mark Hopkinson from the University of Sheffield for the providing me with the quantum structures InAsP/InGaP, InAsP/InGaAsP and InAsP/InP.

My grateful acknowledgements – to prof. Irina Sorokina from the Norwegian University of Science and Technology in Trondheim and to prof. Evgeni Sorokin from the Vienna University of Technology for the granting of the ZnS:Cr^{2+} crystal and for the support of my visit to the TU Vien.

I would like to express my gratitude to the Blessed memory of dr. hab. Sławomir Biernacki for the invaluable assistance in the interpretation of the experimental results of the ZnX:Cr^{2+} (X=S, Se, Te) crystal studies and developing of the theoretical model, describing the observed results.

My frank acknowledgements to prof. dr hab. Witold Trzeciakowski from the Institute of High Pressures Physics PAS to and prof. dr hab. Grzegorz Karczewski from the IF PAS for the benevolent approach and fruitful discussions of the experimental results, concerned InP-based quantum structures.

The results, presented in this Thesis were realized with the financial support of the Polish National Commission for UNESCO (the scholarship was granted in 2008) and Ministry of Science and Higher Education (scientific project No. N N202 204634). I'm very obliged for the financial aid, which made it possible to complete this work.

I am very sincerely grateful to Mgr Krzysztof Kolwas from the SL 2.2 (IF PAS) for the reliable help in preparing of the manuscript of the Thesis as well as for the immeasurable favour and Friendly support, on which I could always count in every life situation.

I am also very thankful to my numerous Polish acquaintances and colleagues, who always – at business time or during the trips, at the moments of joy or sadness – invariably created a friendly atmosphere in my surrounding and always spiritually encouraged my Nation and Country (Ukraine). I can not imagine this Thesis could come into being without such a friendly support and invigoration.

CONTENTS

1. INTRODUCTION

1.1. Motivation

Cr^{2+}-doped II-VI semiconductors are of great interest and recently intensively studied because of their promising application for the mid-infrared easily-tuned laser sources. Such lasers can be applied in the construction of the detectors, being widely applied in the various branches of the economy. The coal-mining, security and environmental protection industries could undoubtedly benefit from the sensors, capable to determine explosive and environmental-polluting and substances. As the biological tissue has an absorption maximum at about 2.9 μm, tuneable coherent mid-infrared sources could be indispensable for the medical applications, such as surgery, ophthalmology and dermatology [1].

Furthermore, it was shown that in the case of the ZnS, ZnSe, CdSe crystals, doped with chromium ions, one can reach high slope efficiency between 2 and 3 μm. This spectral range is characterized with a lack of easily-used laser diodes [2].

The mentioned above applications resulted in the intensive investigations of the broad photoluminescence band centred at about 2.4 μm, peculiar to the Cr^{2+}-doped II-VI semiconductors and the theoretical treatment of the studied spectra. Generally, all observation were interpreted in the terms of the crystal field theory, extended to account the influence of various ligands (*S*, *Se* and *Te*) and including Jahn-Teller instability of the $^5T_2$ and ^5E terms [3,4]. The previously performed experiments can be quantitatively described by the use of the effective parameters in the assumed interaction spin Hamiltonian.

Subsequently, it turned out, that numerous studies of free Cr^{2+} ion energy levels in II-VI compounds revealed noticeable disagreement between the calculated and the experimental energy terms [4-8]. Furthermore, some parameters, obtained from the fit to the experimental spectra do not determine ambiguously the shape of the spectroscopic line. Moreover, they are not critically dependent on the band spectral position.

Consideration of the Trees correction, the spin polarization due to the Coulomb exchange energy in the partly filled 3d electronic shell [9,10], and the covalence effects [11,12] have improved the general agreement between theory and experiment, however, details of the crystal field terms structure are still not clear. Generally, the agreement between calculations and observations for the neighbouring configurations d^3 of the V^{2+} ion and d^5 of the Mn^{2+} ion is remarkably better than for the d^4 configuration of Cr^{2+}.

As far as there are some doubts remained, concerning the theoretical interpretation being in accord with experimental observations, there is a need to obtain an explanation, which includes the pressure dependence of luminescence structure.

High-pressure photoluminescence measurements, envisaged in the solution of the described above problems. Being carried out in the diamond anvil cell (DAC), the experiments presuppose by-turn focusing of the laser beam alternately on the studied sample and on the optical pressure sensor (tiny ruby balls). As the emitting ranges of the studied samples and the sensor do not coincide, the use of two different detecting systems is needed, which in-turn complicates the aligning process of the optical setup. Manufacture and calibration of new pressure sensor, being “tuneable”, more sensitive than ruby and operable in the mid-infrared spectral range is a challenge, which would significantly facilitate the realization of a wide group of high-pressure measurements.

1.2. Brief Thesis review

Chapter 1 "Introduction" presents the unsolved problems in the knowledge system about the optical properties of Cr^{2+}-doped II-VI semiconductors, which would be critical in the construction of the optoelectronic devices, being widely applied in the various branches of the economy. These problems motivated the author for the investigations, which, in turn, led to another substantial task: to calibrate a new, easily-manufactured and sufficiently sensitive pressure sensor for diamond anvil cell (DAC), which would be operable in the mid-infrared spectral range. The research motivations, following from the state-of-art challenges along with Theses review are briefly described in the "Introduction".

Chapter 2 "Fundamentals" covers the theoretical and empirical principles, necessary for the realization of the Thesis main tasks. As the knowledge of the origin of physical problems allows understanding their present-day challenges, a very brief historical sketch forestalls every subchapter.

Section 2.1 introduces to the adiabatic approximation as the basic principles for the vibronic interaction notion and subsequent formulation of the Jahn-Teller theorem. Pseudodegeneracy effect and electronic rearrangement phenomenon were qualitatively illustrated as two other cases of the adiabatic potential behaviour due to vibronic interactions. The shape of the adiabatic potential, commonly mentioned in the literature as "Mexican hat", was analyzed.

Section 2.2 reviews the ideas of the ligand field theory, illustrated by the example of Cr^{2+} ion, embedded in the tetrahedral field. The classification of the ligand field strength was introduced as its comparison with the spin-orbit coupling and correlation effects. Correlation diagrams illustrated the transition from weak to stronger ligand field, whereas Tanabe-Sugano diagrams were introduced as a convenient tool to interpret real optical spectra.

The energy structure of the Cr^{2+} ion was illustrated using the crystal field theory approach, with due regard to the spin-orbit coupling and Jahn-Teller distortion of both $^5T_2$ and ^5E terms. The quantum mechanics ideas were assumed as basis to obtain the relation between the spin-orbit coupling intensity of *S*, *Se* and *Te* ligand atoms.

The literature data on absorption and photoluminescent properties of Cr^{2+}-doped ZnX (X=S, Se, Te) crystals were reviewed. The explained nature of the PL spectra was analyzed to be taken into consideration for the further interpretation of the high-pressure studies of the appropriate samples.

Chapter 3 "High pressure research" is devoted to the study facilities and technical peculiarities, connected with the investigations of the solid state samples under high hydrostatic pressure.

Section 3.1 expands the theoretical inferences, concerning bandgap increase of the semiconductor crystals as well as energy level behaviour in the quantum wells under high pressure conditions.

Section 3.2 describes the diamond anvil cell (DAC) construction and principles of its operation.

Section 3.3 contains special technological peculiarities, which have been invented during the numerous high-pressure measurements and formulated as the generalized author's experience of the operation with the DAC. These methods are believed to be of especial profit for the newcomers in the high-pressure measurements.

Section 3.4 describes the features of the ideal pressure sensor and reviews the comparing characteristics of the pressure gauges, which were recently widely used. The experimental problems, led to the necessity to calibrate a new pressure sensor were formulated, and the first attempts to realize this idea were analyzed.

Chapter 4 "The aims of the research" specifies the main goals of the Thesis.

Chapter 5 "Samples" contains the growth parameters and detailed characterization of the studied samples.

Chapter 6 "Experimental results and discussions" describes the main outcomes of the Dissertation research.

Section 6.1 contains the results of the preliminary ambient-pressure absorption and photoluminescence (PL) measurements of the ZnX (X=S, Se, Te) crystals and InP-based multi quantum wells (MQWs).

Section 6.2 is devoted to the high pressure low-temperature studies of the PL band centered at ~0.6 eV, due to $^5E \rightarrow {}^5T_2$ transition of Cr^{2+} ions imbedded into ZnS, ZnSe and ZnTe crystal lattices. The changes of the PL band shape with pressure growth were explained in terms of Jahn-Teller effect and spin-orbit coupling, which intensity was found to increase with the ligand atomic number. The admixture of *Te* ligand wave functions into the Cr^{2+} central wave functions were found to be responsible for the significant difference of the ambient-pressure and high-pressre ZnTe:Cr^{2+} PL bands in comparison with those, obtained for Cr^{2+}-doped ZnS and ZnSe samples. It was also unambiguously confirmed, that the nature

of 1.25 eV PL band, observed in ZnSe:Cr^{2+} crystals was associated with $^3T_1 \rightarrow {}^5T_2$ transitions of Cr^{2+} ion.

Section 6.3 concludes the results of high-pressure studies of Cr^{2+}-doped ZnX (X=S, Se, Te) crystals.

Section 6.4 is devoted to the detailed ambient-pressure investigations of three InP-based MQWs: InAsP/InGaP, InAsP/InGaAsP and InAsP/InP.

First, on basis of ambient-pressure PL peak position, using the Vegard's low extension and the empirical formula proposed by M. Wada et al., the composition of InAs mole fraction was determined for each sample.

Second, ambient-pressure PL peak position of all the samples was found to change with temperature according to the dependency, proposed by K.P.O'Donnel and X.Chen, and exciton-phonon coupling model was found to be corresponding to the PL line width extension. The best operable temperature range for the possible pressure sensors was found to be (0–100) K.

Third, the ambient pressure PL was studied as a function of excitation power with the corresponding laser power density values (0.72–14.4) mW/cm^2. The investigation confirms, that non-radiative mechanisms in all the MQW samples are negligible, thus, they are good candidates for the pressure gauge for DAC.

Section 6.5 describes in detail the calibration process of new pressure sensors, which was aimed to obtain an explicit form of the calibration curve, valid for every InAsP-based MQW as a potential high-pressure guage. This process performed via the laborious high-pressure PL study of each MQW sample and stage-by-stage fitting processes, which were succeeded in developing of a calibration curve, common for all the samples in the whole temperature range (10–100) K.

It has been shown, that the use of the obtained calibration curve provide for very small (2.3%) relative error, whereas the sensitivity of the new-calibrated pressure gauges are 2-3 times higher than that of widely-used ruby pressure sensor.

Section 6.6 concludes the results of the MQWs research and the calibration process of new high pressure gauge for DAC.

Chapter 7 "Summary" resumes the main achievements of the Thesis.

Chapter 8 "References" contains the literature sources, which were referred in the Thesis.

2. FUNDAMENTALS

2.1. Vibronic interactions and Jahn-Teller effect

2.1.1. The adiabatic approximation

The physical properties of the molecular systems are determined by the motion and interactions of the nuclei and electrons. In the early thirties of the 20th century, just after the discovery of quantum mechanics, there were established the laws, governing such interactions and motions. But because of the mathematical difficulties in the description of quantum-mechanical systems, the treatment of the molecular structure could be carried out only with some simplifications. The most important of them was, *adiabatic (or, so-called, Born-Oppenheimer) approximation* [13,14].

The basic assumption was the following. Since a nuclear mass is about 2000 times greater than that of an electron, one can assume that every fixed position of the nuclei corresponds to a stationary electronic state. This assumption can allow us to solve the problem in two stages:

1. "To fix" the nuclei and to solve the electronic part of the problem.
2. To use the mean electronic energy (the adiabatic potential) for solution of the problem about the nuclei motions.

One has to notice, that a real solid state material can be represented by the assemblage of crystal cells with optical centers (dopant ions), embedded in a crystal lattice. Actually, the closest environment of the dopant ion consists of ligand ions, which are not static in the lattice, but have multitude of vibrating modes. At the same time one can limit the attention just to one representative vibrating mode, so-called "breathing mode", in which ligand ions pulsate radially "in and out" towards the central ion. This simple approximation turns out to be very important, as it makes possible to use only one nuclear coordinate, so-called *"configurational coordinate" Q*, which corresponds to the distance between the central ion and the ligand in the crystal [15]. This assumption will be used in the following rigorous approach of the solution of the Schrödinger equation.

First of all, one can write the total Hamiltonian of the atomic system as the sum of three components:

$$H = H_r + H_Q + V(r,Q), \tag{2.1}$$

where:

- H_r is the electronic component including in the kinetic energy of the electrons and the interelectronic electrostatic interaction;
- H_Q is the kinetic energy of the nuclei: $H_Q = -\sum \frac{\hbar^2}{2\mu_\alpha} \Delta Q_\alpha$;
- $V(r,Q)$ is the energy due to interaction of the electrons with the nuclei and internuclear repulsion (r and Q denote the whole set of coordinates of the electrons r_i, $i = 1, 2, \ldots, n$, and nuclei Q_α, $\alpha = 1, 2, \ldots, N$, respectively).

The operator $V(r,Q)$ can be expanded to a series of small displacements of the nuclei around the equilibrium point $Q_\alpha = Q_{\alpha_0} = 0$, which is chosen as a point of origin. In this case one can obtain:

$$V(r,Q) = V(r,0) + \sum_\alpha \left(\frac{\partial V}{\partial Q}\right)_0 Q_\alpha + \frac{1}{2}\sum_{\alpha,\beta}\left(\frac{\partial^2 V}{\partial Q_\alpha \partial Q_\beta}\right)_0 Q_\varepsilon Q_\beta + \ldots \qquad (2.2)$$

The first term of this expansion can be regarded as the potential energy of the electrons in the field of fixed nuclei. Then, one can solve the electronic part of the Schrödinger equation:

$$\left[H_r + V(r,Q) - \varepsilon_k^{'}\right] \varphi_k(r) = 0 \qquad (2.3)$$

and obtain a set of energies $\varepsilon_k^{'}$ and wave functions $\varphi_k(r)$ for the given nuclear configuration corresponding to the point Q_{α_0}.

But if the nuclei are displaced in the system, these solutions will vary. In order to obtain these changes, one has to solve the full Schrödinger equation:

$$(H - E)\Psi(r,Q) = 0\,, \qquad (2.4)$$

where the total function $\Psi(r,Q)$ can be expressed in terms of electronic functions $\varphi_k(r)$:

$$\Psi(r,Q) = \sum_k \chi_k(Q)\varphi_k(r) \qquad (2.5)$$

Here the expansion coefficients $\chi_k(Q)$ are the functions of the nuclear coordinates. Substituting (2.5) into (2.4), and making some transformations [16], one can obtain the following system of coupled equations for the functions $\chi_k(Q)$:

$$\left[H_Q + \varepsilon_k(Q) - E\right]\chi_k(Q) + \sum_{m \neq k} {}^{'}W_{k,m}(Q)\chi_m(Q) = 0\,. \qquad (2.6)$$

Here $W_{k,m}(Q)$ denotes the electronic matrix element of vibronic interactions, i.e., the part of the electron-nuclear interaction $V(r,Q)$, which depends on Q:

$$W(r,Q) = V(r,Q) - V(r,0) = \sum_{\alpha} \left(\frac{\partial V}{\partial Q_\alpha} \right)_0 Q_\alpha + \frac{1}{2} \sum_{\alpha,\beta} \left(\frac{\partial^2 V}{\partial Q_\alpha \partial Q_\beta} \right)_0 Q_\alpha Q_\beta + \ldots \qquad (2.7)$$

and $\varepsilon_k(Q)$:

$$\varepsilon_k(Q) = \varepsilon_k^{'} + W_{k,k}(Q) \qquad (2.8)$$

is the potential energy of the nuclei in the average field of the electrons in the state $\varphi_k(r)$.

From the coupled system of equations (2.6) it is clear, that if vibronic mixing of different electronic states can be ignored ($W_{km}(Q) = 0$ for $k \neq m$), the coupling in this system vanishes and the system of equations decomposes into a set of simple equations:

$$\left[H_Q + \varepsilon_k(Q) - E \right] \chi_k(Q) = 0. \qquad (2.9)$$

Each of these equations, for given k, represents the Schrödinger equation for the nuclei moving in the average field of the electrons in the state $\varphi_k(r)$. In other words, in this case the motions of the nuclei and electrons are separated and the problem can be solved in two following stages:

1. The electronic states $\varphi_k(r)$ are determined as solutions of equation (2.3) and by means of the equation (2.8) the nuclei potential energy $\varepsilon_k(Q)$ in these states is calculated.
2. Knowing the energy of nuclei $\varepsilon_k(Q)$, the wave functions $\chi_k(Q)$ and energy levels of the nuclei are determined by equation (2.9). In this connection the total wave function is:

$$\Psi(r,Q) = \varphi_k(r,Q)\chi_k(Q), \qquad (2.10)$$

where $\varphi_k(r)$ are the electronic functions for the static state, and $\chi_k(Q)$ are the vibrational wave functions in respect on the motions of the ions.

These are the main points of *the simple adiabatic approximation.*

Thus, it is clear, that the main requirement for the adiabatic approximation to be valid is to ignore the vibronic mixing of different electronic states in the equation (2.6). Meanwhile, it can be shown [17], that the perturbation of the total wave function by vibronic interactions is sufficiently small, when

$$\hbar\omega << \left| \varepsilon_m^{'} - \varepsilon_k^{'} \right|, \qquad (2.11)$$

where: $\hbar\omega$ is the energy of vibration quantum in the electronic state, taken into consideration; $\varepsilon_m^{'}$ and $\varepsilon_k^{'}$ are the mentioned above electron energy levels. Therefore, the inequation (2.11) can be considered as the *criterion of the adiabatic approximation*.

It was also shown, [18] that the solution of the Schrödinger equation (2.9) of one-coordinate dynamic center with eigenfunctions (2.10) leads to the potential energy curves, for the ground and excited states as it is shown in the Fig. 1. The represented dependencies are called a *configurational coordinate diagram.*

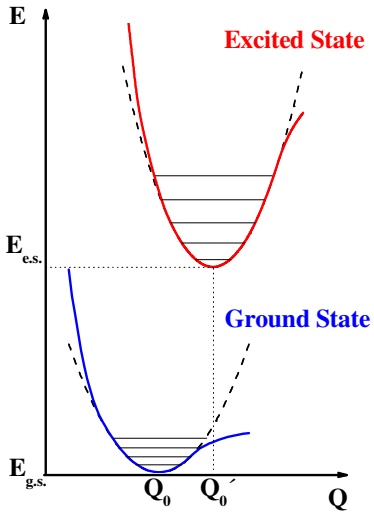

Fig. 1. The configurational coordinate diagram for an ion, embedded in the crystal lattice, oscillating as a breathing mode (after [15]). The broken curves are parabolas within the harmonic oscillator approximation. The horizontal full lines are phonon states.

The solid curves here stay for the interionic interaction potential energy, whereas the horizontal lines represent the set of permitted phonon states. It is remarkable, that the equilibrium position coordinates of the ground and excited states do not coincide: $Q_0 \neq Q_0^{/}$. Besides, at the distances, which are close to the equilibrium coordinates, the interionic potential curves $\varepsilon=f(Q)$ approach parabolic dependence due to *harmonic oscillator approximation*. This correlation can be shown rigorously.

It turns out, that one can choose the coordinates Q_α in such a way, that along with the additive dependence of the kinetic energy on the d^2Q_α/dt^2, the potential energy $\varepsilon(Q_\alpha)$ would also depend on the Q_α^2 additively [16]. These coordinates are called the *normal* ones. If a molecule has N atoms, then the number of vibrational degrees of freedom equals $3N-6$ or $3N-5$ (for linear molecules). Then, the normal coordinates equation (2.9) separates into $3N-6$ (or $3N-5$) equations of harmonic oscillators [19,20]:

$$-\frac{\hbar^2}{2M_\alpha}\frac{\partial^2\chi_{n_\alpha}}{\partial Q_\alpha^2}+\frac{1}{2}\omega_\alpha^2 Q_\alpha^2\chi_{n_\alpha}=E_{n_\alpha}\chi_{n_\alpha},\qquad \alpha=1,\ 2,\ ...,\ 3N-6, \tag{2.12}$$

where: M_α is the reduced mass of the αth normal vibration, and ω_α is its frequency. It is known, that E_{n_α} in this case can take the following values [17]:

$$E_{n_\alpha}=\hbar\omega_\alpha\left(n_\alpha+\frac{1}{2}\right),\qquad n_\alpha=1,\ 2,\ ... \tag{2.13}$$

It means that oscillator levels are changed only by the integer values, divisible by $\hbar\omega$. On the other side, ω_α is the eigenfrequency of the harmonic oscillations of the system with the potential energy, which has such a form: $\frac{1}{2}M_\alpha\omega_\alpha^2Q_\alpha^2$, i.e. it appears as the solution of the differential equation of such a form:

$$\frac{d^2Q_\alpha}{dt^2}+\omega_\alpha^2Q_\alpha=0 \tag{2.14}$$

Therefore, in order to find the frequencies of small oscillations of the multi-atom (multi-ion) system in the absence of electronic degeneracy, one has to solve the mechanical problem of the natural oscillations of the nuclei system with the potential interaction energy $\varepsilon(Q_\alpha)$, which can be approximated by a parabolic dependence.

2.1.2. The adiabatic potential and the Jahn-Teller theorem

In the same thirties of the 20th century, there were observed the most striking deviations from the adiabatic approximation. In 1934 L. D. Landau in a discussion with E. Teller [21] for the first time formulated the idea of instability and spontaneous distortion of the nuclear configuration in a molecule with an orbital electronic degeneration (term formed by two or more orbital states with the same energy). Later this idea was verified by Jahn and Teller for all non-linear molecular systems, and was published in 1937 [22], being called in the literature the Jahn-Teller (J.-T.) theorem.

Before the theorem to be rigorously formulated, one should imagine that in the presence of Jahn-Teller effect electrons do not follow the motion of the nuclei adiabatically. And the nuclear states are determined not only by the average electric field of the electrons, but also by the details of the electronic structure and its changes under nuclear displacements.

The resulting complicated binding between the electronic and nuclear motions is the first essential deviation from the adiabatic approximation. From the theoretical point of view, the stationary electronic states are obtained as solutions of the Schrödinger equation for the fixed nuclei. But taking into account in the Hamiltonian the terms of so-called *vibronic interactions* (interaction of electrons with nuclear displacements), one can conclude about the mixing of the electronic states. This mixing is the starting point in the analysis of the properties of the molecular compounds.

The electronic part of the Schrödinger equation (2.3) contains the function $\varepsilon_k'(Q)$, which is the mean kinetic energy of the electrons at fixed nuclei positions plus interaction energy between nuclei. This term has a meaning of nuclei potential energy and is called *adiabatic potential*. If there is no electron degeneration, this function usually has one absolute minimum, which corresponds to the stable nuclei configuration: $Q_\alpha = Q_\alpha^0$. As it was shown in the previous section, near this minimum the function approximates rather well to the quadratic dependence on Q_α.

Meanwhile, if the electron degeneration is present, the adiabatic potential will be illustrated by the configurational coordinate diagram, different from that presented in Fig.1. The way to study the form of the adiabatic potential can be the following. One can assume, that while solving the electronic equation (2.3) for some symmetric nuclei configuration, described by the point Q_α^0 (α=1, 2, …, N), there obtained two coinciding values of the adiabatic potentials are obtained: $\varepsilon_1(Q_\alpha^0) = \varepsilon_2(Q_\alpha^0)$. These values correspond to two electronic functions Ψ_1 and Ψ_2. In order to study the behaviour of the adiabatic potentials near the point Q_α^0, one can expand the interaction energy between the nuclei and the electrons $V(q, Q_\alpha)$ into a series with a little displacements near the Q_α^0 point:

$$V(r,\ Q_\alpha) = V(r,\ Q_\alpha^0) + \sum\left(\frac{\partial V}{\partial Q_\alpha}\right)_0 \left(Q_\alpha - Q_\alpha^0\right) + \frac{1}{2}\sum\left(\frac{\partial^2 V}{\partial Q_\alpha^2}\right)_0 \left(Q_\alpha - Q_\alpha^0\right)^2 + \ldots \qquad (2.15)$$

If the nuclei are immovable, one can consider only the first term $V(r,\ Q_\alpha^0)$ in the series (2.15) for the solution of the electron equation (2.3). Meantime, if the nuclei displacements are present, one can consider the influence of the further terms as a small perturbation.

It is clear, that if the adiabatic potential has a minimum in the Q_α^0 point, the derivative

$\left(\frac{\partial E}{\partial Q_\alpha}\right)_0 = 0$ and $\varepsilon(Q_\alpha)$ does not contain the linear displacement terms $Q_\alpha - Q_\alpha^0$. This is possible, when all matrix elements of the linear terms of the expansion (2.15), expressed with the wave functions Ψ_1 and Ψ_2 are equal to 0. To put it differently, if at least one of the matrix elements

$$\int \Psi_1^* \left(\frac{\partial V}{\partial Q_\alpha}\right)_0 \Psi_2 d\tau \qquad (\alpha=1, 2, \ldots) \tag{2.16}$$

is not equal 0, then the adiabatic potential $\varepsilon(Q_\alpha)$ in the Q_α^0 point has no minimum.

Jahn and Teller have shown for the first time [22], that for each polyatomic system in the presence of electron degeneration in the non-linear symmetric configuration of nuclei, there will always be such nuclei displacements Q_α, for which the integral (2.16) does not equal 0. It means, that in the point Q_α at least one of the branches of the adiabatic potential has no minimum. It was later shown by Jahn [23], that a similar statement is also valid in the case of spin degeneracy (with the exception of two-fold degeneracy) for the Kramer's systems [24]:

The statement about the absence of the extrema at the point of degeneracy is called Jahn-Teller theorem and may be formulated more rigorously as follows: ***if the adiabatic potential of a nonlinear polyatomic system has several (f>1) sheets coinciding in one point (f-fold degeneracy), at least one of them has no extremum at this point, with the exception of Kramers degeneracy cases.***

The schematic illustration of this statement is presented in Fig. 2. Here at the point Q=0, which corresponds to the maximum symmetric nuclear configuration, two branches of the adiabatic potential coincide, resulting in electron degeneracy. But according to the Jahn-Teller theorem, the adiabatic potential in this point has no minimum, hence, the system in this point is not stable. At the same time, if the atomic system is stable in principle in this studied electronic state, the minima of the adiabatic potentials are situated in the points $Q = \pm Q_1 \neq 0$. At these points the system has a lower energy, the nuclear configuration has a lower symmetry, the adiabatic potential as a whole has a new shape and, thus, the solid state material has a series of new properties.

One has also take into account, that besides of Jahn-Teller effect the vibronic interactions have two other cases [25].

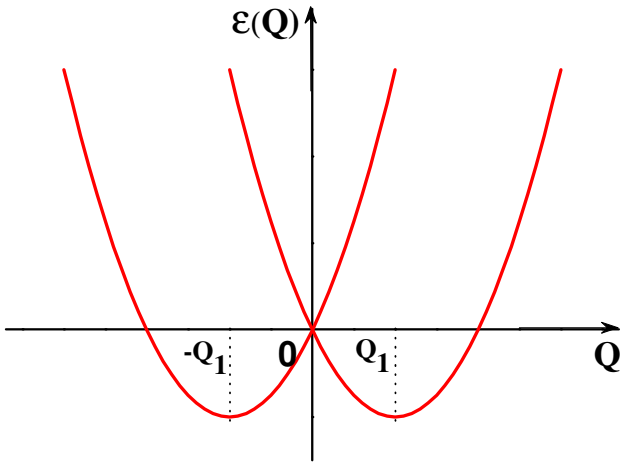

Fig. 2. Schematic illustration of the adiabatic potential behaviour due to Jahn-Teller effect.

1. Pseudo Jahn-Teller effect occurs, when at Q=0 point the direct crossing is removed by some term interaction. As a result, the branches of the adiabatic potential do not cross, but "pseudocross", as it is marked by dotted line in Fig. 3(a). In this case the structure of the molecule is "softened" in the ground state, but still is not stable. Though, in a strong limit the system is unstable at Q=0 and has two minima of the adiabatic potential at $Q = \pm Q_1 \neq 0$, like in the case of Jahn-Teller effect.

2. The variation of the adiabatic potential is present at long distances due to Jahn-Teller effect or electronic rearrangement (Fig. 3(b)). In the general case, these changes of the adiabatic potential, especially in the case of electronic rearrangement, lead to the change of

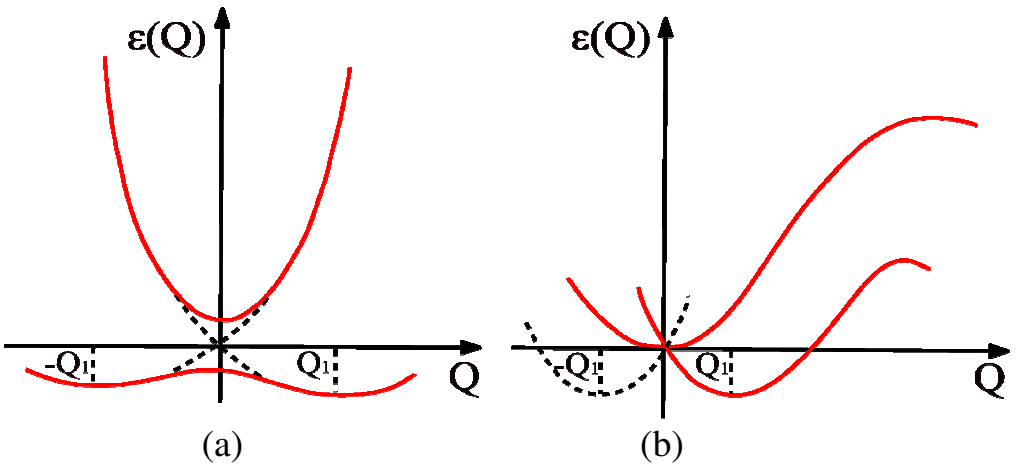

Fig. 3. Schematic illustration of the adiabatic potential behaviour due to vibronic interaction:
a) electronic pseudodegeneracy – pseudo-Jahn-Teller effect;
b) electronic rearrangement effect.

equilibrium nuclei configuration, rigidity (force constants), anharmonicity, and, as a result, the chemical reactivity of the material.

The variety of the effects and laws, revealed by the vibronic approach, made possible to describe and predict a series of stereochemical and spectroscopic properties of the solid state materials.

The corollary of the Jahn-Teller theorem is the fact, that at the point of the nuclear configuration, where electronic state is degenerated, the surface of the potential energy of nuclei has no minimum. Meanwhile, the knowledge of such minima positions (in the presence of Jahn-Teller effect) could give us the substantial information about the stable configuration of the nuclei, their dynamics, and energy spectra. In the literature the study of the adiabatic potential shape is widely illustrated by the example of metal-ligand ML_6-type octahedral complexes.

It is known [26], that ligand atoms influence the central ion, what leads to the splitting of its energy terms. (This matter will be discussed more detailed in the 2.2.1 Section). In the octahedral system such splitting results in the creation of the doubly degenerated *E*-term and trebly degenerated T_2 term, characterized by higher and lower energies correspondingly. The degeneracy or the energy terms can be relieved with the so-called symmetrized displacements which are not connected with the forward and rotary movement of the complex as a single whole. The theoretical calculations show [22,27,28], that in the case of *E*-term, the degeneracy can be relieved via the symmetrized displacements of *e*-type, and such a situation is usually mentioned as $E \otimes e$ case in the literature. The e-type displacements can be expressed by Q_2 and Q_3 normal mode coordinates (Fig.4 (a)), which, in turn, are connected with the Cartesian coordinates via the expressions, presented in the Table 1.

J.H. Van Vleck has shown first [27], that the adiabatic potential of *E*-term can be expressed by the following equation:

$$\varepsilon(Q_2, Q_3) = \frac{1}{2} K(Q_2^2 + Q_3^2) \pm |A| \sqrt{Q_2^2 + Q_3^2} \tag{2.17}$$

In order to analyze the shape of this surface, it is convenient to use the polar coordinates ρ and φ:

$$Q_2 = \rho \sin\varphi, \; Q_3 = \rho \cos\varphi \tag{2.18}$$

Then,

$$\varepsilon(\rho, \varphi) = \frac{1}{2} K\rho^2 \pm |A|\rho \tag{2.19}$$

The latter equation shows, that ε doesn't depend on φ. The shape of this surface of rotation is shown in Fig.4 (b) and is called "mexican hat".

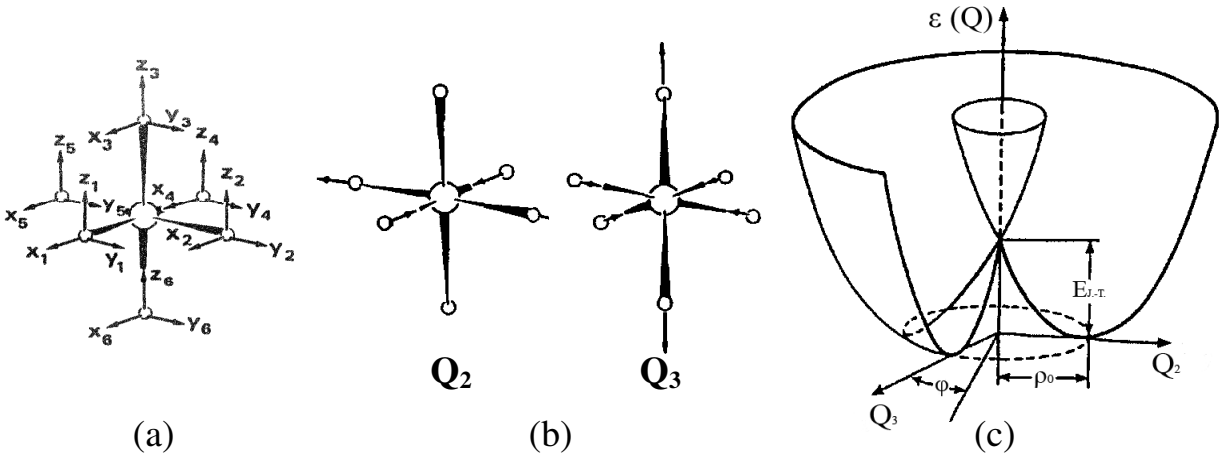

Fig. 4. The labeling of Cartesian displacements (a); the shape of symmetrized displacements of atoms Q_2 and Q_3 in an octahedral complex ML_6 (b); and the"mexican hat"-type adiabatic potential shape for a doubly degenerated *E* term linearly interacting with the e-type displacements, described by Q_2 and Q_3 coordinates (c).

The point Q_2=Q_3=0 is the cross point of the inner and exterior branches of the surface of revolution, presented in Fig. 4 (b), and its minima is the circle with a radius of $\rho_0 = |A|/K$, which is located at a "depth" of Jahn-Teller energy $E_{J.-T.} = A^2/2K$.

One has to notice that the foregoing conclusions about the shape of the adiabatic potential can be obtained, if one takes into consideration only the first two terms in the expansion (2.15). Meanwhile, it was shown [29-32] that if one takes into account the quadratic terms as well, the form of the adiabatic potential will change. Along the bottom of the "mexican hat" 3 "wells" will occur, regularly alternating with three "humps" as it is shown in Fig. 5.

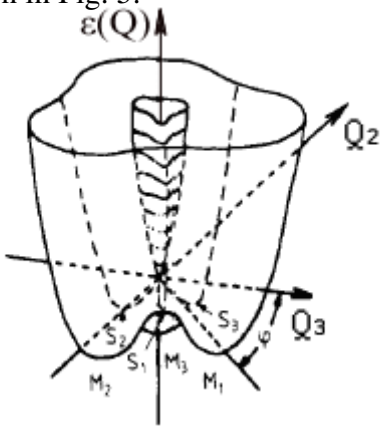

Fig. 5. The distorted "mexican hat" adiabatic potential surface with three minima M_i and three saddle points S_i, where $i = 1,2,3$ (after [34]).

Table 1. Symmetrized displacements, expressed via Cartesian Coordinates labeled as shown in Fig. 4(a) [33].

Sym-metrized coordinates	Sym-metry type	Transfor-mation properties	Expression in Cartesian coordinates
Q_2	***e***	$\sqrt{3}(x^2-y^2)$	$\frac{1}{2}(x_1-x_4-y_2+y_5)$
Q_3		$2z^2-x^2-y^2$	$\frac{2z_3-2z_6-x_1+x_4-y_2+y_5}{\sqrt{12}}$

2.2. Cr^{2+} ion in the tetrahedral field of ligands.

2.2.1. The main ideas of the ligand field theory

By the end of the 30's it had been clear, that the electrostatic ideas could not completely describe the atomic interactions in the coordination compounds and conformably explain a wide range of magnetic and optical material properties. Thus, a new approach of the crystal bounds, based on the quantum mechanics laws was developed by Bethe in 1929 [26]. He studied the influence of the surrounding ions on the electron distribution within any of the ions in a NaCl-type lattice. Later on the principles of this work were recognized by Penney, Schalp [35,36] and van Vleck [37] to describe the spectral and magnetic properties of the transition metal complexes. These ideas served as a basis for the formation of so-called, *crystal field* and *molecular orbital theories*, which tried to describe the bounds, arising between the atoms or ions in the complex compounds. Later on, being enriched with the conclusions of the two above mentioned theories, a new, more general and adequate conception about the processes in the complex compounds was created and called *ligand field theory*. It covers all the aspects concerned the influence of the nearest neighbours on the physical properties of the atom or ion, located in the center of the coordination compound.

The main assumptions of the ligand field theory can be formulated as follows [38].

1. While considering the orbital energies, the contribution of both electrostatic field of ligands and covalence effects have to be taken into account.
2. If the electrons are located on molecular orbitals, similar to *d*-ones, then the real molecular orbitals are substituted by the *d*-orbitals, with a somewhat modified radial term $R_{nd}(r)$.

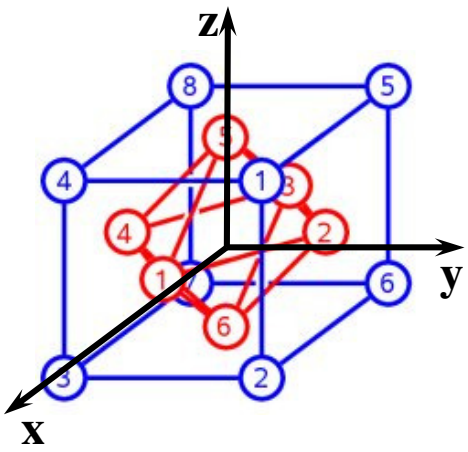

Fig. 6. A schematic illustration of ligands in the octahedral ML_6-type complex.

In the present section there will be reviewed the ideas of the ligand field theory, which mainly refer to the transition metals. One should notice that ligand field perturbations for the 3*d*-electrons of transition series is greater than, for example, in the case of 4*f*-electrons of rare earth atoms. The latter peculiarity is

explained by the fact that 3*d*-electron orbitals are not protected by the shield of exterior electrons, as it takes place in the case 4*f*-electrons, which are screened with 5*s*- and 5*p*-electrons. In the isolated free transition metal ion all five *d* atomic orbitals have the same energy, i.e. the *d*-orbital level is quintuply degenerated and forms fivefold degenerated ^2D-term. But in the complex compounds the presence of ligand ions around the central one leads to the symmetry decrease, which results in the splitting of the degenerated states. The case, which is widely discussed in the literature and vividly illustrates the perturbation process of the central ion is octahedral (O_h) ligand configuration. There are six ligand ions (shown with red color in Fig. 6) disposed on the apices of the octahedron which is inscribed in the cube. Then, if the Cartesian coordinate system is chosen as it is shown in the picture, the directions of the $d_{x^2-y^2}$ and d_{z^2} orbitals of the central ion have their electron density maxima oriented directly towards the ligands. At the same time d_{xy}, d_{yz}, and d_{xz} orbitals have their density maxima oriented in the regions between the Cartesian axes. Thus, the $d_{x^2-y^2}$ and d_{z^2} orbitals are affected by the ligands more than the d_{xy}, d_{yz}, d_{xz} ones, and therefore five *d* states in the octahedral free ion are split into doubly degenerated e_g state (*E*-term) and triply degenerated t_{2g} state (T_2-term) with higher and lower energies, respectively.

Since the experimental part of the Theses mostly discusses the materials with tetrahedral (T_d) configuration of ligand ions, it should also be expedient to illustrate the splitting of the *d* orbital energies in this case.

First, one has to take into account, that a regular tetrahedral can be obtained by taking alternate apices of a cube (ions, shown with blue color and marked as 1, 3, 6, 8 in Fig.6). Then, the orbitals of t_2 set are directed towards the centers of the cube edges, and the *e* set orbitals are directed towards the cube face centers. Moreover, the close inspection shows, that in this case t_2 orbitals spread closer to the ligand ions in comparison with *e* orbitals. Thus, as it follows from the rigorous calculations [16], *in the tetrahedral complexes e and* t_2 *sets are reversed with respect to the splitting in the octahedral ligand configurations* (Fig. 7). As it is shown in Fig. 7, the separation between d_{e_g} and $d_{t_{2g}}$ orbitals is equal to $10Dq$ (often abbreviated as Δ), where Dq is so-called crystal field parameter, being the product of two components [18,39]:

$$D = \frac{35Ze}{4a^5} \quad \text{and} \quad q = \frac{2e\langle r^4 \rangle}{105}. \tag{2.20}$$

Here Ze is a central ion charge, a is the distance between the central and ligand ions, and $\langle r^4 \rangle$ is the mean fourth power radius of the d electrons of the central ion. As it my be seen from the picture (Fig. 7), crystal field parameter is different in the case of octahedral and tetrahedral configuration, and it was shown rigorously [18], that

$$Dq_{octahedral} = -\frac{9}{4} Dq_{tetrahedral} . \qquad (2.21)$$

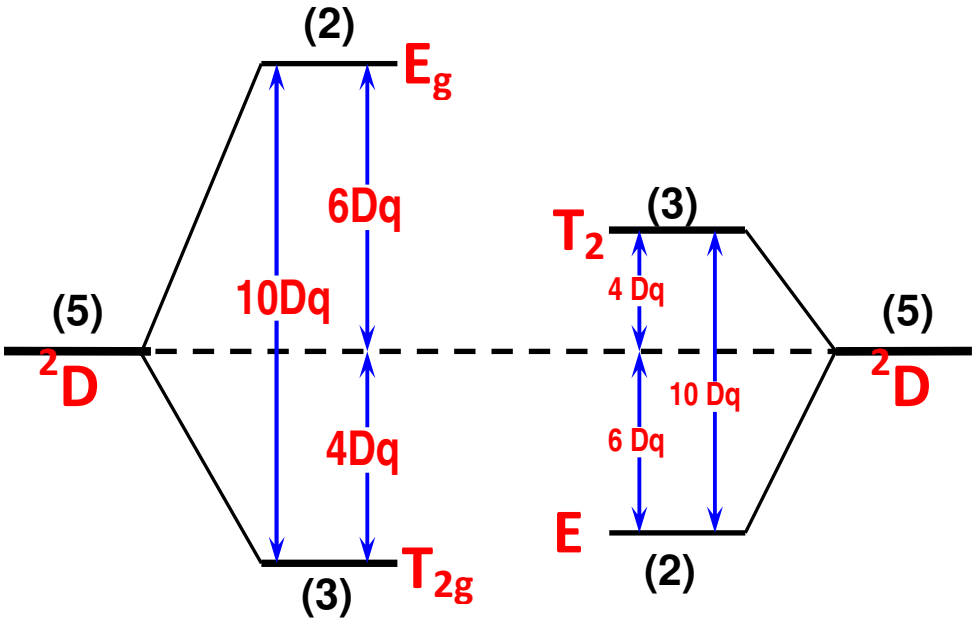

Fig. 7. The splitting of the energies of the *d* orbitals by octahedral (left) and tetrahedral (right) crystal fields.

It is essential to mention, that the energy of the quintuply split ^2D-term in the ligand surrounding is E_0 value higher in comparison with the free ion case. The E_0 energy is obtained by the central ion electrons due to the interaction with the negative ligands and in consequence of the attraction of ligand electrons to the positive core of the central ion. It can be shown [16], that E_0 energy coincides with the position of the term of the central ion in the field of ligands, located in a spherically symmetrical positions. This energy is also used as a level from which the position of the split terms is counted out, thus, it is called a "center of gravity" of the split levels (marked with a dashed line in Fig. 7). In the octahedral and tetrahedral configurations the E-terms and T-terms are $6Dq$ and $4Dq$ distant from the center of gravity respectively, but in accordance with (2.21) they are located on its opposite sides.

If the central ion has more than one d-electron over the closed electron shell, the interaction between d-electrons becomes significant and, in this case four following situations are possible [16,39]:

1. The ligand field influences on the *d*-electrons much weaker in comparison with the spin-orbit interaction, what can be expressed with the following inequation:

$$\hat{H}_{LF} < \lambda \vec{L}\vec{S},$$

where $\vec{L}$ is the operator of random orbital angular momentum of atom and $\vec{S}$ is the operator of random spin momentum of electron respectively. In this case the atomic terms of the central ion undergo just some perturbation from the ligands and this case is called *a weak field approximation.*

2. The inter-electronic repulsion causes the splitting of the terms as large as ligand field influence. In this case so-called *medium field approximation* is considered:

$$\hat{H}_{LF} \approx \lambda \vec{L}\vec{S}$$

3. The influence of ligand field exceeds the electrostatic interaction between *d*-electrons and their orbital bounds are being broken. The ligand field is stronger than spin-orbit coupling and weaker than correlation effects (intra-atomic exchange interactions):

$$\lambda \vec{L}\vec{S} < \hat{H}_{LF} < \hat{H}_{corr.\ ef.}$$

The terms of the central ion do not exist in this case and it is said about *strong field approximation.*

4. The interaction of the central atom and the ligand field are characterized by the energy, comparable with that of correlation effects, and significantly exceeds the spin-orbit coupling energy:

$$\lambda \vec{L}\vec{S} << \hat{H}_{LF} \sim \hat{H}_{corr.\ ef.}$$

This is *a very strong field approximation* case, which it is characterized by break-down of the Hund's rules and release of some electrons from 3*d* shell.

The case of Cr^{2+} ion, embedded in the field of sulphur, selenium and tellurium ligand atoms can be considered in the context of medium field of ligands.

The study of the optical properties of crystals at high pressures makes it necessary to know the change of energy levels with interatomic distance decrease, i.e. with the ligand field increase. The behavior of energy levels under above mentioned conditions can be pictorially represented by so-called correlation diagrams. On the basis of representation theory of the symmetry group it was shown [18] that the term splitting for the $3d^n$ system in O_h symmetry and for the $3d^{10-n}$ system in T_d symmetry are equivalent. Thus, *the diagrams for the $3d^n$ case in*

O_h symmetry are approximately valid for the $3d^{10-n}$ case in T_d symmetry and vice versa. Fig. 8 represents the correlation diagram for $3d^4$ case in T_d configuration [39]. The scale on theextreme left and right sides of the diagram is rough and does not represent the true energy distances between the terms.

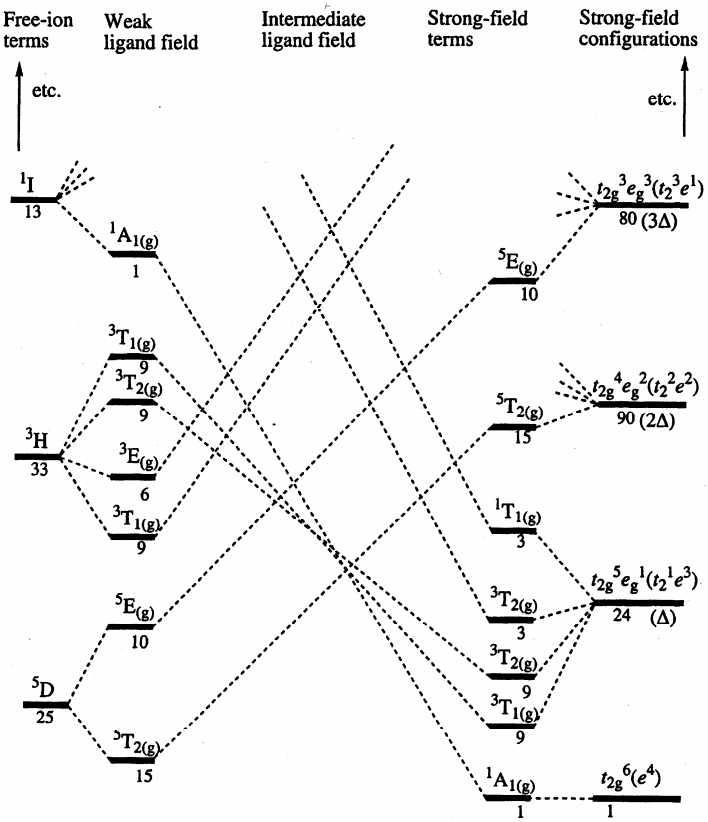

Fig. 8. The correlation diagram for the ion terms for $3d^4$ in T_d and $3d^6$ in O_h (after [39]).

The correlation diagram is a rather good qualitative illustration of the transition from weak to the strong ligand fields, but its disadvantage is the fact, it cannot be used for the interpretation of the real spectra. For this purpose the energy levels of a d^n system should be calculated, taking into account both ligand field influence and interelectronic repulsion, which is characterized by so-called Racah parameters [40,41]. They are determined experimentally and for Cr^{2+} ion, for instance, have the following values: B=810 cm^{-1} and C=3565 cm^{-1}, therefore $\gamma=C/B$=4.40 [42]. The latter ratio makes it possible to use only two (instead of three) parameters – Δ and B, which characterize the relative position of the energy levels. Thus, while choosing the abscissa axis in the units of B, one can plot the dependence of energy levels as a function of Δ. Such diagrams were proposed by Tanabe and Sugano [42,43] for all configurations d^n $(n = 2 \div 8)$.

The lowest energy term is always taken as the zero level in these diagrams and if the change of the ground state occurs at some value of Δ, all the terms undergo a break, which corresponds to the transition from the weak to the strong ligand field. Fig.9 represents the Tanabe-Sugano diagram for the d^6 configuration in O_h symmetry, which is also valid for the d^4 case in T_d symmetry, according to the above mentioned reasons.

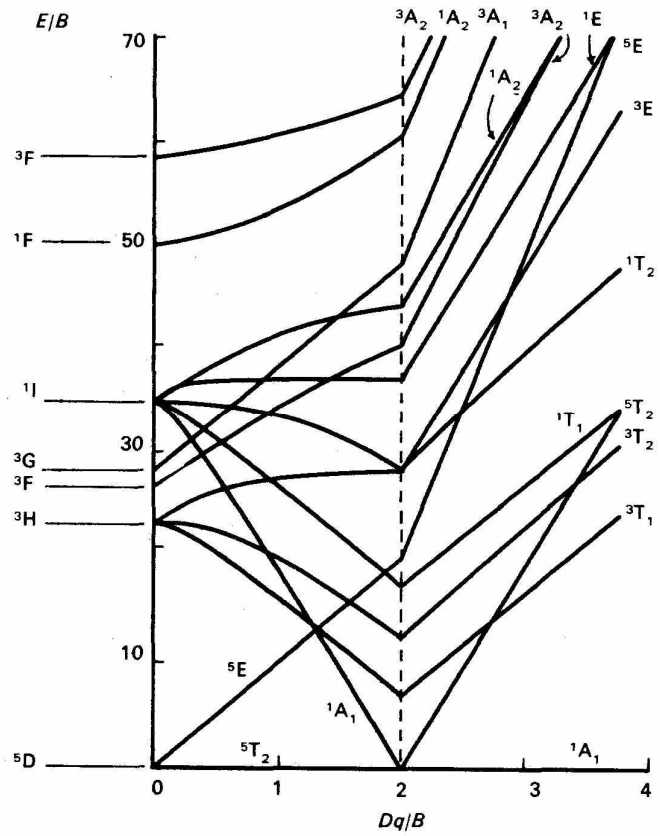

Fig. 9. Energy levels of the $3d^6$ system for the octahedral ligand field. The energy values are calculated for γ=4.81 (following [12,42,43]).

Thus, this diagram was used to analyze the high-pressure photoluminescence spectra, obtained from the Cr^{2+} ion, embedded into ZnX (X=S, Se, Te) lattices (what will be discussed in the Chapter 6 of the Thesis). Nevertheless, one should also notice that Tanabe-Sugano diagrams are of approximate nature. They do not take into consideration the overlapping of the wave function, which can take place in the crystal lattice and be responsible, e.g., for the covalence effects.

2.2.2. The energy structure of Cr^{2+} ion

An isolated chromium atom has 24 electrons, which arranged in the following configuration: $1s^2\,2s^2\,2p^6\,3s^2\,3p^6\,3d^5\,4s^1$. Having been inserted into the cation position in the II-VI crystal structure, the *Cr* atom loses two electrons and remains a Cr^{2+} cation with $3d^4$ configuration. In 1970 J.T.Vallin et al for the first time applied the basis of above discussed ligand field theory in order to describe the energy levels of Cr^{2+} ion embedded in the ZnS, ZnSe and ZnTe crystals lattices [5]. This model was found to be effective for the interpretation of magnetic [5,44-48] and optical properties [49-51] of the ZnX:Cr^{2+} (X=S, Se, Te) crystals. The main points of this model can be represented as follows.

The energy structure of the Cr^{2+} ion can be described by the following Hamiltonian:

$$H = H_{CF} + H_{J.-T.} + H_{so} + H_B \ , \tag{2.22}$$

where:

– H_{CF} is the cubic ligand field of tetrahedral symmetry T_d;

– $H_{J.-T.}$ stands for the static Jahn-Teller distortion of tetragonal symmetry;

– H_{so} describes the spin-orbit interaction;

– H_B is responsible for the interaction with the external magnetic field (if it is present).

The term, responsible for the crystal field, can be expressed by the equation [52]:

$$H_{CF} = B_4(O_4^0 + 5O_4^4)\,, \tag{2.23}$$

where the equivalent operators O_4^0 and O_4^4 are defined as follows:

$$O_4^0 = 35L_z^4 - 30L(L+1)L_z^2 + 25L_z^2 - 6L(L+1) + 3L^2(L+1)^2\,, \tag{2.24}$$

$$O_4^4 = \frac{1}{2}(L_+^4 + L_-^4)\,. \tag{2.25}$$

Here $L = (L_x,\ L_y,\ L_z)$ is the orbital momentum operator, and $L_\pm = L_x \pm iL_y$. The B_4 crystal field parameter is related to the commonly used parameter *Dq* by the equation:

$$12B_4 = Dq \tag{2.26}$$

The strong static Jahn-Teller effect of Cr^{2+} ion takes place along one of three directions: A (<100>), B (<010>) or C (<001>), as it is presented in Fig. 10 [3,5,53,54].

The Jahn-Teller distortion is described by the second term of the Hamiltonian (2.22) [52]:

$$H_{J.-T.} = B_2^0 O_2^0 + B_4^0 O_4^0\,, \tag{2.27}$$

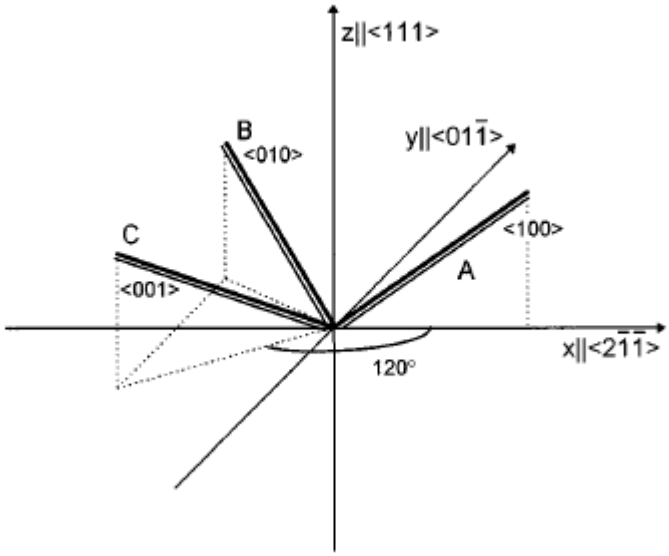

Fig. 10. The typical crystallographic directions in the Cr^{2+} ion surrounding [53]. The bold lines (labeled as A, B and C) represent the axes of Jahn-Teller distortion.

where O_4^0 is the operator determined in (2.24), and

$$O_2^0 = 3L_z^2 - L(L+1)\,. \tag{2.28}$$

On the other side, in the F.S.Ham's notation [55,56], the most general Hamiltonian for a linear Jahn-Teller coupling, concordant with the symmetry requirements, can be written as follows:

$$H_{J.-T.} = V_1(q_\theta \varepsilon_\theta + q_\varepsilon \varepsilon_\varepsilon) + V_2(q_\theta U_\theta + q_\varepsilon U_\varepsilon) + \frac{1}{2}k(q_\theta^2 + q_\varepsilon^2)I\,, \tag{2.29}$$

where:

– V_1 and V_2 are the coupling coefficients of the lattice to the orbital $^5T_2$ and ^5E states, respectively;

– q_θ and q_ε are the dimensionless parameters, which measure the magnitudes of the two E distortrions Q_θ and Q_ε in the F.S.Ham's notations (i. e. Q_3 and Q_2 distortions in the notations, used in the 2.1.2 section of this Thesis);

– ε_θ and ε_ε are the electronic operators, which only have matrix elements within the orbital T_2 wave functions;

– U_θ and U_ε are the electronic operators, which operate within the orbital E wave functions;

– $-\frac{1}{2}(q_\theta^2 + q_\varepsilon^2)$ term is the elastic energy, associated with the distortion;

– I is the unit matrix.

A schematic illustration of the energy levels of a Cr^{2+} ion, located in the field of ligands with D_{2d} symmetry and tetragonal distortion is presented in Fig. 11. The ground term of the isolated Cr^{2+} ion is ^5D, with a total orbital momentum L=2 and a total spin S=2, thus, it is 25-fold degenerate. The first item H_{CF} of the equation (2.22) splits the ^5D ground term of the isolated ion Cr^{2+} into 15-fold degenerate $^5T_2$ orbital triplet and 10-fold degenerate ^5E orbital doublet, separated by ~5000 cm^{-1} (~619 meV). The ground term $^5T_2$ undergoes a static tetragonal Jahn-Teller distortion, equivalent to the stress along the A (<100>) crystal axis (which is considered by J.T.Vallin et al. to be the most probable one for the tetragonal compression). This distortion reduces the local symmetry to D_{2d} and leads to $^5T_2$ splitting into $^5\hat{B}_2$ ground singlet and $^5\hat{E}$ elevated doublet. In Fig. 11 this splitting is labeled as $1.5V_1q_\theta$, according to the mentioned above notes. The coupling of the ^5E doublet, in turn, equals $2V_2q_\theta$.

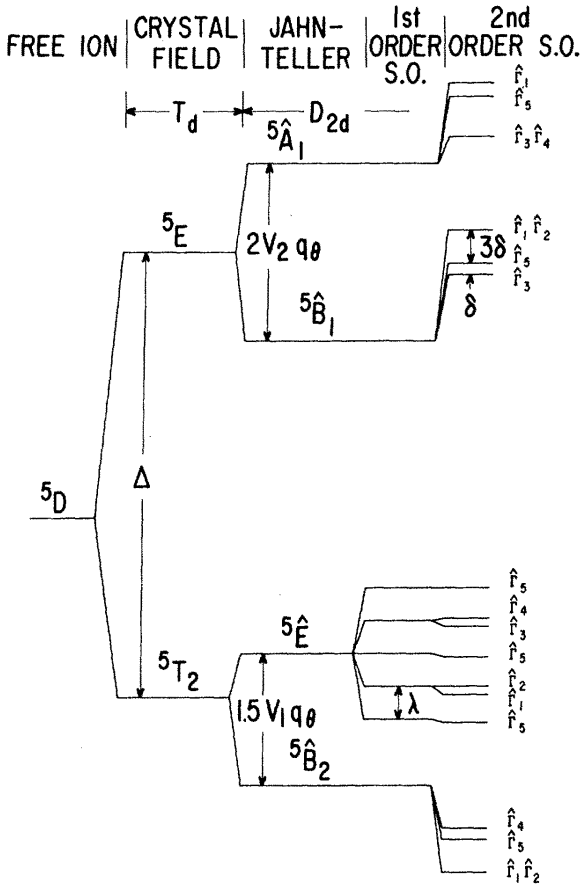

Fig. 11. Energy level of Cr^{2+} ion, predicted by crystal-field theory for the substitutional cation site of D_{2d} symmetry (after [5]).

While comparing the calculating results with the real absorption spectra, the authors come to the conclusion, that the best fit is achieved, when $V_1 >> V_2 \neq 0$ and $E_{J.-T.} \approx 0$. In this case the wave functions of the ${}^5E$ excited state are inseparably mixed and represented by five equally located levels.

G. Grebe et al. [57,58] studied the low-temperature ${}^5E \rightarrow {}^5T_2$ photoluminescence of ZnSe and ZnS crystals, doped with Cr^{2+} ions. The observed no-phonon lines were assigned to the to the transitions, terminating on the $\hat{\Gamma}_1$, $\hat{\Gamma}_2$ and $\hat{\Gamma}_5$ levels of the split ${}^5\hat{B}_2$ term.

M. Kamińska et al. investigated the absorption and emission spectra of ZnX (X=S, Se, Te), taken at liquid-helium temperature [4]. The experimental results were interpreted in the framework of the crystal field theory with spin-orbit coupling and Jahn-Teller distortion of both ${}^5T_2$ and ${}^5E$ terms. Using the Franck-Condon principle, the absorption and emission spectra were calculated with the semiclassical approximation. In the regions, where transitions occur, the surfaces of the potential energies were approximated by harmonic potentials. This approach is rather successful for the absorption case, since the Jahn-Teller stabilization of the ground state is large enough for the region near the energy minimum, approximated by parabola.

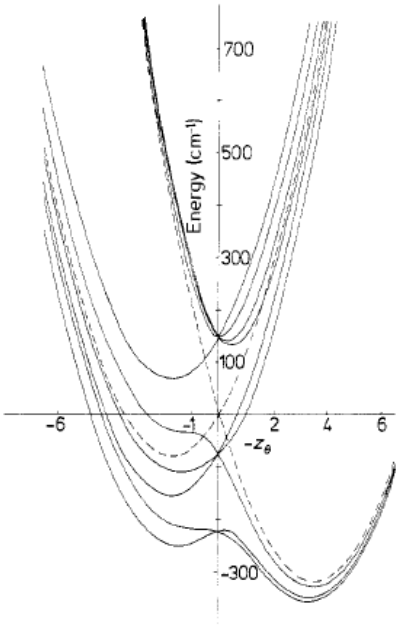

Fig. 12. The schematic illustration of the cross section along the z_θ axis for the ${}^5T_2$ state with coupling to E mode (after [4]). The units of the abscissa is $(\hbar/m\omega)^{1/2}$.

The schematic illustration of the calculation results is presented in Fig. 12. The solid curve is simulated for the presence of spin-orbit coupling, characterizining by a spin-orbit parameter λ=–74 cm^{-1}. The dashed curve corresponds to the case without spin-orbit splitting,

but with the same values of Jahn-Teller energy $E_{J.-T.} \approx 320\ \mathrm{cm}^{-1}$ and mode frequency $\hbar\omega = 50\mathrm{cm}^{-1}$. In the latter case ($\lambda \approx 0$) the double peak shape of the emission spectra is interpreted by the authors as the Jahn-Teller interaction in the excited ^5E state. The Jahn-Teller energy of this term $E_{J.-T.}(^5E) \approx 50\ \mathrm{cm}^{-1}$ was estimated to be smaller, than in the case of $^5T_2$ term.

Natadze and Ryskin [59] reported about the larger Jahn-Teller energy value for the excited ^5E state in the case of ZnS:Cr^{2+} crystals: $E_{J.-T.}(^5E) = 94\mathrm{cm}^{-1}$. They calculated an equally strong coupling to *e*- and t_2-modes for the ground state, while assuming "nearly dynamic" Jahn-Teller effect. Several authors [60,61] also discussed that the coupling with t_2-modes is comparatively insignificant.

2.2.3. The spin-orbit interaction of Cr^{2+} ion

The energy levels of the atomic electrons are affected by the interaction between the electron spin magnetic moment $\vec{s}$ and the orbital angular momentum $\vec{l}$. In the relativistic approximation the operator of the interaction energy between $\vec{s}$ and $\vec{l}$, being obtained from the Dirac equation, can be expressed by the following formula [41]:

$$H_{so} = \xi(r)(\vec{l},\vec{s}), \tag{2.30}$$

where

$$\xi(r) = -\frac{e}{2m^2c^2}\frac{1}{r}\frac{\partial V(r)}{\partial r} \tag{2.31}$$

and $V(r)$ is the potential of the nuclei field.

While taking into account the spin-orbit operator as a perturbation, one can calculate the proper corrections for the atomic energy levels. Usually they are defined by the matrix elements of the perturbation, in which the main part is the following value:

$$\zeta_{n,l} = \hbar^2 \int \xi(r) R_{n,l}^2(r) dr, \tag{2.32}$$

where $R_{n,l}(r)$ is a radial part of the wave function of the perturbated electron state, *n* and *l* are principal and orbital quantum numbers respectively. The term $\zeta_{n,l}$ is a so-called *spin-orbit interaction constant*. While substituting (2.31) into (2.32), one can also take into consideration that the Coulomb electrostatic field of the nucleus can be written as:

$$V = \frac{Ze}{r}, \tag{2.33}$$

where *Z* is the atomic number, and that average value of the r^{-3} for the so-called hydrogenic wave function can be expressed as [62]:

$$\int r^{-3} R_{n,l}^2 dr = \frac{Z^3}{a^3 n^3 l(l+1)\left(l+\frac{1}{2}\right)}, \tag{2.34}$$

where $a = \frac{\hbar^2}{me^2}$. Then, the equation (2.32) can be re-written in the following way:

$$\zeta_{n,l} = \frac{Ze^2\hbar^2}{2m^2c^2a^3}\int r^{-3} R_{n,l}^2(r) dr = \frac{e^2\hbar^2}{2m^2c^2a^3}\frac{Z^4}{n^3 l(l+1)\left(l+\frac{1}{2}\right)} \tag{2.35}$$

When a system has more, than one electron, the total perturbation of the spin-orbit interaction can be expressed by the equation:

$$H_{so} = \sum_i \xi(r_i)(\vec{l}_i, \vec{s}_i) \tag{2.36}$$

In case of LS-bound spin-orbital interaction is assumed to be weak, thus, it can be counted as a perturbation of the states with perfect L and S. It was also shown [41], that in this case the spin-orbit operator can be represented by the formula:

$$H_{so} = \lambda(LS), \tag{2.37}$$

where λ is a *constant of a spin-orbit interaction, being called spin orbit-parameter* and $S = (S_x, S_y, S_z)$ is the spin operator. The expression (2.37) also represents the H_{so} term of the (2.22) equation. The spin–orbit parameter λ can be expressed as a sum of radial integrals of (2.35) type, thus:

$$\lambda \propto Z^4 \tag{2.38}$$

Meanwhile, the EPR studies have shown [3,63,64], that the spin-orbit parameter value for Cr^{2+} ion, embedded into the II-VI compound lattice differs from that value for free ions. This fact was explained by the hybridization of the central ion *d* wave functions and the ligand wave functions. As the ligand spin-orbit parameter is often significantly larger, than that one of the central Cr^{2+} ion, even small admixtures of ligand wave functions may change the value of the spin-orbit parameter of Cr^{2+} ion. As it follows from the previous publications [3,4,63,64], this change, can be approximated by the following expression:

$$\lambda = \lambda_0(1-a), \tag{2.39}$$

where λ_0=57 cm^{-1} is the spin-orbit parameter of the Cr^{2+} free ion, and a=0.2, 1 and 2.3 for ZnS, ZnSe and ZnTe respectively. The negative sign of the λ for ZnTe is explained by the large spin-orbit parameter of *Te*. In ZnSe case the spin-orbit parameter is assumed to be 0, i.e. spin-orbit splitting in ZnSe:Cr^{2+} case is supposed to be very weak.

On the other hand, taking into account the dependence (2.37) and comparing the atomic numbers for *S*, *Se* and *Te* atoms, one can conclude, that:

$$\lambda_S < \lambda_{Se} < \lambda_{Te}. \tag{2.40}$$

Therefore, it is possible to assume, that *S*, *Se* and *Te* ligand atoms will provoke the spin-orbit splitting of Cr^{2+} central ion to the extent, being defined by (2.39) inequality. This assumption

is of contradiction with the λ values, having been obtained from (2.38) formula, which are equal to 46 cm^{-1}, 0 and –74 cm^{-1} for ZnS, ZnSe and ZnTe respectively.

The mentioned above contradiction was to be checked experimentally, and this is one of the goals of the present Thesis.

2.2.4. Optical properties of ZnX:Cr (X=S, Se, Te) crystals

During the last 40 years there were published numerous reports about the experimental studies of the optical transitions, originating from the split energy levels of Cr^{2+} ion, embedded in the tetrahedral ligand field of II-VI semiconductor lattices. First, the researchers' attention was attracted by the midinfrared (between 2 and 4 μm) emission of Cr-doped II-VI compounds [57,58] as they could be effectively applied for the new laser systems, operable in this spectral range. Later on these semiconductor structures awoke a vivid interest as new materials for the construction of blue-green laser diodes, continuous-wave lasers with life-times exceeding 100h and also fluorescent displays [65-67].

Absorption. The first intensive investigations of ZnX:Cr (X=S, Se, Te) started just in the early seventies of the last century and these experimental works were devoted to the study of the optical absorption spectra, taken at room and liquid helium temperature [5,68,69]. It was found out, that the room-temperature spectrum revealed a broad absorption band at about 5500 cm^{-1}, which originated from $^5T_2 \rightarrow {}^5E$ transition. At liquid-helium temperatures a single [5] or double [70] so-called *zero-phonon line* (ZPL) appeared on the low-energy side of the absorption band and its intensity decreased with the temperature increase. These lines are associated with the optical transitions between the ground state ($\hat{\Gamma}_1$, $\hat{\Gamma}_2$ or $\hat{\Gamma}_4$ level of the $^5B_2$ term, originating from the split $^5T_2$ term and the lowest excited state ($\hat{\Gamma}_3$ level of the $^5B_1$ term, originating from the split ^5E term). The main absorption band parameters, obtained in these investigations, are presented in the Table 2. Further experimental studies of these materials, made it possible to characterize the other energy transitions, listed in the Table 3:

1. Between the levels, arisen due to spin-orbit splitting of the $^5B_2$ term: ($\hat{\Gamma}_1$,$\hat{\Gamma}_2$) semidoublet and $\hat{\Gamma}_5$ doublet.

2. Between $^5B_2$ and ^5E level of the $^5T_2$ term, split due to the Jahn-Teller distortion. (This splitting is equal to $3E_{J.-T.}$).

The energy of $(\hat{\Gamma}_1, \hat{\Gamma}_2) \rightarrow \hat{\Gamma}_5$ transition was determined by means of far infrared (FIR) absorption measurements and via low-field EPR study. One should mention, that the sequence of the spin-orbitally split states within the $^5B_2$ term in ZnX:Cr (X=S, Se, Te) crystals turned out to be dependent on the anion type (X). These sequences were determined on the basis of temperature-dependence studies of EPR line intensities [3] and are also presented in the Table 3.

Table 2. The characteristics of the near-infrared absorption band of ZnX:Cr (X=S, Se, Te) crystals (after [5,70]).

Crystal type	Absorption band peak, cm^{-1}		FWHM of AB, cm^{-1}	ZPL peak position, cm^{-1}	
	T=2 K	T=300 K		After J.T. Vallin et al. [5]	Following G. Goetz et al. [70]
ZnS:Cr	5800	6000	1035	5224±2	5212; 5218
ZnSe:Cr	5525	5650	675	4975±3	4971
ZnTe:Cr	5530	5620	570	4994±2	---

Table 3. Experimental spectroscopic parameters of Cr^{2+} ion, embedded into the different ZnX:Cr (X=S, Se, Te) crystal lattices. (All energy values are in cm^{-1}).

Crystal type	Ground state	$(\hat{\Gamma}_1, \hat{\Gamma}_2) \rightarrow \hat{\Gamma}_5$ transition		The Jahn-Teller splitting of the $^5T_2$ term		
		FIR absorption measurements	Low field EPR srudies [3]	Following J.T.Vallin et al. [5]	After M.Kamińska et al. [4]	Following J.T.Vallin and G.D.Watkins [3]
ZnS:Cr	(Γ_1, Γ_2)	5.53±0.10 [a)]	5.58±0.09	575	300	---
ZnSe:Cr	(Γ_1, Γ_2)	7.43±0.02 [b)]	7.44±0.03	550	340	> 470
ZnTe:Cr	Γ_4	---	6.60±0.06	535	320	> 200

[a)] After A.E.Hughes and J.T.Vallin [71];

[b)] According to J.T.Vallin et al. [5].

As it follows from the Table 3, there is a large discrepancy between the Jahn-Teller energy values of the $^5T_2$ term, reported by different authors.The Jahn-Teller energy of the ^5E term is reported to be rather small: about (40…60) cm^{-1} [4] or even close to zero [5].

High-pressure dependence of the ZnS:Cr near-infrared absorption, centered at about 0.72 eV was investigated by C. Stuart Kelley in 1973 [72]. The measurements were performed at 0, 5, 10 and 15 kbar at T=300 K in order to determine the dependence of the absorption coefficient α on the full-width at half-maximum (FWHM) E. Then, on the basis of T.Keil's semiclassical treatment of the band shape [73], using the dependence

$$\alpha = \alpha_0 + \alpha_m \exp\left[-4\ln 2(E - E_0)^2 / \gamma^2\right], \tag{2.35}$$

the author determined three parameters of the absorption band: a full-width at half-minimum (FWHM) γ, a maximum of absorption intensity α_m and a position of the absorption peak E_0 for each pressure value. Thus, pressure dependences of these parameters were also estimated and found to be equal to: $-8.6\cdot10^{-4}$ eV/kbar (-6.94 cm^{-1}/kbar), $9\cdot10^{-3}$ cm/kbar and $4.1\cdot10^{-5}$ eV/kbar (0.33 cm^{-1}/kbar) for γ, α_m and E_0 respectively. The cited paper is only one known to the author of the Thesis publication, devoted to the high-pressure optical studies of Cr-doped ZnX (X=S, Se, Te) semiconductors.

Photoluminescence. The experimental optical studies of II-VI Cr^{2+}-doped semiconductors [45,46] in both room and liquid-helium temperature have revealed, that the photoluminescence (PL) of Cr^{2+} impurity behaves similarly for all ZnX (X=S, Se, Te) host lattices. Thus, the emission bands have the analogous shape, and in the case of ZnX:Cr (X=S, Se) the spectral position of the $^5E \rightarrow {}^5T_2$ transition was found to be dependent on the energy gap [70]. This tendency is also observed in the case of other Cr-doped II-VI semiconductors (e.g. CdS:Cr and CdSe:Cr samples), but ZnTe:Cr emission band is not kept within mentioned regularity (Table 4.).

Liquid-helium PL of ZnX:Cr (X=S, Se) samples reveal a characteristic double-peak form [4,57,58], which is a consequence of $^5A_1(E) \rightarrow {}^5B_2(T_2)$ and $^5A_1(E) \rightarrow {}^5B_2(T_2)$ transitions [74]. The distance between the peaks is about 420 cm^{-1} and 340 cm^{-1} in the case of Cr-doped ZnS and ZnSe samples respectively. The low-temperature PL of the ZnTe:Cr samples reveals a pronounced 3-peak band, observed in the case of both bulk samples [4] and epilayers [75]. As far as PL process has been reported to depend strongly on the anions which surround the Cr^{2+} ions [70], the presence of the third peak has been explained by the significant splitting of the ground $^5T_2$ state, being a consequence of the Te admixture into

the *Cr* ion wave function [4]. It was found to be in a good agreement with the theoretical investigations [11,76,77], which emphasized the hybridization of the wave functions of the central ion with those of the neighboring anions.

ZnS:Cr samples have revealed a pronounced phonon structure compared to the Cr-doped ZnSe and ZnTe samples. The ZPL doublet observed at Cr-doped zinc sulfide and selenide emission bands was interpreted as the transition from the excited ^5E state into the spin-orbit components of the $^5T_2$ state. But the position of the ZPL doublet was not identical in the reports of the different authors. Thus, G. Grebe and H.-J. Schulz have revealed the ZPLs at 5211 and 5216 cm^{-1}, what corresponded to the 3 cm^{-1} shift towards the lower energy versus the position of these lines in the absorption spectra [57]. Later G. Goetz with co-authors asserted, that the ZPL doublet was observed at 5212 and 5218 cm^{-1} [70], both in the emission and in the absorption spectra (see Tables 2 and 4) and these values were declared by authors as authentic ones. The strength of the ZPLs were found to be strongly dependent on the *Cr* concentration in the case of ZnS:Cr samples.

Meanwhile, the authors of [70] claim, that a low-temperature ZnSe:Cr photoluminescence does not reveal a significant dependence on the *Cr* concentration in comparison with ZnS:Cr case. PL band is also characterized with the ZPL doublet at 4964 and 4971 cm^{-1} [58,70], which are not observed at coinciding energy values in the absorption band (contrary to ZnS:Cr case) – only a faint structure at 4964 cm^{-1} becomes noticeable at about 15 K. With the *Cr* concentration increase the ZPLs were found to be less distinct [70].

Table 4. The characteristics of the near-infrared PL band of ZnX:Cr (X=S, Se, Te) crystals (after [4,70,78]).

Crystal type	Band-gap energy of the host crystal, after D.Long [79]	Approximate PL peak position of $^5A_1(E)\rightarrow{}^5B_2(T_2)$ transition (following M.Kamińska et al. [4]), cm^{-1} (eV)	ZPL peak position (following G.Goetz et al. [70]), cm^{-1}
ZnS:Cr	3.68	5008 (0.621)	5212; 5218
ZnSe:Cr	2.8215	4754 (0.589)	4964; 4971
ZnTe:Cr	2.394	4784 (0.593)	---

Besides of the wide ZnSe:Cr PL band, associated with the $^5E \rightarrow {}^5T_2$ transition, several authors reported about another PL peak, centered at about 10485 cm^{-1} (1.3 eV) [80] or 11290 cm^{-1} (1.4 eV) [81]. Meanwhile, the nature of this band was explained in the contradictory way.

First of all, H.Pradella and U.W. Pohl associated this PL band with $^4T_1 \rightarrow {}^6A_1$ transition of Cr^{1+} [82]. In turn, M.U.Lehr and coauthors interpreted this emission peak as $^3T_1 \rightarrow {}^5T_2$ transition of the Cr^{2+} ion [83].

The other authors, who tried interpret the origin of this band took into account the localization of *Cr* deep impurity levels in ZnSe:Cr band gap, determined on the basis of photo-ESP measurements by M. Godlewski and M. Kamińska. These levels were found to be localized at 1.24 and 2.26 eV beneath the conduction band edge for Cr^{1+} and Cr^{2+} states respectively [84].

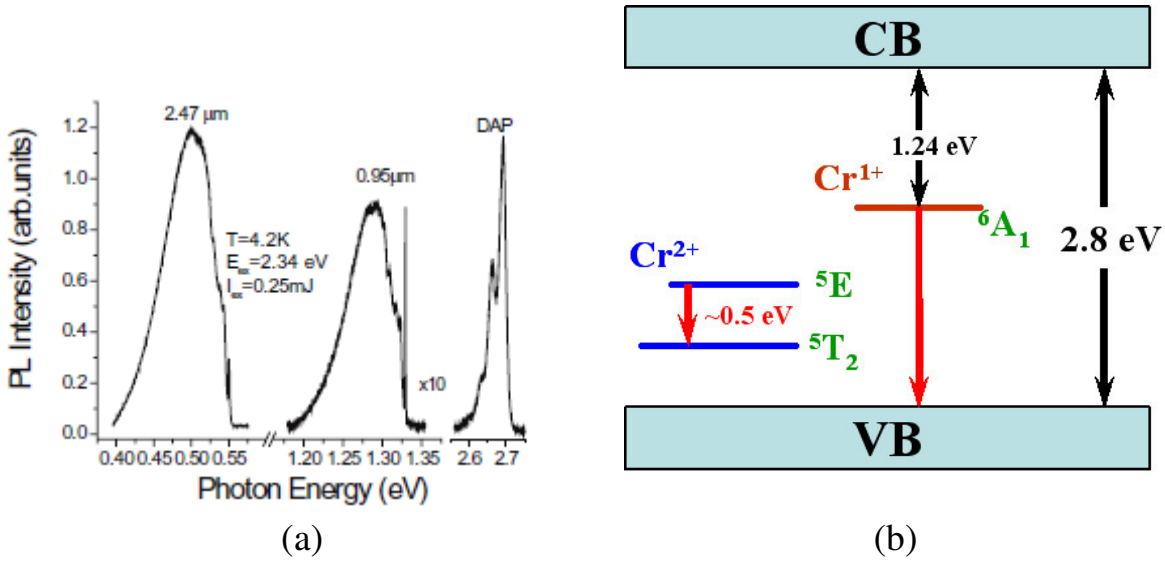

(a) (b)

Fig. 13. The emission spectra of ZnSe:Cr crystal (after [80]) reveals Cr-related PL bands centered at ~0.5 and ~1.3 eV, which have $^5E \rightarrow {}^5T_2$ (Cr^{2+}) transition nature and an unidentified origin respectively (a); the schematic illustration of Cr^{2+} and Cr^{1+} levels in the ZnSe:Cr band gap following [2,84] (b).

Taking into consideration these values, one can conclude, that the PL band centered at about 1.3 (1.4) eV may originate from the transition from $^6A_1$ level of Cr^{1+} state to the valence band [81] (Fig.13).

Consequently, the origin of this peak was not explained unambiguously and therefore the interpretation of this PL peak was one of the goals of the present Thesis.

3. HIGH-PRESSURE INVESTIGATIONS

3.1 The effect of high pressure on semiconductors

The effect of the high hydrostatic pressures on the band gap of a typical A^NB^{8-N} semiconductor compound can be described in the terms of the interactions of the nearest neighbours. It is known, that the symmetric (antisymmetric) combinations of the adjacent atoms lead to bonding (antibonding) molecular orbitals. The schematic illustration of the dependence of atomic energy levels on the interatomic distances is shown in Fig. 14. The interatomic distance d_0, which minimizes the total energy of the crystal corresponds to the equilibrium lattice constant.

As it follows from the picture, the decrease of d with respect to d_0 leads to relatively little change of the bonding states, whereas the antibonding states increases significantly. Therefore the bonding-antibonding splitting is also expected to increase with pressure, as well as the lowest direct semiconductor bandgap at the Brillouin-zone center.

Both experimental and theoretical studies of semiconductors show, that the application of hydrostatic pressures allows to achieve a controlled tuning of the bandgap towards a crossover of zone center (Γ) and zone boundary (X) of conduction-band states.

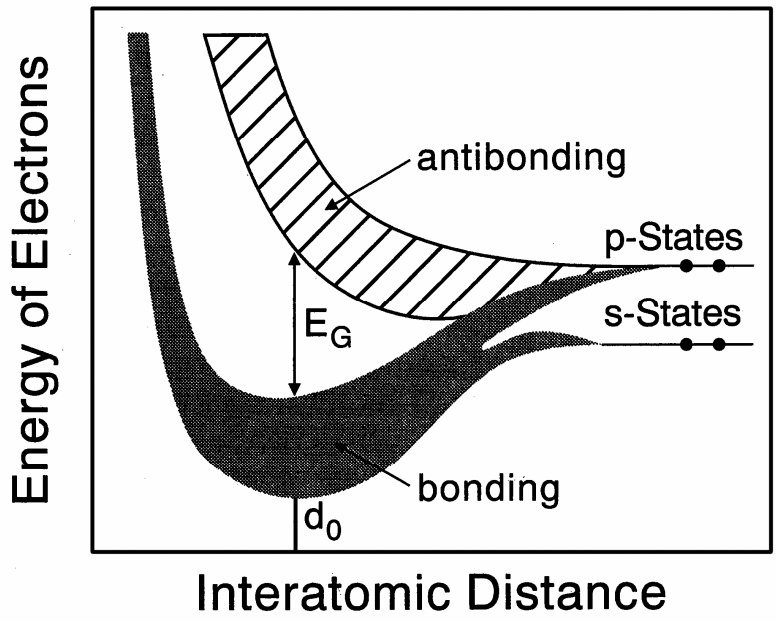

Fig. 14. The schematic illustration of the atomic energy levels versus interatomic distances in a typical A^NB^{8-N} semiconductor. The d_0 distance corresponds to the equilibrium state of atoms in the solid (following [85]).

The effect of the high pressure on the quantum well can be analyzed with the use of $\vec{k}\cdot\vec{p}$ calculations within the so-called envelope function approximation [86,87]. Thus, quantum well states can be described as a superposition of Bloch wavefunctions. And the Fourier transform of each expansion coefficient of Bloch function is just an envelope function $F(z)$, which can be obtained as a solution of a Schrödinger equation:

$$\left[-\frac{\hbar^2}{2\tilde{m}^*}\frac{\partial^2}{\partial z^2}+U_{SL}(z)\right]\cdot F_n(z)=\varepsilon_n\cdot F_n(z), \tag{3.1}$$

where $\tilde{m}^*$ is the effective mass tensor and U_{SL} is a superlattice potential.

For the infinitely deep and L_z wide quantum well the energy eigenvalues ε_n and wave functions F_n of Eq. (3.1) can be obtained as:

$$\varepsilon_n=\frac{\hbar^2}{2m^*}\cdot\left(\frac{n\pi}{L_z}\right)^2=\frac{\hbar^2}{2m^*}\cdot(k_n)^2,\ \text{n = 1, 2, 3, …} \tag{3.2}$$

$$F_n(z)=A\cdot\sin\left(\frac{n\pi z}{L_z}\right), \tag{3.3}$$

where $k_n=\frac{n\pi}{L_z}$ is a magnitude of the effective confinement wave vector (n is a subband quantum number). As it follows from (3.2) equation, the confinement energy ε_n grows quadratically with k_n value and decreases inversely to the effective mass of the confined particle.

One should take into account, that the bandgap E_0 icreases due to confinement, what results in its additional nonparabolicity. Thus, the effective masses of the light particles in the wells are assumed to be not constants, but dependent on energy. The $\vec{k}\cdot\vec{p}$ calculations of the effective masses of electrons and light holes lead to the following expressions [88]:

$$\frac{m_0}{m_e^*(\varepsilon_n)}=1+\frac{2p^2}{3m_0}\left(\frac{2}{E_0+\varepsilon_n}+\frac{1}{E_0+\varepsilon_{SO}+\varepsilon_n}\right), \tag{3.4}$$

$$\frac{m_0}{m_{lh}^*(\varepsilon_n)}=1-\frac{4p^2}{3m_0}\frac{1}{E_0+\varepsilon_n}\cdot\left(1-\frac{\varepsilon_n}{2(\varepsilon_{SO}-\varepsilon_n)}\right), \tag{3.5}$$

where p is the matrix element of the momentum operator, defined as

$$p=p_x=p_y=p_z=-i\langle s|p_x|x\rangle \tag{3.6}$$

and ε_{SO} is the spin-orbit coupling energy.

The latter dependences can be used to analyze the effect of pressure on the quantum well. If the pressure is applied, the light particles become heavier, as the bandgap increases. According to (3.2) this, in turn, reduces the confinement energy of electrons and light holes. On the other hand, the height of the potential barriers for confinement also varys with pressure, if the band offsets are dependent on it. In the first approximation it can be assumed, that the band offsets change with pressure proportionally to the difference of the pressure coefficient of the energy gaps of the quantum well and barrier materials:

$$\frac{\partial \Delta U_{C,V}}{\partial P} \approx Q_{C,V} \cdot \left(\frac{\partial E_0^{QW}}{\partial P} - \frac{\partial E_0^{B}}{\partial P} \right), \tag{3.7}$$

where $Q_{C,V}$ is a pressure-independent coefficient.

As a an example, it was reported, that for GaAs/AlGaAs the offsets varied negligibly with pressure [89,90], whereas for GaSb/InAs QWs the offset changes reached ~6 meV/kbar [90-92].

3.2. The principles of DAC operation

The era of high-pressure measurements began since 1910, when the first devices for this purpose were invented by Percy Williams Bridgman, who afterwards won the Noble Prize in Physics in 1946, *"for the invention of an apparatus to produce extremely high pressures and for the discoveries he made therewith in the field of high pressure physics"*. His first mechanisms were able to achieve the pressures up to 100 kbar[1] [93]. In the post-Bridgman times ultra-high-pressure supported anvil devices were constructed for the electric and x-ray measurements and reached several hundred kbar [94,95]. But the crucial invention, which was the turning point in the high-pressure generation technique was a so-called *diamond anvil cell* (DAC), which conceived independently in 1959 in the University of Chicago [96] and in the National Bureau of Standards (NBS) [97]. During the last 50 years numerous developments and innovation designs made it possible to operate DAC very easily, achieving the pressures up to 550 GPa [98-100]. Thus, nowadays DAC became an extremely important tool for the up-to-date physical research.

[1] 1 bar = 10^5 Pa ≈ 1 atm (= 0.9869 atm); 1 kbar = 0.1 GPa ≈ 1000 atm.

The experiments, described in the present Thesis, were performed with a so-called gasketed DAC. It consists of two diamonds, which bear with their tips (culets) on a metal gasket (Fig. 15). The culets are flat dioctahedron surfaces, with about 750 μm distance between the opposite sides of the dioctahedron. The gasket is a metal sheet, made of Inconel or tempered stainless steel, usually (0.25÷0.45) mm thick, which has a proper elasticity according to the maximum pressure, applied during the measurements.

A very small sample (dozens of micrometers in length, width and thickness), together with the pressure sensor is loaded into the DAC. Then the sell is filled up with a pressure-transmitting medium and hermetically closed with diamonds. While exerting pressure on the diamonds, one can hydrostatically stress the sample and the ruby, which plays a role of the pressure gauge.

The basic principle, which makes it possible to achieve extremely high pressures, using DACs is very simple. While applying relatively weak force to the diamond culet with a very small area (about 0.45 mm^2) one can obtain utterly high pressures. Diamond is considered to be the most proper and convenient material for the construction of such pressure cells because of two reasons. First, it is the firmest natural material, known by the present day.

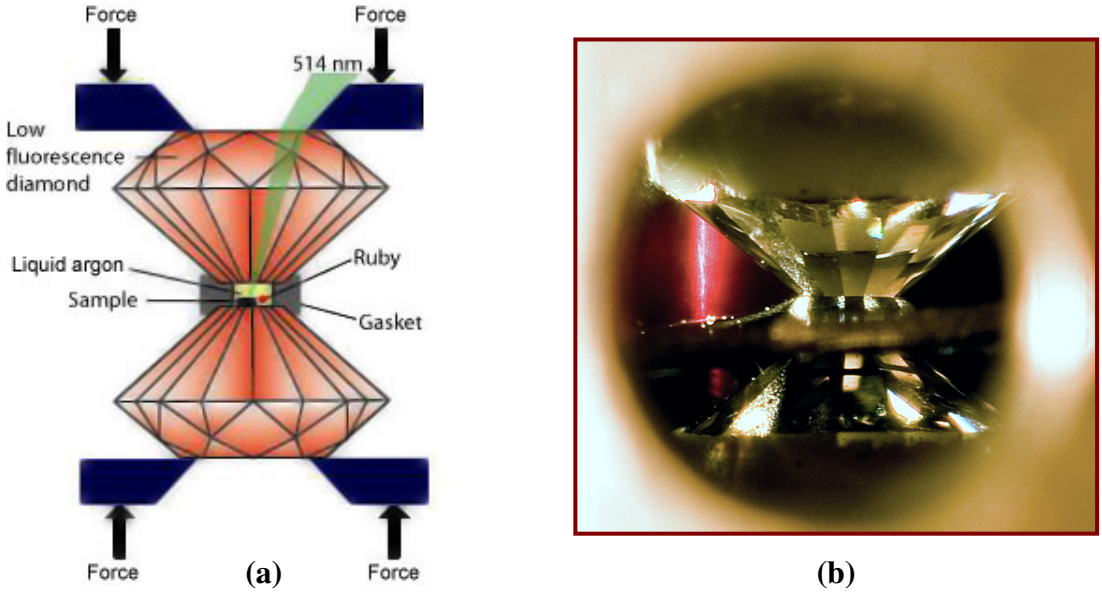

Fig. 15. A schematic view of the DAC, following [101] (a); and a picture of diamonds with a gasket, which are seen throw the hole in the DAC[1)], mounted into the holder before high-pressure measurements (b).

[1] The picture was taken by mgr Jacek Błoniarz in the optical laboratory of the scientific Division ON 4.1 in the Institute of Physics PAS. This photo has won an annual competition of the pictures, chosen to be printed in 2009 wall calendar of the IF PAS. (In the Thesis the picture was reproduced with the author's permission).

Second, due to its transparency, one can perform high-pressure experiments, while observing the sample. The excitation illumination, which can reach the sample in the DAC, belongs to the rather wide optical spectral range – from infrared up to ultraviolet (5.3 eV). Furthermore, X-rays can also penetrate the sample [102]. But on the other hand, diamonds demand an exclusive accuracy during the DAC loading and measurement preparation, what protracts this process significantly.

While performing high-pressure measurements, one has take into account that the diamonds have to be placed in the DAC in strict parallel with each other; otherwise they can crack during the measurements. Besides, the maximum pressure, which can be applied to the DAC is limited by the diamond culet diameter. D.J. Dunstan and I.L. Spain proposed the empirical relationship between the maximum pressure, which can be achieved in the DAC and diamond diameter [102]:

$$p_{\max}[GPa] = \frac{12.5}{(d[mm])^2}. \tag{3.8}$$

Meanwhile, the authors claim, that in practice one should achieve pressures not higher, than 0.8 p_{max} in order to avoid a DAC brackage.

3.3. DAC preparation for measurements

Before high-pressure PL measurements to be started, one has to prepare the DAC and load the sample. These procedures are fulfilled in the following consecution.

1. Checking the parallel and axial alignment of the diamonds.

The operation is done with the closed DAC without metal gasket. The diamonds, touching culet-to-culet are observed via the optical microscope, while the DAC bottom is illuminated with the white light. First, the axial alignment is achieved, while correcting the upper diamond position with three screws, placed in the brass DAC mounting. The correction is considered to be complete, if the overlapping images of both culets have a round shape. Second, a parallel alignment is achieved, while observing the interference fringes, created between the culet surfaces. No fringes mean the best parallel alignment and at this point the DAC is ready for the loading the gasket with the sample.

2. Gasket preparation.

A metal gasket has to be previously squeezed in the DAC during 3-4 approaches almost up to the maximum pressures, applied during the measurements. Each squeezing has

to be made with the following measuring of the foil width in the diamond-shaped indentation. As a result of this process a gasket will have a diamond-shaped hollow, (70…90) μm wide. The less this width is, the higher pressure values one can achieve during the experiment. In the center of the indentation a little hole in diameter 0.25 mm, equals about 1/3 of the diameter of cullet, has to be drilled. The hole walls and the diamond culets form the high-pressure sell.

3. Loading of the sample and the pressure sensor.

A cullet has to be covered with the prepared gasket, faced towards the diamond with the same surface which touched the cullet during the preliminary squeezing. A sample, polished up to ~25 μm in thickness and slivered up to ~120 μm in length and width is placed into the cell together with the pressure sensor – tiny ruby balls, around (10–20) μm in diameter. Then the DAC is closed and observed through the microscope – to control the position of the sample and ruby, which should be located in the center of the gasket hole.

4. Filling the DAC with compressing medium.

Having been loaded, the DAC is mounted into a special holder for applying pressure for the sample via a liquid pressure medium. Methanol-ethanol mixture (with or without water) [103,104], oil or different condensed gases: He, Ne, Ar, Xe, H_2, N_2, O_2 [105-109] can be applied for this purpose. In the case of the experiments described in this Thesis, liquid argon was used, being supplied into the DAC via a special setup shown schematically in Fig.16.

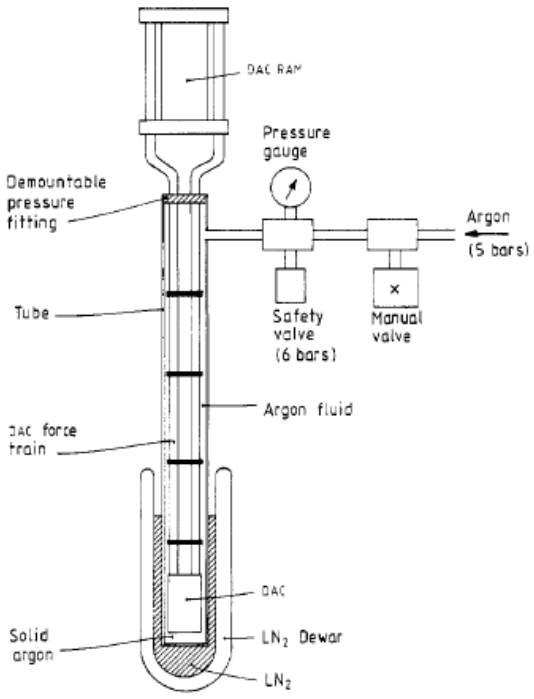

Fig. 16. A schematic view of the apparatus, used for filling of the pressure media into the DAC (after [110]).

While having diamonds not closely abut on the gasket, the DAC in the holder is placed into the tube, which is then closed hermetically. An air is pumped out from the tube with the following filling it with argon up to the pressure of 5 bar. This process is repeated for several times in order to achieve pure argon in the tube. Gas inflow and outflow should be done very slowly to prevent the movement of the sample inside the DAC. Finely, argon is left in the tube under the pressure of 5 kbar and the dewar (Fig.16) is slowly filled with liquid nitrogen. Since the argon boiling point is 10 degrees higher, than that of nitrogen [111], the argon in the tube is condensed up to the level of the nitrogen in the dewar. When the dewar is full, the DAC should be closed hermetically, using the external hydraulic system. In this case a pressure of about 35 bar is applied to the diamonds in order to prevent argon outflow during the tube heating. After the dewar is taken away, the tube has to be heated up to the room temperature in a natural way, without use of any external warming devices. As it was empirically observed, an accelerated heating of the tube can result in partial argon outflow from the DAC. Besides, taking DAC off the tube can result in water vapor condensation on the external diamond surfaces with further adhering of micro motes, being in the air.

3.4. DAC pressure sensors

3.3.1. Traditionally used pressure sensors

An ideal pressure sensor, used in the DAC during PL measurements has to be characterized by the following features [112,113].

1. High PL intensity and linear pressure sensitivity in the wide pressure range.
2. A weak temperature shift of the signal in the wide temperature range.
3. A small linewidth and little or no surrounding background.
4. The stability of the ambient crystal structure at high pressure.
5. "Tunability", i.e. a possibility to be used at different wavelengths – in the same spectral range with the emission of the sample, however a sensor signal should not overlap with the measured spectra.

The first fruitful attempt in searching of a perfect pressure sensor was made by Forman et al. in 1972 [114]. He has shown, that ruby ($Al_2O_3:Cr^{3+}$) *R*-lines [R_1=694.2 nm (14406 cm^{-1}) and R_2=692.7 (14437 cm^{-1}), a stronger and a weaker one, respectively] shift linearly with the hydrostatic pressure and broaden, if the ruby undergo nonhydrostatic stresses. It has also been reported, that the redshift of R_1 line is linear up to 195 kbar and the ruby pressure coefficient is −0.77 cm^{-1}/kbar [115]. This value turned to be constant with an accuracy of 5% for a wide temperature interval: T=(4–300) K [116]. Besides, while measuring an intensity ratio of R_1 and R_2 lines, one has to estimate the temperature inside the DAC with an accuracy of 1 K in the temperature range of T=(10–100) K [117]. Thus, a possibility to control pressure, temperature and hydrostatic conditions in the DAC makes ruby a very convenient sensor for high-pressure measurements [116,118-120].

Meanwhile, in high pressures and temperatures the *R*-lines of ruby reveal broadening and decrease in intensity, what makes it impossible to identify the pressure precisely [117]. This problem led to searching of new pressure sensors, based on the PL measurement principle. Table 5 contains the most important parameters of the materials, which can be considered as PL pressure sensors. (For the convenience all the values were recalculated in different units of measurement – nm, cm^{-1}, eV). One can notice, that $Cr^{3+}:YAlO_3$ pressure sensor is characterized by the highest sensitivity, as it has the largest pressure coefficient. Promising candidates for such applications were reported various lanthanide ions, hosted in different lattices [121-126]. As it follows from Table 5, $Cr^{3+}:YAlO_3$ is the only pressure sensor, which can compete in sensitivity with ruby. Meanwhile, the lanthanides reveal smaller

Table 5. Basic parameters of various luminescence pressure sensors, operable in the visual spectral range (after [126]).

Material	PL peak position at ambient pressure, cm^{-1}; **nm**; *eV*	$\frac{d\lambda}{dp}\left(\frac{dE}{dp}\right)$, cm^{-1}/kbar; **nm/kbar**; *meV/kbar*	$\frac{d\lambda}{dT}\left(\frac{dE}{dT}\right)$, $cm^{-1}/10^3K$; **nm/10³ K**; *meV/10³K*	$\frac{d\lambda}{\Gamma dp}$, **kbar⁻¹** [a]	$\frac{d\lambda/dT}{d\lambda/dp}$, **kbar/10³K**	Transition	Ref.
Cr^{3+}:Al_2O_3	14405.07 **694.2** *1.786*	0.757 **0.365** *0.094*	139.74 **6.8** *17.325*	**0.049**	**186**	$^2E\rightarrow{}^4A_2$, doublet	[127]
Cr^{3+}:$YAlO_3$	13835.09 **722.8** *1.715*	1.339 **0.7** *0.166*	143.96 **7.6** 17.849	**0.07**	**109**	$^2E\rightarrow{}^4A_2$, doublet	[127]
Eu^{3+}:LaOCl	17280.11 **578.7** *2.14*	0.746 **0.25** *0.093*	(-14.94) [b] [c] **(-0.5)** *(1.853)*	**(0.1)**	**(20)**	$^5D_0\rightarrow{}^7F_0$, singlet	[124]
Eu^{3+}:LaOBr	(17301.04) **(578)** [b] *(2.145)*	(0.898) **(0.3)** *(0.111)*	(-14.98) [c] **(-0.5)** *(1.857)*	**(0.1)**	**(17)**	$^5D_0\rightarrow{}^7F_0$, singlet	[125]
Eu^{3+}:YAG	16931.93 **590.6** *2.099*	0.565 **0.197** *0.07*	-14.35 [c] **-0.5** *1.77876*	**(0.07)**	**25**	$^5D_0\rightarrow{}^7F_1$, doublet	[122]
Sm^{3+}:YAG	16186.47 16231.13 **617.8** **616.1** *2.007* *2.012*	0.780 0.600 **0.298** **0.228** *0.097* *0.075*	5.24 2.63 **0.2** **0.1** *0.64947* *0.32658*	**0.023** **0.02**	**7** **4**	?$\rightarrow{}^6H$, multiplet	[123]
Sm^{2+}:SrB_4O_4	14590.02 **685.4** *1.809*	0.543 **0.255** *0.067*	-2.129 **-0.1** *0.26396*	**0.17**	**4**	$^5D_0\rightarrow{}^7F_0$, singlet	[121]
Sm^{2+}:BaFCl	14543.34 **687.6** *1.803*	2.323 [c] **1.1** *0.288*	-33.92 **-1.6** *4.20558*	**0.48**	**15**	$^5D_0\rightarrow{}^7F_0$, singlet	[126]
Sm^{2+}:SrFCl	14486.46 **690.3** *1.796*	2.305 [c] **1.1** *0.286*	-48.43 **-2.3** *6.00437*	**0.58**	**21**	$^5D_0\rightarrow{}^7F_0$, singlet	[126]

[a] Γ – is a linewidht.

[b] The values in parentheses are estimated.

[c] Different values of $\frac{dE}{dp}$ correspond to the same ones of $\frac{d\lambda}{dp}$ (presented in bold print), as in the re-calculation of the measurement units, different positions of the PL peak of the sensor at ambient pressure was taken into account. The same concept was assumed during the $\frac{d\lambda}{dT}$ into $\frac{dE}{dT}$ unit recalculation.

temperature coefficients, as compared with ruby, so, they can be operable in the high-temperature conditions. Thus, Sm^{3+}:YAG as well as Sm^{2+}:SrB_4O_7 pressure sensors, which have the smallest $\frac{d\lambda}{dT}$ and $\left(\frac{d\lambda}{dT}\right)\Big/\left(\frac{d\lambda}{dp}\right)$ coefficients, can be used in the high-stress measurements, taken at temperatures up to 700 K [126].

All pressure sensors, listed in the Table 5 are operable in the visible spectral range. H.Hua and Y.K.Vohra have reported first that room-temperature emission spectra of neodymium-doped yttrium aluminum perovskite (Nd^{3+}:$YAlO_3$) in the near-infrared spectral range reveals several lines associated with Nd^{3+} $^4F_{3/2} \rightarrow {}^4F_{9/2}$ transitions [113]. These lines undergo blueshift with pressure and two of them, centered at 866 and 875 nm (1.43169 and 1.41696 eV respectively), meet almost all the criteria of an ideal emission pressure sensor in the range (0–800) kbar.

Recently S.Kobyakov et al. have shown, that neodymium-doped yttrium aluminum garnet crystal (Nd^{3+}:YAG) can also be used as a DAC pressure sensor operable at the wavelengths around 950 nm (1.31 eV) in the pressure and temperature ranges (0–120) kbar and (10–300) K respectively [128].

3.3.2. Problem led to the search of new pressure sensors

High-pressure PL measurements, performed in the framework of the experimental part of this Thesis were carried out in the spectral range (900÷2500) nm [(0.49÷1.38) eV]. For this purpose Judson J13TE2 PbS photoconductive detector was applied, which has the highest spectral response in the range (1–3) μm. Ruby, being used as a pressure sensor, emits, in turn, red light at about 695 nm and can not be registered with the PbS detector.

Because of the dispersion of lenses, used in the experimental setup, the process of the high-pressure PL measurements which involve taking signal in visible range and infrared by turns, usually includes numerous precise alignings of the optical system. In our case the PL measurements at each pressure point are performed according to the following algorithm.

1. Focusing the laser beam on the pressure sensor (ruby) and aligning the optical setup, using *a detecting system, operable in the visible spectral range* (in our case – Ocean Optics High-Resolved Spectrometer HR 4000).

2. Taking the emission spectrum of the pressure sensor (ruby).
3. Focusing the laser beam on the sample and aligning the optical setup with *another detecting system, operable in infrared* (in our case – PbS detector).
4. Taking PL spectrum of the sample and re-focusing the laser beam on the pressure gauge (ruby).
5. While observing the position of the PL peak of the ruby, increasing pressure in the DAC until the required value achieved. (This process also usually results in the misaligning of the ruby balls from the focused laser beam).

In this algorithm the first step is the most complicated one, as it consists in the guiding of a very weak signal, coming from tiny ruby balls (and then reflected from a tilting mirror) into a thin optical fiber connected with the Ocean Optics High-Resolution Spectrometer (Fig.17). This procedure demands special operator's skills and is usually very prolonged. Therefore, a complete measurement of the sample (taken at more, than 10 pressure values) becomes very time-consuming as well.

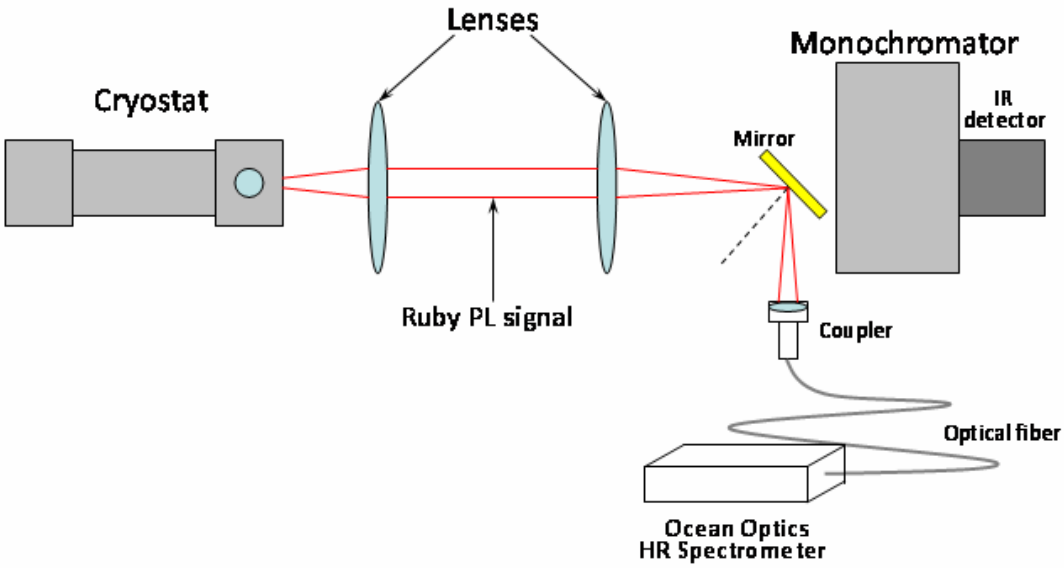

Fig. 17. A schematic view of taking PL signal from the ruby balls (pressure sensors), with the use of tilting mirror, which is taken away, when infrared PL of the sample is measured. (The picture corresponds to the steps 2 and 3 of the above mentioned algorithm).

Besides, the precision of the high pressure measurements, described in this Thesis might also be increased, as it is limited at least by 2 factors:

– the ruby pressure coefficient value;
– broadening of the ruby linewidth with stress.

Thus, if there was a possibility to calibrate a new pressure sensor, which would be more precise and operable in the same spectral range with the studied sample, the entire time of the high-pressure PL measurements along with a measurement error would significantly decrease. This idea was the main motivation for seeking of a new pressure sensor, operable in the infrared.

3.3.3. InP-based crystals, alloys and quantum heterostructures

During last 30 years numerous papers were published about high pressure optical studies of III-V semiconductors, but InP-based materials ranked high among the reported compounds. High-pressure PL measurements of undoped *bulk* InP samples were performed first at room [129-131] and later at liquid helium temperatures [132]. This material is characterized by the energy gap equals 1.35 eV at T=300 K and 1.42 eV at T=0 K. It was found, that an intense emission peak, corresponding to the direct-band-gap transition underwent a sublinear blueshift with pressure, and this behavior was similar both at room and at liquid-helium temperature. It was also shown, that the dependence of the peak position E(eV) on pressure p(kbar) could be fitted with the following quadratic equation [129,132]:

$$E_{PL\ peak} = E_0 + Bp + Cp^2, \tag{3.9}$$

where:

– E_0 is a PL peak positition at ambient pressure;

– B=(7.5±0.2) meV/kbar; C=(−1.2±0.5)·10^{-2} meV/kbar^2 for T=20 K;

– B=(8.4±0.2) meV/kbar; C=(−1.8±0.3)·10^{-2} meV/kbar^2 for T=300 K.

S.W.Tozer et al. reported about further high-pressure investigations of InP in comparison with $Ga_xIn_{1-x}P$ (x=0.17, 0.36, 0.54) *alloys* [133]. The latter samples revealed donor-bound-exciton and donor-acceptor pair recombination, which resulted in nonlinear change of the direct band edge with pressure. This dependence could also be fitted with the function (3.9), which has similar parameters as in the InP case: B=8.3 meV/kbar, C=3.01·10^{-2} meV/kbar^2. The crossing of conduction band minima Γ and X in the case of $Ga_xIn_{1-x}P$ alloys is observed at lower pressures compared to InP (even at $p_{\Gamma-X} = 20\ kbar$ for x_{Ga}=0.54), as with increasing of Ga-mole fraction the direct gap opens and low pressures are needed to achieve band crossing. The extrapolation of the dependency of Ga mole fraction on

Γ–X crossover pressure made it possible to estimate the $p_{\Gamma-X}$ value for pure InP which was found to lie above 120 kbar.

While considering InP and GaInP alloys for the usage as DAC pressure sensors, described in the Section 3.3.2, one should notice, that there are two disadvantages, which restrict such application. First, both sensors could not be operable in the infrared spectral range. Second, due to crossing of Γ and X conduction band minima at stress values $p > p_{\Gamma-X}$ the PL intensity of GaInP alloys decreases exponentially and the sign of the pressure coefficient changes [133]. This feature makes impossible to use a pressure sensor at stresses, exceeding $p_{\Gamma-X}$ value. In this sense InP sensor could be more suitable, but its working range is also limited by a very sharp and irreversible rocksalt phase transition, which takes place at $p \approx 106$ kbar.

In the quoted publications the authors' task was not to calibrate a new InP-based pressure sensor. Nevertheless, an intense PL line and extremely high pressure coefficient B of the researched structures (almost 80 times greater, than that of ruby) was remarkable. Thus, these results were a strong motivation for seeking for new III-V materials, which could be applied as effective DAC pressure sensors.

Later on a group of researchers – W.Trzeciakowski, T.P.Sosin and P.Perlin with co-authors performed optical pressure calibrations of different III-V-based *quantum structures.* Having analyzed high pressure PL and absorption behaviour of various QW samples the authors note, that InP-based quantum wells surpass GaAs-based ones [134-136], as the latter structures are characterized by low-pressure Γ–X crossover ($p \approx 40$ *kbar*) and different QW samples are to have different calibrations. The possibility to use GaAs-based structures in the infrared spectral range was not discussed.

In 1995 T.P.Sosin, W.Trzeciakowski et al. have reported about calibration of InAsP/InP quantum wells in the range of (0÷100) kbar for T=300 K and T=80 K [137]. It was found that the pressure-induced blueshift of both QW and substrate PL lines could be fitted with the equation (3.9) with the same fitting parameters: B=8.3 meV/kbar and C=0.02 meV/kbar^2. The authors stress, that the studied sample was not optimized as a pressure sensor because the higher signal intensity and smaller linewidth had not still been obtained. But nevertheless, being characterized by a high pressure coefficient and while working in the IR spectral range, InP-based quantum structures would evidently benefit as possible candidates for new pressure sensors, in particular described in the 3.3.2 Section of the present Thesis.

4. THE AIMS OF THE RESEARCH

Consequently to the state-of-the-art, concerned Cr^{2+}-doped II-VI semiconductors and the properties of actually used pressure sensors for DAC, the main aims of the present PhD research can be formulated as follows.

1. **To investigate and compare the features of vibronic and spin-orbit interactions in ZnX:Cr^{2+} semiconductors with different anion type (X=S, Se, Te) using a high-pressure PL measurements.**

   To realize this purpose high liquid-helium temperature hydrostatic pressure PL studies of ZnX (X=S, Se, Te) samples should be performed. As a result the influence of the interionic distances on the intrashell ${}^5E \rightarrow {}^5T_2$ transition of Cr^{2+} ion will be studied dependently on the anion type, embedded in the crystal. The dependence of emission in ZnX:Cr^{2+} (X=S, Se, Te) compounds on hydrostatic pressure can reinterpret the previously reported observations.
2. **To study the unidentified ZnSe:Cr^{2+} optical transition responsible for the near-infrared PL band, centered at ~1.25 eV.**

   The low-temperature high-pressure hydrostatic studies of the ZnSe:Cr^{2+} sample should be performed and the results should be analyzed on the basis of the previously described theoretical behaviour of Cr^{2+} ion energy terms with the crystal field increase.
3. **To calibrate new InP-based high-pressure sensors, operable in the infrared spectral range and being characterized with the working parameters, exceeding those of ruby gauge.**

   In order to realize this purpose one should study several InP-based multi quantum wells (MQWs), which differ with structure and, consequently, with the ambient-pressure emission line position. Temperature and excitation power dependences of PL should be studied for all MQWs in order to determine the applicability range of new sensors and their accuracy. High-pressure measurements should be performed in different temperatures in order to try to find the explicit form of the function (3.9)

   $$E_{PL\ peak} = E_0 + Bp + Cp^2,$$

   which can describe $E_{PLpeak}=f(p)$ dependencies of all the MQWs at each temperature to within the position A of the PL peak at ambient pressure. Then, these $E_{PLpeak}=f(p)$ dependencies can be used as calibration curves of new InP-based pressure sensors.

5. SAMPLES

ZnS:Cr^{2+} crystal was grown in the Lawrence Livermore National Laboratory (Livermore, USA) by the chemical vapor transport (CVT) method. Afterwards it was diffusion-doped with chromium as it was described by K. Graham et al. [138]. The sample was cut into slices, which had a shape of slightly wedged (0.4 degrees) rectangular with an area and a thickness of 5x5 mm^2 and 1 mm respectively. The crystals had a daffodil color.

ZnSe:Cr^{2+} sample was grown in the ON1 Division of Physics of Semiconductors of the IF PAS (Warsaw, Poland). Synthesized powder of ZnSe and pure Cr metal were used as source materials for ZnSe:Cr^{2+} crystal growth. The crystallization process took place at 1550 ºC in the open ampoule, filled with nitrogen gas at pressure 50 atm (5MPa). Crystallization velocity was about 1.5 mm/h. After growth the crystal was cut into slices up to 1 mm thick, which had vinous color.

ZnTe:Cr^{2+} sample was also obtained in the ON1.1 Division of the IF PAS (Warsaw, Poland). The crystal was grown, using high-pressure Bridgman technique. The Zn, Te and Cr mixture was heated up to 1400 ºC for 24 hours and melted completely. Then the ampoule was pulled through the furnace at various speeds 1.5, 2.5 and 5 mm/h. During the growth process the nitrogen pressure in the chamber was kept at about 30 atm (3MPa). The temperature gradient in the growth region was about 60 ºC/cm. When the top of the ampoule reached the temperature below 1100 ºC, the growth was finished. Afterwards the crystal was cut into slices up to 1 mm thick, which were black colored.

While being prepared for the high pressure PL measurements, all the bulk samples were polished from both sides up to ~25 μm thick and then cut with a chirurgical scalpel into pieces up to ~120 μm in length and width.

InP-based MQWs. The samples of multi-quantum wells (M1217 – InAsP/InGaP, M1342 – InAsP/InGaAsP, M1352 – InAsP/InP) were grown by MBE method in the EPSRC National Centre for III-V Technologies, University of Sheffield (Sheffield, UK). They had the structures, shown in Fig.18. The growth parameters of the quantum well are presented in Tables 6–8. For the high-pressure measurements all the samples were etched down up to ~30 μm thick. After this procedure all the samples look like identically black from both surfaces – QW and substrate ones. Thus, before the loading of a sample into the DAC the following procedure should be done. Every sample has to be divided into two pieces and glued with silver paste to the cryostat sample holder with two opposite surfaces upwards. The preliminary low-temperature PL measurements should be taken from both pieces. Then a part

of the sample, glued with quantum well surface upwards has to be taken very carefully onto the microscope slide. A drop of acetone is dripped from above gingerly to prevent the turning over the sample during its further cutting into pieces (up to ~120 μm in length and width). One piece, which is desirable to be of irregular shape, has to be loaded into the DAC. The shape of this piece should be previously drown on the paper in order to be sure, whether the sample is still being loaded into the cell with the substrate towards the culet surface.

This procedure makes it possible to save time during the experiment significantly, as it excludes the case when high-pressure measurements had already started but the sample turned out to be placed in the DAC with the substrate surface towards the excitation laser beam. (Such a situation demands unfreezing the DAC and its reloading).

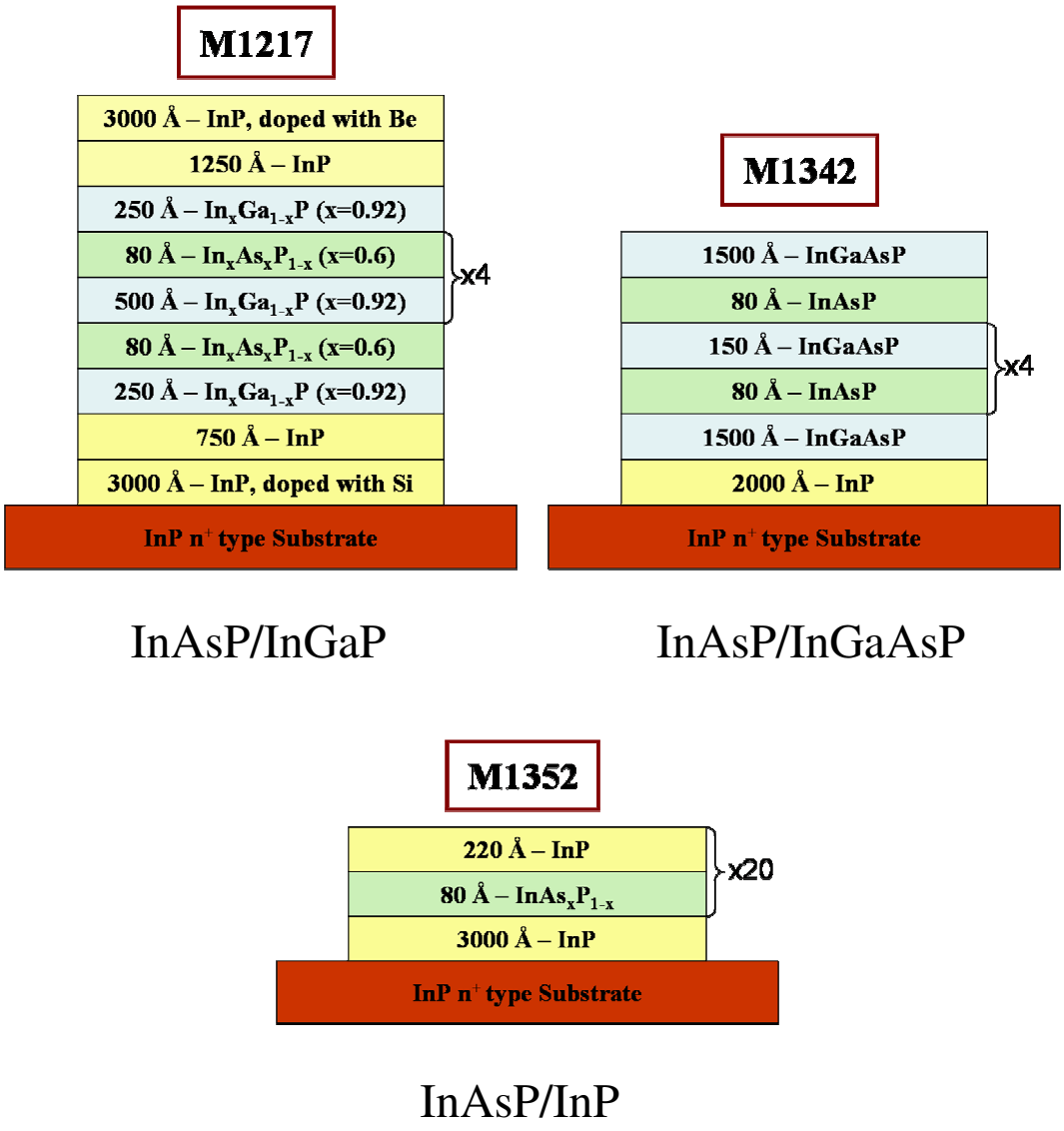

Fig. 18. A schematic view of the growth sequence of InP-based quantum structures.

Table 6. Technological growth parameters of the InAsP/InGaP (M1217) sample.

Rpt:	Thickness (Å):	Material:	T_s:	(x):	Dopant:	Type:	Conc.:
1	3000	InP	471		Beryllium	p	$2 \cdot 10^{18}$
1	1250	InP				ud	
1	250	$In_xGa_{1-x}P$		0.92		ud	
5	80	$InAs_xP_{1-x}$	459	0.6		ud	
4	500	$In_xGa_{1-x}P$	458	0.92		ud	
1	250	$In_xGa_{1-x}P$		0.92		ud	
1	750	InP	476			ud	
1	3000	InP	498		Silicon	n	$2 \cdot 10^{18}$
InP n+ Substrate							

Table 7. Technological growth parameters of the InAsP/InGaAsP (M1342) sample.

Rpt:	Thickness (Å):	Material:	T_s:	(x):	Dopant:	Type:	Conc.:
1	1500	InGaAsP	501	Unidentified (u/id)		ud	Unidentified
4	150	InGaAsP				ud	
5	80	InAsP				ud	
1	1500	InGaAsP				ud	
1	2000	InP	502		u/d	ud	
InP n+ Substrate							

Table 8. Technological growth parameters of the InAsP/InP (M1352) sample.

Rpt:	Thickness (Å):	Material:	T_s:	(x):	Dopant:	Type:	Conc.:
20	220	InP	505	Uniden-tified	undoped	ud	Uniden-tified
20	80	$InAs_xP_{1-x}$	503		undoped	ud	
1	3000	InP	503		undoped	ud	
InP n+ Substrate							

6. EXPERIMENTAL RESULTS AND DISCUSSIONS

6.1. Preliminary (ambient pressure) optical studies of ZnX:Cr^{2+} (X=S, Se, Te) crystals.

Absorption. The absorption spectra of all ZnX :Cr^{2+} (X=S, Se Te) crystals were taken with the use of Cary 5000 UV-Vis-NIR Spectrophotometer at T=300 K. All the samples were about 1 mm thick and polished carefully before measurements from both plane-parallel sides. The results of the absorption measurements are shown in Fig. 19. The peaks of absorption bands are centered at about 0.73, 0.70 and 0.69 eV (5900, 5650 and 5600 cm^{-1}) for Cr-doped ZnS, ZnSe and ZnTe crystals respectively, what corresponds to the values, given in the literature [5,70]. These bands are associated with $^5T_2 \rightarrow {}^5E$ optical transition (Fig. 20 (b)).

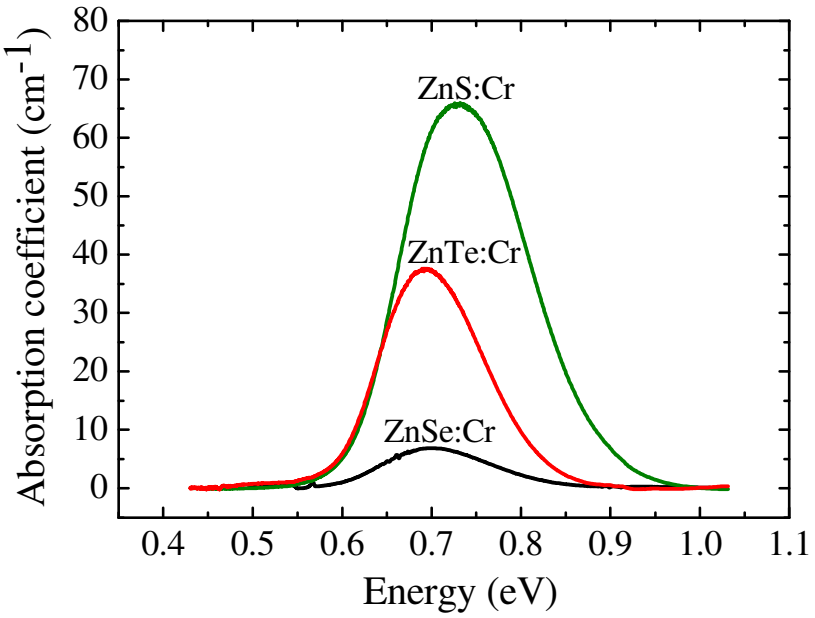

Fig. 19. Room-temperature absorption spectra of ZnX:Cr^{2+} (X=S, Se, Te) samples.

The different absoption peak intensities are due to the different chromium dopant concentration in the studied samples, which can be estimated via the relation [139]:

$$\alpha = n\,\sigma\ . \qquad (6.0)$$

Here σ is the absorption cross-section related to the absorption coefficient α at a single frequency for n number of atoms per unit volume. At room temperature the absorption cross-section values for Cr-doped ZnSe, ZnTe and ZnS were reported to be $8.7\cdot10^{-19}$ cm^2,

$1.23 \cdot 10^{-18}$ cm^2 and $5.2 \cdot 10^{-19}$ cm^2 relatively [140]. Thus, taking into account the maxima of the aborption coefficient (Fig. 19), one can estimate, that the chromium dopant concentration is $7.9 \cdot 10^{18}$ cm^{-3}, $3.1 \cdot 10^{19}$ cm^{-3} and $1.3 \cdot 10^{20}$ cm^{-3} for ZnSe:Cr, ZnTe:Cr and ZnS:Cr sample respectively.

Photoluminescence. Ambient pressure PL studies were performed at liquid-helium temperature.

First "thick" and then "thin" samples (grinded and polished up to ~1 mm and ~25 μm thickness respectively) of ZnX:Cr (X=S, Se, Te) compounds were used to carry out preliminary PL measurements. ("Thin" crystals are studied to estimate, whether PL signal intensity is high enough to use the sample for the further high-pressure measurements).

Emission spectra of **ZnA:Cr (A=S, Se)** crystals were excited by the 514.5 nm and 488 nm argon-laser lines and measured using Lomo MDR-2 Monochromator, Hamamatsu (P819) solid CO_2-cooled PbS detector and a 7265 DSP EG&G Instruments Lock-in amplifier.

PL spectra of both samples reveal a broad band associated with $^5E \rightarrow {}^5T_2$ intrashel transition (Fig. 20 (a)). Due to Jahn-Teller effect the band is split into two subbands centered at about 0.557, 0.62 eV (ZnS:Cr^{2+}) and 0.535, 0.584 eV (ZnSe:Cr^{2+}).

Ambient-pressure **ZnTe:Cr^{2+}** spectra were excited with the same laser and lines and measured with the use of DIGIKROM 240 monochromator equipped with a Judson J13TE2 thermoelectrically cooled PbS detector and a SR 530 model Standford Research lock-in amplifier.

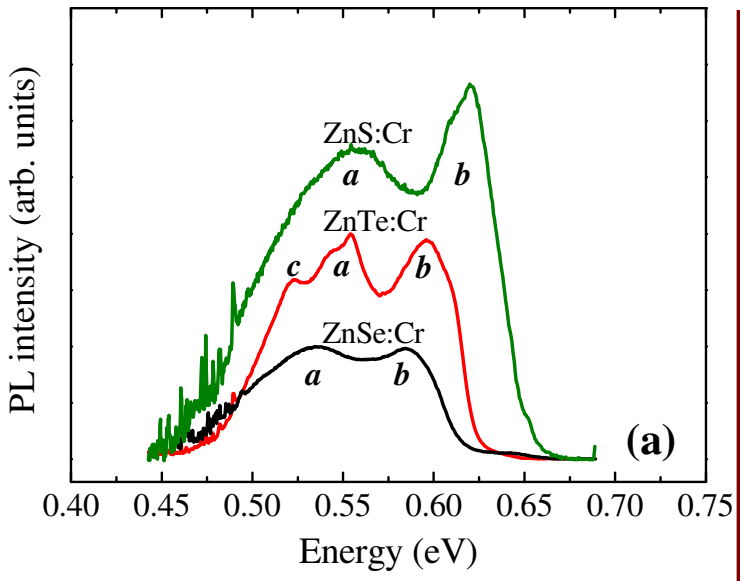

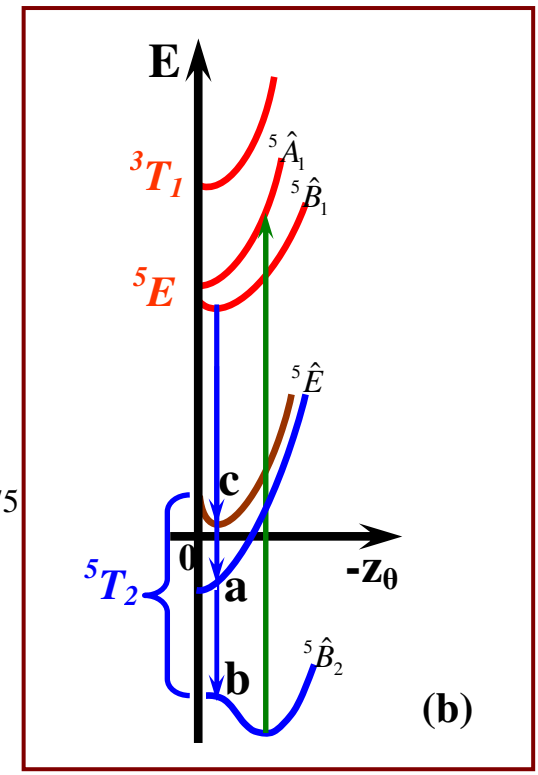

Fig. 20. Low-temperature PL spectra of ZnX:Cr (X=S, Se, Te) samples at ambient pressure (a); and schematic illustration of the transitions, responsible for the observed PL spectra and absorption band (b).

As one can see in Fig. 20 (a), as well as in the case of ZnA (A=S, Se) spectra, the PL band of ZnTe:Cr^{2+} sample also characterized with a $^5E \rightarrow {}^5T_2$-associated broad band, but consisting of three subbands centered at about 0.523, 0.553 and 0.596 eV and being a consequence of combine effect of Jahn-Teller splitting and spin-orbit coupling. Schematic illustration of the energy transitions, responsible for the observed absorption and PL spectra (in the approach of M. Kamińska et al. [4]) is presented in Fig. 20 (b). One can notice that the shape and peak positions of all the PL bands are in a good agreement with the experimental data, reported in the literature and described in the 2.2.4 Section.

Ambient-pressure low-temperature PL measurements of **ZnSe:Cr^{2+} sample in the range of 1.25 eV** were carried out with the use of liquid-nitrogen cooled S1-type EMI 9684B photomultiplier tube (Fig. 21). The spectra were excited by 514.5 nm of argon-ion laser.

A zero-phonon line with a peak at 1.328 eV revealed on the "thick" sample, but was not observable on the "thin" one. Such an effect can be explained by the significant broadening of the ZPL line, which is a consequence of the following factors:

– deficient amount of Cr^{2+} ions in the "thin" sample for the zero-phonon line to be registered with the applied detecting system;

– one-axis deformation effects, which may occur in the "thin" sample, as a result of being glued with a silver paste before measurements [141].

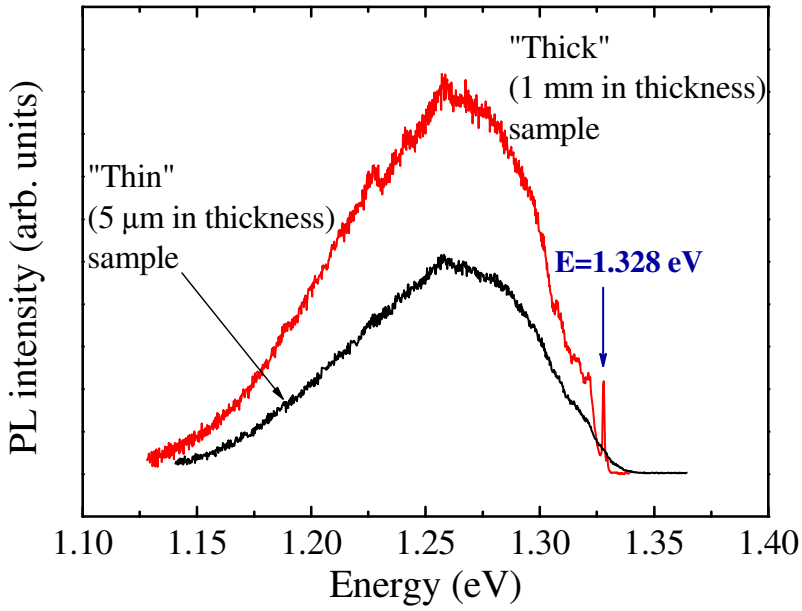

Fig. 21. Ambient-pressure PL spectra of the "thick" and "thin" ZnSe:Cr samples taken at T=10 K.

6.2. High-pressure ZnX:Cr^{2+} (X=S, Se, Te) studies

Preliminary ambient pressure studies were followed by high-pressure measurements performed using a Diacell Products MCDAC-1 diamond anvil cell. It was mounted into an Oxford 1204 cryostat equipped with a temperature controller for low temperature measurements. For each sample the same equipment and excitation were used, as in the case of preliminary ambient-pressure studies outlined in the previous 6.1 Section. All the measurements of ZnX (X=S, Se, Te) crystals were taken at T=10 K. The obtained spectra were corrected for the quantum efficiency of the system.

The hydrostatic conditions were monitored by recording of the full width at half minimum (FWHM) of the ruby emission. The increase of the linewidth of R_1 ruby line with stress growth was observed in the measurements, however, for the pressure values about 100 kbar the FWHM did not exceed 5 cm^{-1}. (At ambient pressure FWHM is about 2.5 cm^{-1}; 1 meV = 8.065 cm^{-1}). It means that the non-hydrostatic effects were rather weak.

6.2.1. ZnS:Cr^{2+} high-pressure PL

High-pressure PL of ZnS:Cr^{2+} sample was studied in (0÷83.3) kbar stress range (Fig. 22). One can see, that the shape of the band is almost independent of the applied pressures.

The observed spectra can be qualitatively interpreted, using the schematic configuration coordinate diagram for the ^5E and $^5T_2$ states, proposed by M. Kamińska et al. [4] and shown in Fig. 20 (b). Here the “a”, “b” and “c” transitions correspond to three subbands, usually observed in the PL spectra of Cr-doped II-VI semiconductors. In the case, when spin-orbit coupling is absent, the ground terms of the “c” and “a” transitions coincide, and the parabolas, standing for $^5E(^5T_2)$ and $^5B_2(^5T_2)$ terms cross in “0” point in the configuration coordinate diagram, as it is shown with a dashed curve in Fig. 13.

The PL band of ZnS:Cr crystal, being associated with $^5E \rightarrow {}^5T_2$ transition does not reveal the features, arguing about the presence of experimentally observable spin-orbit coupling of the $^5T_2$ term. The “c” transition (Fig. 20 (b)) practically does not reveal itself as a separate subband neither at low nor at high pressures. And the peak marked as “c+a” in Fig. 22 (a) thus, can be assumed as a sum of two very closely located subbands, responsible

for ”c” and “a” transitions shown in Fig. 20 (b)), which arise from the combined Jahn-Teller effect and extremely weak spin-orbit coupling.

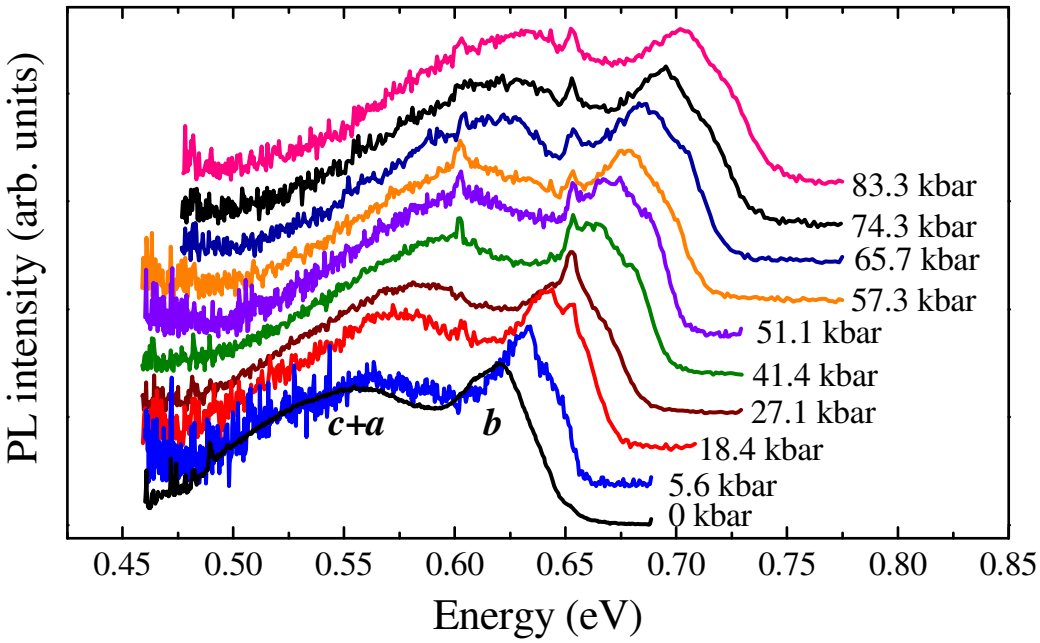

Fig. 22. Pressure dependence of ZnS:Cr PL band, taken at T=10 K.

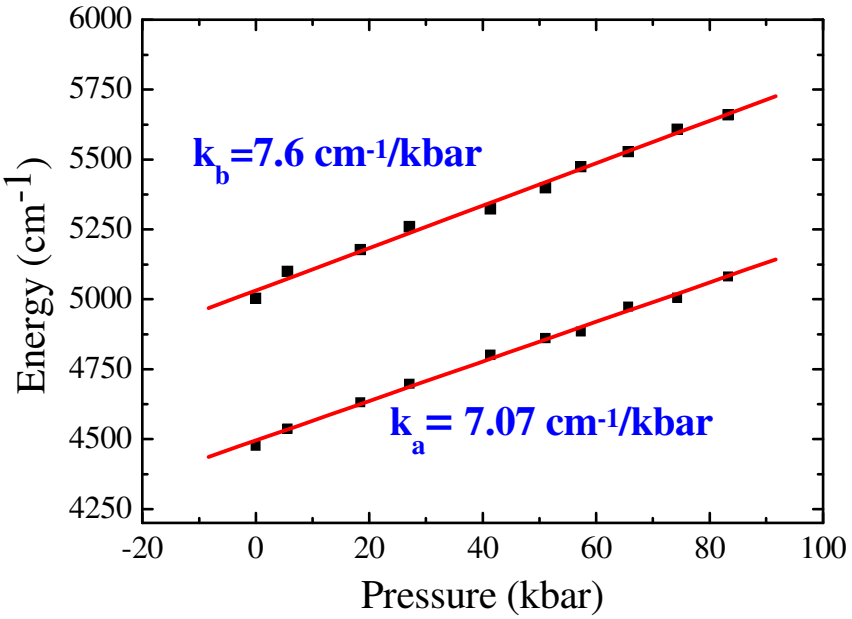

Fig. 23. Pressure dependencies of the spectra position of Cr^{2+} PL maxima in the ZnS:Cr crystal at liquid-helium temperature.

Fig. 23 presents the pressure dependences of the spectral position of Cr^{2+} PL maxima in the ZnS:Cr crystal. It is seen, that the peaks shift nearly linearly with stress increase, and the pressure coefficients were found to be about 7.1 and 7.6 cm^{-1}/kbar for "a" and "b" subbands respectively.

Taking into account, that JT effect is approximately pressure-independent (both pressure coefficients k_a and k_b are almost equal), and the spin-orbit interaction is not evinced on the PL band at high-pressure conditions, one can assume the following.

1. The spin-orbit coupling in Cr-doped ZnS crystals is extremely weak.
2. The hybridization of electron shells of the central and ligand ions does not result in the spin-orbit parameter λ change.

Thus, the approach of *S* ligand to *Cr* central atom does not result in the increase of the combined effect of Jahn-Teller distortion and spin-orbit coupling. Further (6.2.2 and 6.2.4 Sections) it will be shown, the effect of high-pressure conditions on the PL properties of ZnS:Cr sample turned out to be the weakest one in comparison with the other Cr-doped ZnSe and ZnTe samples.

6.2.2. High-pressure PL of ZnSe:Cr^{2+} (0.6 eV band)

The photoluminescence band centred at 0.6 eV were investigated within (0÷80) kbar pressure range (Fig. 24). The two-humped band (with "a" and "b" subbands) evidently belongs to the $^5E \rightarrow {}^5T_2$ transition, which in ZnSe:Cr was investigated in details by M. Kamińska *et al.* [4]. In addition, a variation of the d-orbital energy of JT distorted T_d complexes was studied also by R. Valiente and F. Rodriguez [142]. It has been reported, that both $^5T_2$ and ^5E terms exhibit the Jahn-Teller (JT) effect and the value of JT energy ε_{JT} was extracted from the line shape fit to observed spectra. (As it was already mentioned in 2.2.4 Section, the JT energy of the $^5T_2$ ground state was deduced to be $\varepsilon_{JT}(^5T_2)$ = 340 cm^{-1} and the JT interaction in the excited ^5E state, was found to be much smaller: $\varepsilon_{JT}(^5E)$ = 40 cm^{-1} [4]). Besides, while comparing the Cr^{2+} spectra in ZnS, ZnSe and CdTe, it has been shown that in ZnSe the spin-orbit splitting of the $^5T_2$ term is negligible. This was explained by the particular ratio of the admixture of ligand *p* function to the *d* function [4].

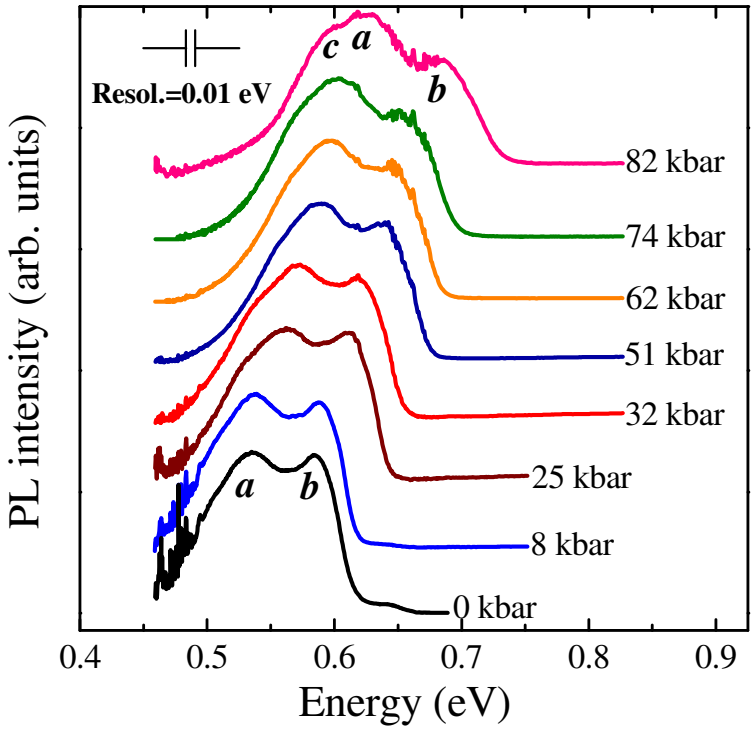

Fig. 24. Pressure dependence of the liquid-helium ZnSe:Cr PL band centered at 0.6 eV.

But a more detailed inspection of the result of high-pressure PL measurements shows that at higher pressure an additional subband "c" appears at the low energy side of the

spectrum (Fig. 24). At 82 kbar, this extra subband centred at energy of about 0.58 eV, in addition to two other peaks at 0.62 eV and 0.68 eV. Fig. 25 shows pressure dependencies of the spectral positions of the Cr^{2+} luminescence maxima in the ZnSe:Cr crystal at low temperatures. From this graph follows that the energy maxima of "a" and "b" subbands increase nearly linearly with increasing pressure. The pressure coefficients of these maxima equal to about 8 cm^{-1}/kbar and are similar with those for ZnS:Cr sample.

One has take into account, that in a standard CF point charge model, the ${}^5E \rightarrow {}^5T_2$ transition energy depends only on the cubic CF parameter Δ and it is given (in CGS units) as [12]:

$$\Delta = 10Dq = \frac{10}{6} Z \frac{e^2 < r^4 >}{R^5} \qquad (6.1.)$$

where:

– R is the interatomic distance between Cr and Se ions approximated by the Zn–Se separation;

– $< r^n >$ can be obtained by the expression $< r^n >= \int R_{3d} r^{n+2} dr$;

– Ze is the charge of the ligand ion.

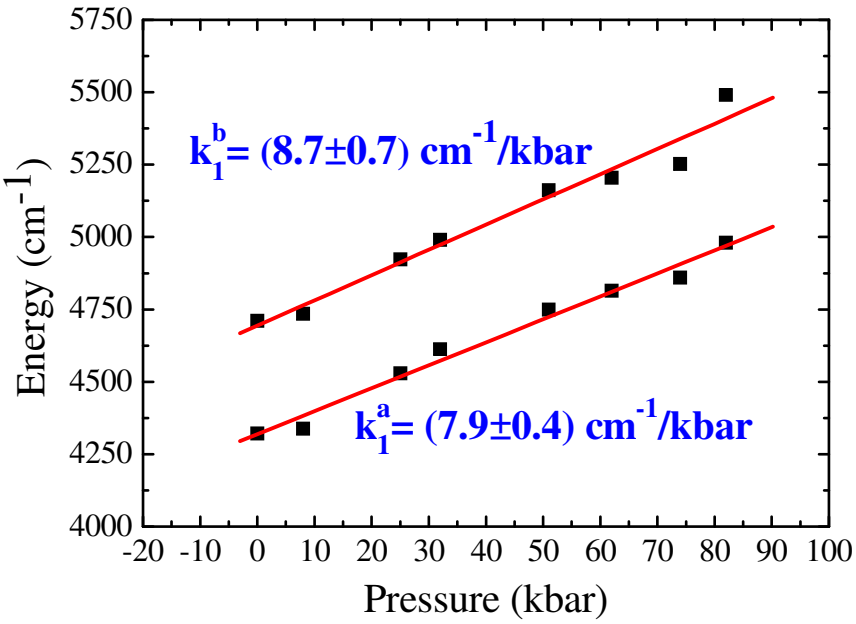

Fig. 25. Pressure dependencies of the spectra position of Cr^{2+} PL maxima of the ZnSe:Cr crystal at liquid-helium temperature.

Hydrostatic pressure reduces the distance R and then Δ can be scaled from the value for ambient pressure using the Murnaghan scaling factor [143]:

$$\frac{R_0}{R_p} = \left(\frac{pB_0'}{B_0} + 1 \right)^{\frac{1}{3B_0'}}, \tag{6.2}$$

where B_0 = 624 kbar is the bulk modulus and B'_0 = 4.77 is its pressure derivative for ZnSe crystal [144,145]. The calculated pressure dependencies of interatomic distance changes ΔR and changes of the cubic CF strength parameter ΔDq are shown in Fig. 26.

The change of Dq is slightly bow-shaped. Further on, this dependence was approximated as linear. Therefore, as it is seen from Fig. 26, the pressure coefficient of Dq is close to 8 cm^{-1}/kbar, what is in a good agreement with the pressure coefficients of "a" and "b" components of the 0.6 eV band.

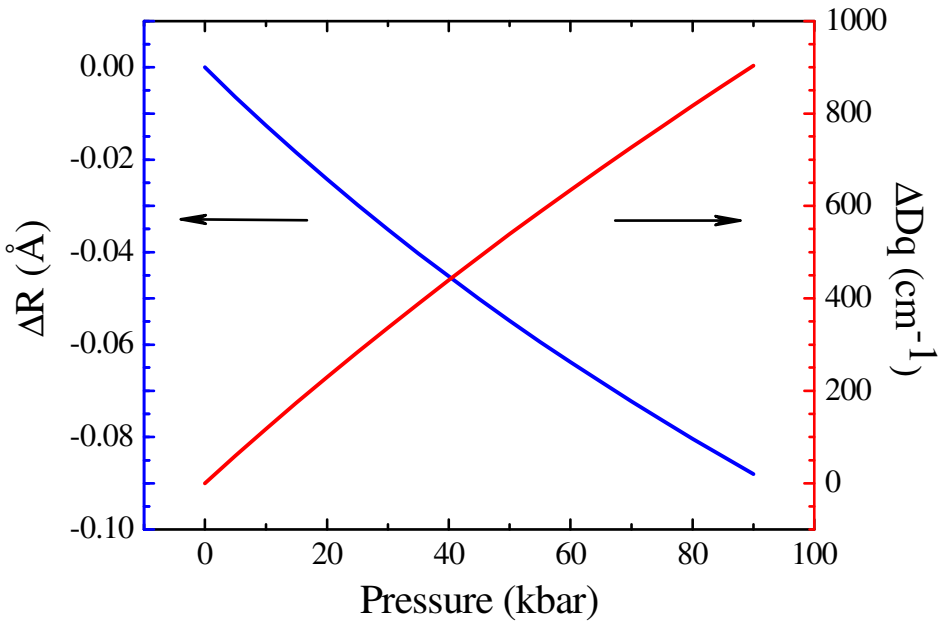

Fig. 26. The calculated changes of *R* and *Dq* with pressure.

The transition between the ground and the first excited term is accompanied with the conversion of one *e* electron by the energy 10*Dq*. The conventional Tanabe-Sugano diagrams [12] show the CF term energies for a particular value of the crystal-field strength parameter *Dq*. The Tanabe-Sugano diagram for the lowest six CF terms of the d^4 electronic configuration in a tetrahedral CF is shown in Fig. 27.

According to the theoretical ideas, presented in 2.1.2 Section of the Thesis, the energy surface of the ^5E term has the form of a "Mexican hat". The ground sublevels of the $^5T_2$ term are split. This splitting is determined by the equilibrium position of the ^5E term on the coordinate configuration diagram. Since the estimation based on the CF theory suggests

different tetragonal coupling constants for both terms the observed energy distance of 380 cm^{-1} is not equal to the splitting $3E_{JT}$ of the $^5T_2$ term at its equilibrium deformation. The energy value of $3E_{JT}$ obtained from the direct absorption between sub-levels of the $^5T_2$ term is 3-4 times larger. The ligand displacements from the equilibrium position is proportional to the electron-lattice coupling constant while the JT splitting to the square of this constant. Taking into account these peculiarities, one can find that the equilibrium displacement of the ligands for the ^5E term is approximately equal to half of that for the $^5T_2$ term.

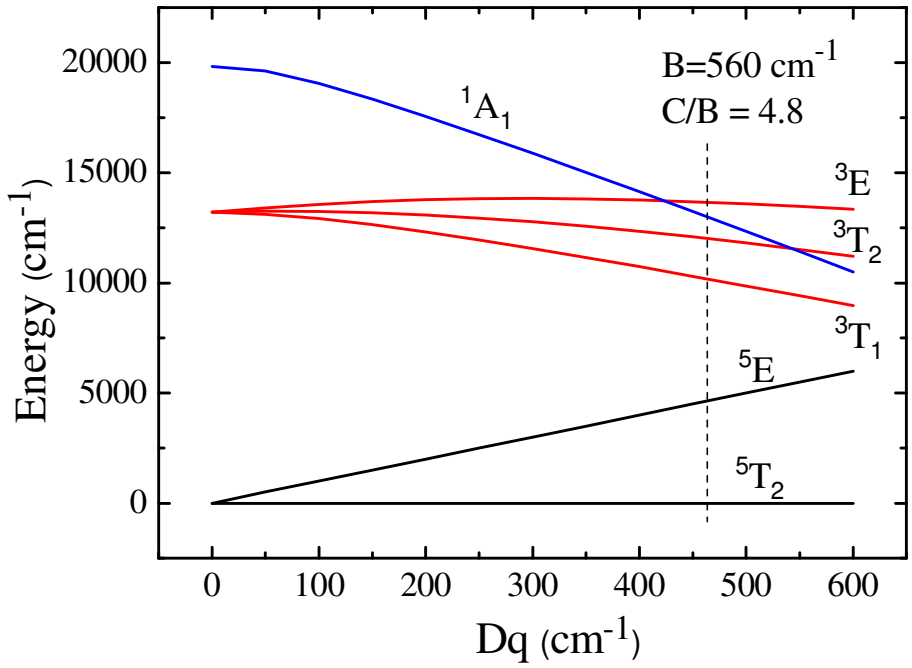

Fig. 27. The Tanabe-Sugano diagram for the six lowest CF terms of the d^4 configuration in a tetrahedral crystal field.

The luminescence shows broadening not only due to rotation about the tetragonal axis for the ^5E term but also due to the breathing vibration around the equilibrium position which influences directly $10Dq$. The amplitude of such vibration can be estimated from the relation $kQ_b^2 \approx h\omega$. Taking $h\omega = 300$ cm^{-1} one can obtain that the maximal amplitude is ΔR~0.05Å. Therefore the total shift for inside and outside motion around the equilibrium is about 0.1 Å. As it is shown in Fig. 26, the shift of $\Delta R \approx 0.05$ Å is equivalent to the application of pressure equals 50 kbar. The corresponding shift at the value of Δ10Dq is about 500 cm^{-1}. Thus, the thermal vibration of ligands around their equilibrium causes harmonic oscillation in the average value of $10Dq$ of about 500 cm^{-1}.

Hydrostatic compression leads to a decrease of R and, hence, an increase of cubic CF. It is clearly seen in Fig. 24 and Fig. 25, where both peaks of the 0.6 eV emission show positive pressure coefficients equal to about 8 cm^{-1}/kbar. Certainly, hydrostatic pressure does not change the site symmetry of the centre, but it can change the amplitude of tetragonal distortion.

A more accurate description of the ${}^5E \leftrightarrow {}^5T_2$ optical transitions of Cr^{2+} ions in II-VI compounds requires taking into account both Jahn-Teller and spin-orbit interactions [4]. Accidentally, at ambient pressure the spin-orbit interaction parameter is very small for ZnSe:Cr^{2+}, however it is not equal to 0, as far as for the other *Cr*-doped II-VI compounds it results in the splitting of the ${}^5E \rightarrow {}^5T_2$ luminescence band into three sub-bands, instead of the two sub-bands observed at ambient pressure ZnSe:Cr. The appearance of the additional "c"-subband with pressure increase can be explained by the pressure induced admixture of ligand wave functions into the central ion wave functions (the nephelauxetic effect) [146]. It is known that even a small admixture of the ligand wave functions may have a significant influence on the spin-orbit parameter [4]. The nephelauxetic effect obviously increases with applied pressure [147] and changes the value of the spin-orbit parameter, which explains the appearance of the additional band in the ${}^5E \rightarrow {}^5T_2$ luminescence spectrum and changes in the intensities of the sub-bands.

6.2.3. The nature of 1.25 eV-centered ZnSe:Cr PL band

In order to identify the origin of ZnSe:Cr emission band, centered at 1.25 eV, it was studied under high pressure within (0÷55) kbar range at liquid-helium temperature. The 1.25 eV band is broader and does not exhibit any splitting, in contrast to the 0.6 eV band. Besides, the 1.25 eV PL peak undergoes a red-shift with pressure increase, as one can see in Fig. 28 and Fig. 29. Thus, the pressure coefficient of this PL band is negative, and its absolute value $[k_2 \approx (-10.6 \pm 0.5) cm^{-1}/kbar]$ turned out to be similar to the pressure coefficients of "a" and "b" subbands of the 0.6 eV band $[k_1^a \approx (7.9 \pm 0.4) cm^{-1}/kbar$ and $k_1^b \approx (8.7 \pm 0.7) cm^{-1}/kbar]$.

The zero-phonon line, observed at around 1.328 eV in the case of bulk "thick" sample didn't reveal itself in the high-pressure measurements as well. As it was mentioned earlier, the

deformations effects, present in the sample, being under high hydrostatic pressure can provoke the extreme broadening of the zero-phonon line, what, in turn, makes it unobservable on the spectra [141]. Besides, very thin samples used in the experiment and, consequently, low intensity of emission limits in the DAC the spectral resolution of the data.

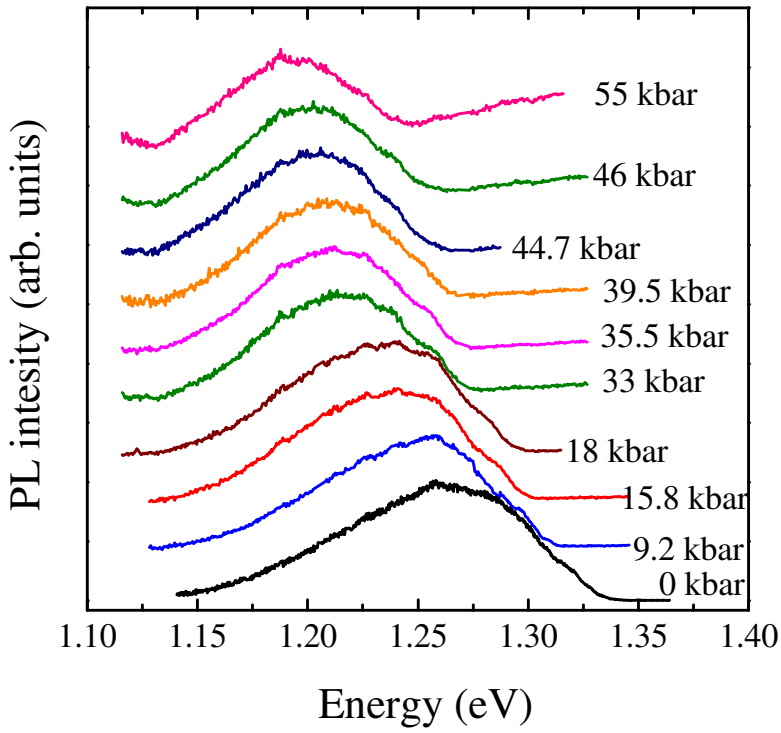

Fig. 28. Pressure dependence of the liquid-helium ZnSe:Cr PL band centered at 1.25 eV.

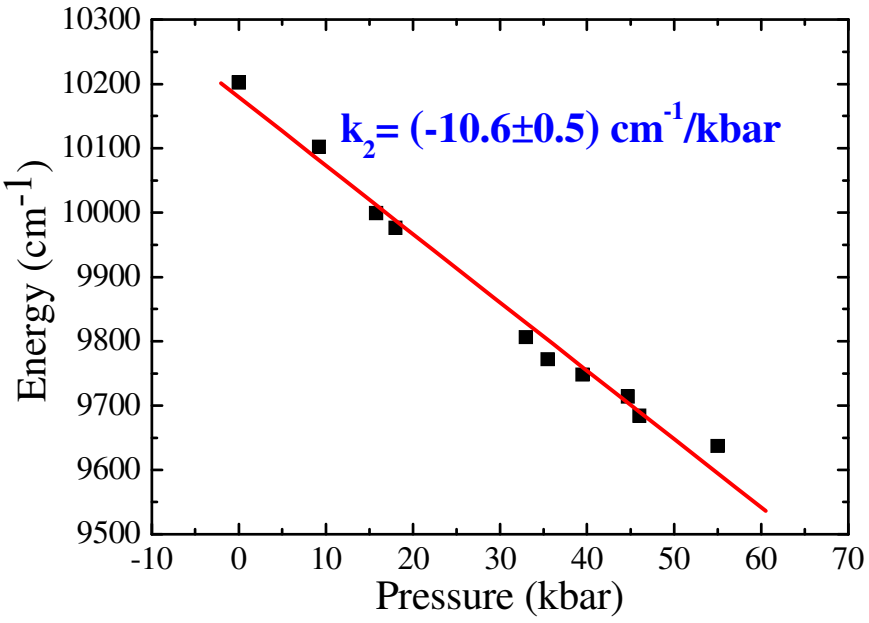

Fig. 29. Pressure dependence of the spectra position of Cr^{2+} PL maxima of the same crystal at liquid-helium temperature.

As it follows from the Tanabe-Sugano diagram, $^3T_1 \rightarrow {}^5T_2$ transition is the most probable candidate for the origin of this band. The $^3T_1$ state is the second excited state of Cr^{2+} ion in tetrahedral CF. The relatively large energy of this transition and the relatively large energetic distance from the first excited ^5E state makes the radiative transitions from this level quite probable.

There are a few $^3T_2$ and $^3T_1$ terms within the d^4 configuration. The two lowest terms shown in Fig. 27 consist mainly (about 90 %) of the t_2e^3 configuration. Therefore, both terms should undergo tetragonal distortion and the transition from these terms to the ground $^5T_2$ level should show splitting. However, in both terms the e^3 electrons are shared in a different manner among the d_v=v and d_u=u orbitals, and this makes the essential difference in their behavior. One can illustrate this in a detail.

The diagonal matrix elements of tetragonal distortion (elongation or contraction along z axis) for the d states are:

$$\left.\begin{aligned} &\langle xz||xz\rangle=\langle yz||yz\rangle=V/7,\\ &\langle xy||xy|\rangle=-2V/7,\\ &\langle u||u\rangle=2V/7,\\ &\langle v||v\rangle=-2V/7. \end{aligned}\right\} \qquad (6.3)$$

Here || denotes the corresponding operator of tetragonal distortion and V is the JT coupling constant. The z components of the wave function in form of the Slater determinant of the term under considerations are [12]:

$$|^3T_{1Z}\rangle=|xy,u,\underline{u},v\rangle \qquad (6.4)$$

and

$$|^3T_{2z}\rangle=|xy,\ u,v,\underline{v}\rangle, \qquad (6.5)$$

where the opposite spin orientation is underlined. The tetragonal distortion for the considered components is:

$$\langle^3T_{1Z}||^3T_{1Z}\rangle=(-2/7+2/7+2/7-2/7)V=0 \qquad (6.6)$$

and

$$\langle^3T_{2Z}||^3T_{2Z}\rangle=(-2/7+2/7-2/7-2/7)V=-4V/7. \qquad (6.7)$$

Therefore, within this approximation the $^3T_1$ term is not JT active while the $^3T_2$ term shows a strong distortion. Since the final term for the luminescence starting from non distorted $^3T_1$ term is also free of distortion we conclude that the 1.25 eV luminescence is the $^3T_1 \rightarrow {}^5T_2$ transition. Certainly, $^3T_1$ consists of around 10% of other electron configurations (6 of total 7)

which produces some residual distortion. However, the $^3T_1 \rightarrow {}^5T_2$ transition is rather strongly crystal field dependent and the expected splitting is hidden in the thermal width of luminescence line.

The two excited terms involved in luminescence show also different breathing distortions. Taking the $^5T_2$ term with the configuration $t_2^2e^2$ as reference equilibrium for the ligand tetrahedron, the term ^5E with the configuration t_2^3e produces enlargement of the tetrahedron while the term $^3T_1$ with configuration t_2e^3 produces its contraction. This means, contrary to the Tanabe-Sugano diagrams, little difference in Dq for both transition lines and additionally, the different portion of the Coulomb repulsion energy in transition. The latter comes from the different degree of covalence (the admixture of the ligand functions to the 3d functions – again the nephelauxetic effect) in each term separated by quite large energy intervals. Thus, the energy difference between ^5E and $^5T_2$ is not pure $10Dq$ energy. This, at least partly, explains some small difference in the absolute values of the pressure coefficients for the 1.25 eV and 0.65 eV lines. Although the luminescence between the $^3T_1$ and $^5T_2$ can be easily detected, the spin-forbidden character of the $^3T_1 \leftrightarrow {}^5T_2$ transitions makes them difficult to be observed in the absorption spectra.

One can speculate that 1.25 eV band is due to the Cr^{1+} charge state. The $Cr^{2+} \rightarrow Cr^{1+}$ photo-transformation process upon illumination of the crystal by the argon ion laser light was reported in ZnSe:Cr crystals in [148]. The possible candidate for this would be the $^4T_1 \rightarrow {}^6A_1$ transition within the d^5 electronic configuration of the Cr^{1+} ion. However, such a transition should be observed at much higher energy, according to the Tanabe-Sugano diagrams for the d^5 configuration (calculated also with the parameters for Cr^{2+}) [149]. Hence, one can assume that both luminescence bands belong to the Cr^{2+} charge state.

6.2.4. High-pressure PL studies of ZnTe:Cr^{2+}

The emission band, corresponding to $^5E \rightarrow {}^5T_2$ transition of ZnTe:Cr^{2+} was studied as a function of hydrostatic stress within (0–102.5) kbar pressure range (Fig. 30). As compared with a similar emission for ZnSe:Cr^{2+}, the fine structure consisting of three peaks (marked on the graph) is clearly resolved. The pressure dependence of maxima positions for the corresponding lines is plotted in Fig. 31. The shift of the lines in average as whole is due to increase of the strength of the cubic crystal field $\Delta = 10Dq$. The energy separation between

the lines is increased as well. Further this splitting will be interpreted as the combined action of the JT instability in the excited ^5E term and both JT and spin-orbit splitting in the ground $^5T_2$ term. As compared with ZnSe:Cr^{2+} the average shift is 20-25 % larger. This is related to the lower value of the bulk modulus B_0 = 510 kbar for ZnTe as compared with the value of B_0=624 kbar for ZnSe crystals [144,145].

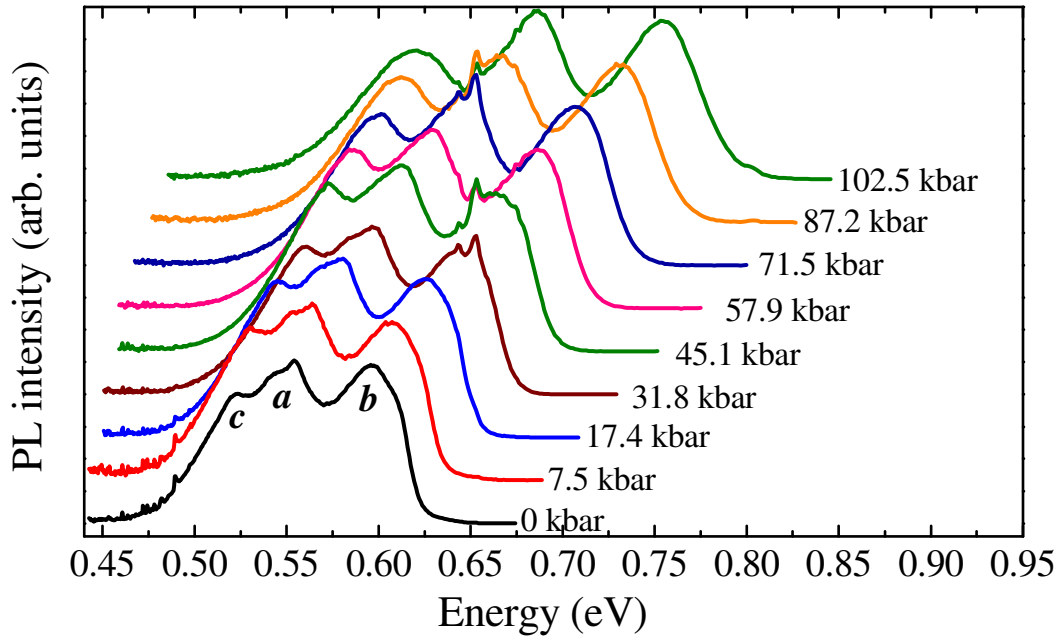

Fig. 30. The luminescence spectra of the ZnTe:Cr^{2+} crystal as a function of hydrostatic pressure at T=10 K, excited by the 514 nm argon-ion laser line.

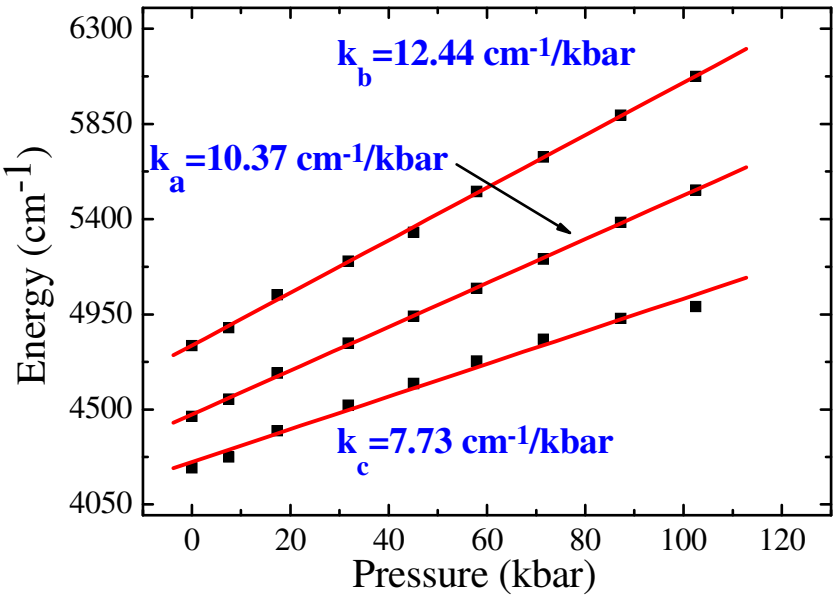

Fig. 31. Pressure dependencies of the spectral position of the Cr^{2+} emission maxima of the ZnTe:Cr crystal at T=10 K.

6.2.4.1. Discussion: $^5E \leftrightarrow {}^5T_2$ emission and absorption [150]

The ligands surrounding Cr^{2+} ions in II-VI compounds are tetragonally distorted along one of cubic axes. Since none of the axes is statistically preferred we consider in detail the distortion along z axis only. The description of tetragonal distortion caused by JT coupling differs from that given by the classical tetragonal crystal field. Both descriptions are used to interpret the optical spectra. However, there is only a limited compatibility between the parameters derived within the framework of both descriptions. This point will be discussed by making the parallel considerations.

The ground $^5T_2$ term is strongly coupled to e type JT distortion (the T-e problem). The matrix of distortion energy along only z axis is given as [55]:

$$E(T) = V_T \begin{pmatrix} 1/2 & 0 & 0 \\ 0 & 1/2 & 0 \\ 0 & 0 & -1 \end{pmatrix} Q_{3z^2-r^2} \tag{6.8}$$

In the point-charge approximation of ligands, the value of V_T is equal to:

$$V_T = Z\frac{8\sqrt{2}}{7}\left[\frac{\langle r^2\rangle}{R_0^4} + \frac{20}{27}\frac{\langle r^4\rangle}{R_0^6}\right], \tag{6.9}$$

where Z is a ligand charge. To explain consistently the previous absorption/emission and EPR studies with these high pressure emission studies we draw one-electron levels and many-electron terms with account for the JT instability and spin-orbit (SO) coupling. Fig. 32 presents occupation of one-electron levels appropriate for the $^5T_2$ term.

In this figure the JT splitting is shown assuming a positive sign of the corresponding JT coupling constants V_T. The slope of t_2 d levels is proportional to the coefficients entering the matrix (6.8) and the scaling due to V_T are omitted. The e levels change according to the matrix for ^5E term as given below. The occupation on the left side of Fig. 32 originates in the energy gain of $E_{JT} = V_T^2/k$, where k is the elastic force constant. The occupation on the right side gives energy gain $E_{JT}/4$ and does not correspond to real physical situation. The splitting of the $^5T_2$ term corresponding to occupation in Fig. 32 is shown in Fig. 34 and it is caused by the compression along z axis. If one assumes a negative V_T, then it is necessary only to change the direction of axis of distortion $Q_{3z^2-r^2}$.

The tetragonal crystal field splitting of $^5T_2$ is given as [151]:

$$E(^5E) = Bs - 4Ft, \tag{6.10}$$

$$E(^5B_2) = -2Bs + Ft, \tag{6.11}$$

where B and F are numerical coefficients and $s = \frac{2\langle r^2 \rangle}{7}$, $t = \frac{8\langle r^4 \rangle}{21}$. These energies can be partly derived from the JT coupling matrix. Looking at the formula for V_T one can recognize that the first term in brackets, when multiplied by $Q_{3z^2-r^2}$, can be associated with Bs, while the second one – with Ft. The analogy is not full because Ft enters expressions (6.11) and (6.12) with opposite sign and different coefficients. The point is that we consider the JT coupling linear in displacements $Q_{3z^2-r^2}$. There is also a term quadratic in the displacement, which produces in the lowest order the contribution proportional to $\langle r^4 \rangle$, which gives additional contribution to Ft. Equivalently this quadratic term can be considered as a correction to the elastic energy term. The expression of type (6.11) and (6.12) are usually derived by Stevens method of equivalent operators [55] and is totally based on the proper account of defect symmetry.

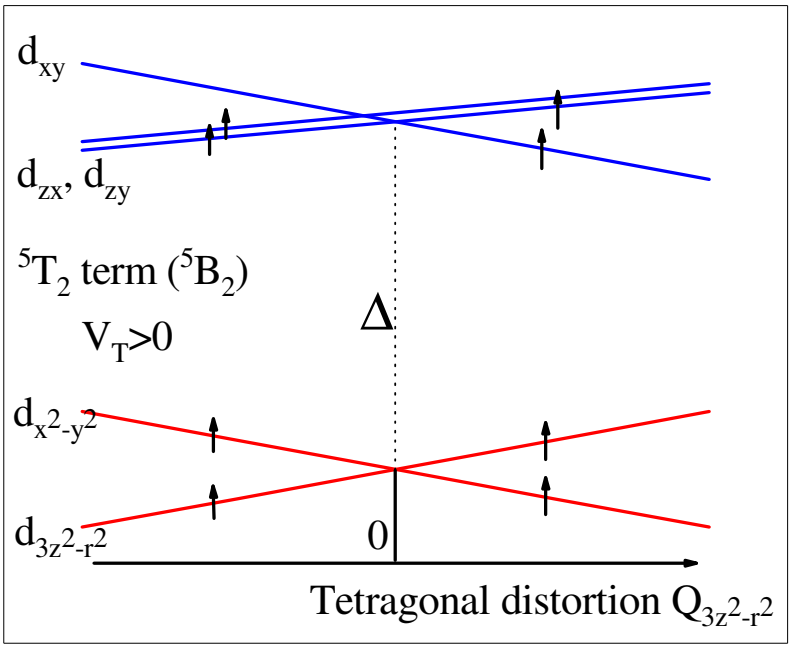

Fig. 32. The occupation of one-electron *d* orbitals appropriate for the ground $^5T_2$ term. The JT splitting (without inclusion of the elastic energy) under tetragonal distortion $Q_{3z^2-r^2}$ is shown. Having provided $V_T > 0$, the energy minimum corresponds to contraction along the *z*-axis.

In case of the ^5E term there is also a coupling to tetragonal distortion (the *E-e* problem). The coupling energy matrix is the following:

$$E(E) = V_E \begin{pmatrix} 1 & 0 \\ 0 & -1 \end{pmatrix} Q_{3z^2-r^2} \qquad (6.12)$$

The JT coupling constant for this term is equal to:

$$V_E = Z\frac{8\sqrt{2}}{7}\left[\frac{\langle r^2\rangle}{R_0^4} - \frac{5}{9}\frac{\langle r^4\rangle}{R_0^6}\right], \tag{6.13}$$

The σ_z Pauli matrix is the coupling energy matrix and apart from the sign differs from that in the custom description of *E-e* problem [56], which does not coincidence with the convention of the classical tetragonal distortion of the crystal field. The first term in brackets in the expression for V_T and V_E is the same while the second enters with the opposite sign. From this follows that $|V_E| < |V_T|$. One electron occupation for the ^5E term is shown in Fig. 33 and the corresponding terms are shown in Fig. 34.

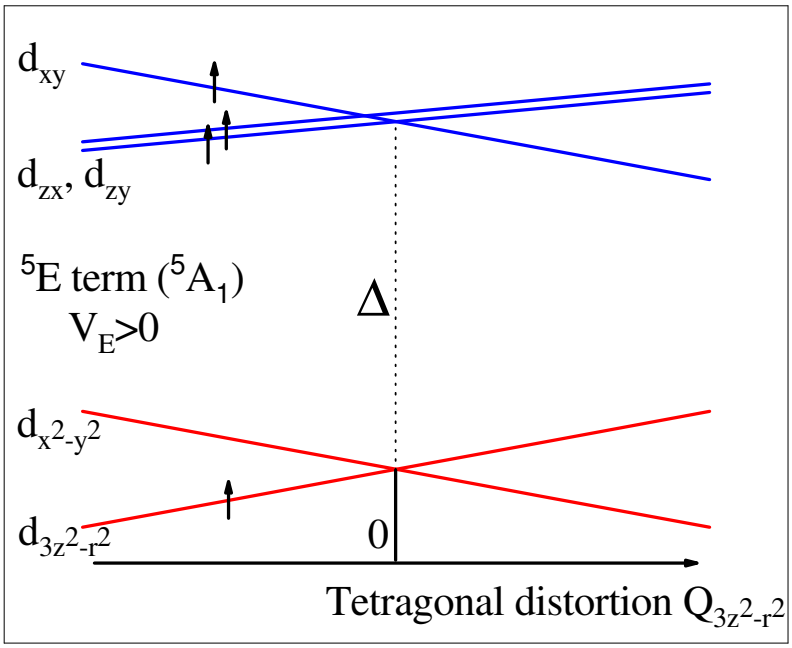

Fig. 33. The occupation of one-electron *d* orbitals appropriate for the excited ^{5}E term. The JT splitting (without inclusion of the elastic energy) under tetragonal distortion $Q_{3z^2-r^2}$ is shown. Having provided $V_E > 0$, the energy minimum corresponds to elongation along the *z*-axis.

When $^5T_2 \rightarrow {}^5E$ transitions take place the ^5E term splitting is governed by V_E but they take place at distortion coordinate $Q_{3z^2-r^2} = -V_T/k$. Therefore the resulting splitting of ^5E term (it is not at its equilibrium distortion) is proportional to V_E V_T. Using the expression for the JT energy in the ground ($E_{JT}=V_T^2/k$) and in the excited term ($E_{JT}=V_E^2/k$) one can make replacements:

$$V_E V_T = E_{JT}(av)2k = \sqrt{E_{JT}(V_T)E_{JT}(E)}\,2k\,. \tag{6.14}$$

The separation between terms $^5A_1$ and $^5B_1$ is equal to $4E_{JT}(av)$. The tetragonal crystal field splitting of ^5E term is given as [151]:

$$E(^5A_1) = 2Bs + 64Ft, \tag{6.15}$$

$$E(^5B_1) = -2Bs + Ft. \tag{6.16}$$

Again, Bs term can be associated with the first term in brackets in the expression (6.13) for V_E, while the second term is associated with Ft. The tetragonal crystal field expression also contains the contribution from the quadratic JT coupling (this coupling is responsible for the warping of the "Mexican Hat" surface in the E-e problem). After absorption process the electron configuration changes from $t_2^2e^2$ to t_2^3e and the new equilibrium is searched. The ^5E term has two equilibrium distortions (see Fig. 34), but since

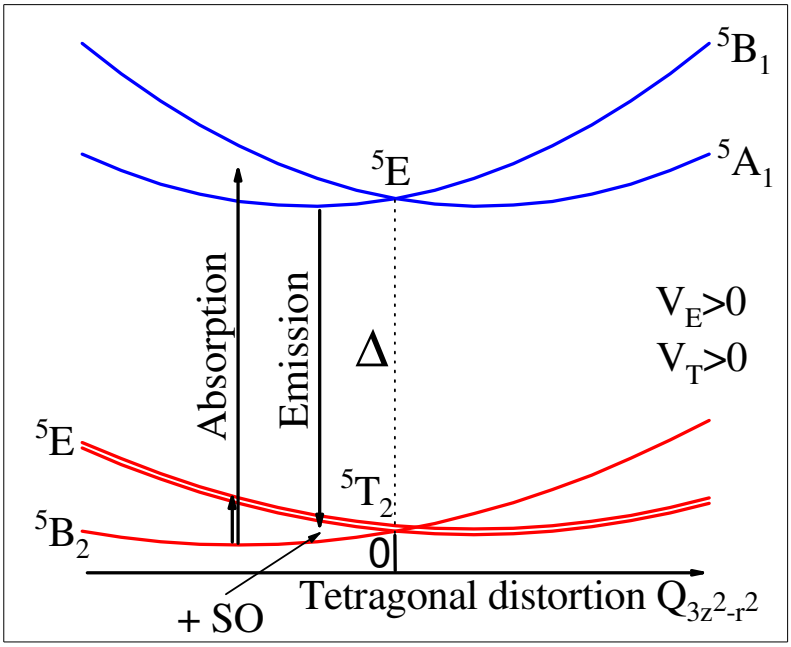

Fig. 34. The configuration diagram of absorption/emission transitions between the $^5T_2 \leftrightarrow {}^5E$ terms. The JT splitting (with inclusion of the elastic energy) under tetragonal distortion $Q_{3z^2-r^2}$ is shown. The energy minima in the ground and excited terms correspond to contraction or expansion along z-axis. The end states of emission are split due to combined action of JT and spin-orbit coupling (not shown here).

the previous equilibrium corresponds to the compression, the smallest elastic energy change will correspond to equilibrium coordinate $Q_{3z^2-r^2} = -V_E/k$. The separation between the ^5E and $^5B_2$ terms at the equilibrium coordinate $Q_{3z^2-r^2} = -V_E/k$ is equal to $3E_{JT}(av)$. After the emission a process of relaxation of ligands occurs to coordinate $Q_{3z^2-r^2} = -V_T/k$. The principal difference between the treatment of tetragonal distortion in terms of the classical crystal field theory and the J-T distortion is the following. The classical crystal field model

assumes that equilibrium distortion in all terms is the same as in the ground one (this is the basic assumption of the Tanabe-Sugano diagrams) [56]. In other words the distortion does not depend on the electron sharing among the t_2e electron orbitals. Since the absorption spectra are rather broad (also due to the thermal motion) it is possible only to determine the rough value of *Bs*. The JT description of distortion takes into account the dependence of equilibrium distortion on the particular electron configuration. However, the formulas for V_T and V_E based on the point charge model are not enough precise for numerical estimation. The JT description correctly distinguishes the absorption/emission of electrons among t_2e orbitals and associates it with the adjacent lattice relaxation. However, it is possible to conclude that V_T and V_E have the same sign and that $|V_E| < |V_T|$. The energies of many electron terms and assumed transitions in Cr^{2+} ion are shown. Now, we will explain the possible physical situation of the particular experiments. This will remove some seeming controversies between various observations.

In the equilibrium configuration of the $^5T_2$ term the JT coupling is so strong that the spin-orbit coupling within this term is quenched [55]. The exponent in Ham quenching factor $\gamma=\exp(-3E_{JT}/2\hbar\omega)$ can be even around –10, so that off-diagonal matrix elements of spin-orbit coupling are negligible. Here $\hbar\omega$ is the value of effective energy of the tetragonal vibrational mode. For this reason the *g* factor for the orbitally nondegenerate term is nearly isotropic across ZnS, ZnSe, ZnTe, and CdTe crystals. The $^5B_2 \rightarrow {}^5E$ absorption is a broad band without structure. It is centered on $3E_{JT} \approx 1000$ cm^{-1} across II-VI compounds [4]. Similarly the higher energy absorption $^5B_2 \rightarrow {}^5B_1$ and $^5B_2 \rightarrow {}^5A_1$ is a single broad band centered on Δ. The absorption to excited term is determined by the ligand distortion of the initial term. Since the amplitude of ligand distortion in the excited term ^5E is different, i.e. $V_T \neq V_E$, the ligands change their position so as to adjust to the equilibrium position for new electronic configuration $e^1t_2^3$ in the ^5E term. We note that due to the $e^2t_2^2 \rightarrow e^1t_2^3$ electronic configuration change both the tetragonal distortion and also the breathing type distortion change. Then the emission transitions proceed from the lowest level determined by ligand deformation corresponding to the excited term. Now the splitting of $^5T_2$ is governed by the V_T but at equilibrium coordinate $Q_{3z^2-r^2} = -V_E / k$. Since the amplitude of V_E is much smaller than V_T and the equilibrium distortion for the lowest and excited terms are far away, the action of factor γ in the nonequilibrium $^5T_2$ term is ineffective. As a result the emission line characterizes the combined action of JT distortion with the $3E_{JT}(av)$ energy and the spin-orbit interaction. The splitting of the $^5T_2$ term under mentioned condition is shown in Fig. 34 at zero pressure.

From this follows that ${}^5T_2 \leftrightarrow {}^5E$ absorption/emission transitions carry totally different information because the details of the initial and final states are not the same ones. Immediately after the emission the ${}^5T_2$ level relaxes (by means of ligands displacement) to its new equilibrium position.

6.2.4.2. Effect of hydrostatic pressure

In principle, the hydrostatic pressure is equivalent to the displacement of ligands in the breathing mode fashion towards the central Cr^{2+} ion. At ambient condition the breathing mode coupling constant (analogue of JT coupling constants) is $V_A = 0$. This is a condition of equilibrium interatomic distance R_0. Application of pressure makes $V_A \neq 0$ and produces resistance against applied stress. In the point charge model the strength of the cubic field is inversely proportional to the fifth power of interatomic distance:

$$\Delta \propto \frac{1}{R^5}, \tag{6.17}$$

hence, the application of pressure increases Δ, i.e. the average energy distance between ${}^5E$ and ${}^5T_2$ terms increases. As concerns the tetragonal distortion the breathing and tetragonal mode transform according to different irreducible representations and there is no interference between them. However, the tetragonal mode coupling constants V_E or V_T are estimated at pure cubic crystal field distance R_0 which is changed by applied pressure. As a result, the tetragonal coupling mode constants V_E or V_T, described by equations (6.9) and (6.13), increase in the point charge model approximation proportionally to $\frac{1}{R^4} - \frac{1}{R^6}$. Thus, similarly to Δ, the hydrostatic pressure effectively increases the tetragonal distortion. Since the JT distortion energy is proportional to V^2, it means that the average change of $E_{JT} \propto \frac{1}{R^{10}}$ (provided that the force constant k changes negligibly).

According to the point ion approximation, the cubic crystal field parameter Δ and the tetragonal field parameter $D=3E_{JT}$ change with the pressure as

$$\Delta = \Delta_0 \left(\frac{R_0}{R} \right)^5 , \tag{6.18}$$

$$D = 3E_{JT} = D_0\left(\frac{R_0}{R}\right)^{10} \tag{6.19}$$

where (R_0/R) changes with pressure p according to Murnaghan equation of state (6.2) [143].

While solving the secular equation for the JT interaction and spin-orbit interaction in the $|L,M,S,M_S>$ basis, we use an approximation where the diagonal matrix elements for $^5T_2$ and ^5E states change with pressure as

$$\varepsilon_1(^5T_2) \propto \Delta_0\left(\frac{R_0}{R}\right)^5 + E_{JT}\left(\frac{R_0}{R}\right)^{10} \tag{6.20}$$

and

$$\varepsilon_2(^5E) \propto \Delta_0\left(\frac{R_0}{R}\right)^5 - 2E_{JT}\left(\frac{R_0}{R}\right)^{10}, \tag{6.21}$$

respectively. One should note, that these relations are only approximately valid because only linear JT coupling has been considered. Additionally to the pressure dependence of the diagonal matrix elements, there was included into calculation the following approximate dependence on pressure of spin-orbit constant:

$$\lambda = \lambda_0\left(\frac{R_0}{R}\right)^4, \tag{6.22}$$

where λ corresponds to λ_1 in the notation of J.T.Valin et al. [5]. This approximation can be very roughly justified by the covalent effects which remarkably change λ of Cr^{2+}. This change is due to admixture of ligands electronic functions to d function, so the effective function of d electrons is not limited to the volume occupied by Cr^{2+} ion. The interaction matrix elements of $3d$ electrons with ligands can change as $\left(\frac{R_0}{R}\right)^{\frac{7}{2}}$ [152]. This mainly contributes to the variation of λ with the pressure. If the effective spin-orbit coupling constant is averaged over such extended function then there are contribution from atomic spin-orbit constant of ligands. From atomic calculations it is known that single electron spin-orbit coupling constant of Te is more than 10 times larger than that for Cr^{2+} ion [153]. Also the spin-orbit coupling constant of Te is much larger than those of S and Se [153]. Therefore, the modification of amplitude of spin-orbit interaction is not surprising and explains the much stronger pressure effect on Cr^{2+} ion in ZnTe in comparison with previously studied Cr^{2+}–doped ZnSe and ZnS, what was shown in the 6.2.1 and 6.2.2 Sections of the present Thesis. The second order of perturbation theory of SO coupling between the $^5T_2$–^5E terms was included, what gives a contribution proportional to λ^2/Δ. J.T. Vallin suggests [5] that the spin-

orbit constant (in his notation λ_2) between these terms is negative. However, it does not make problem in calculation because the corresponding correction is proportional to λ^2. The results of such calculations are shown in Fig. 35.

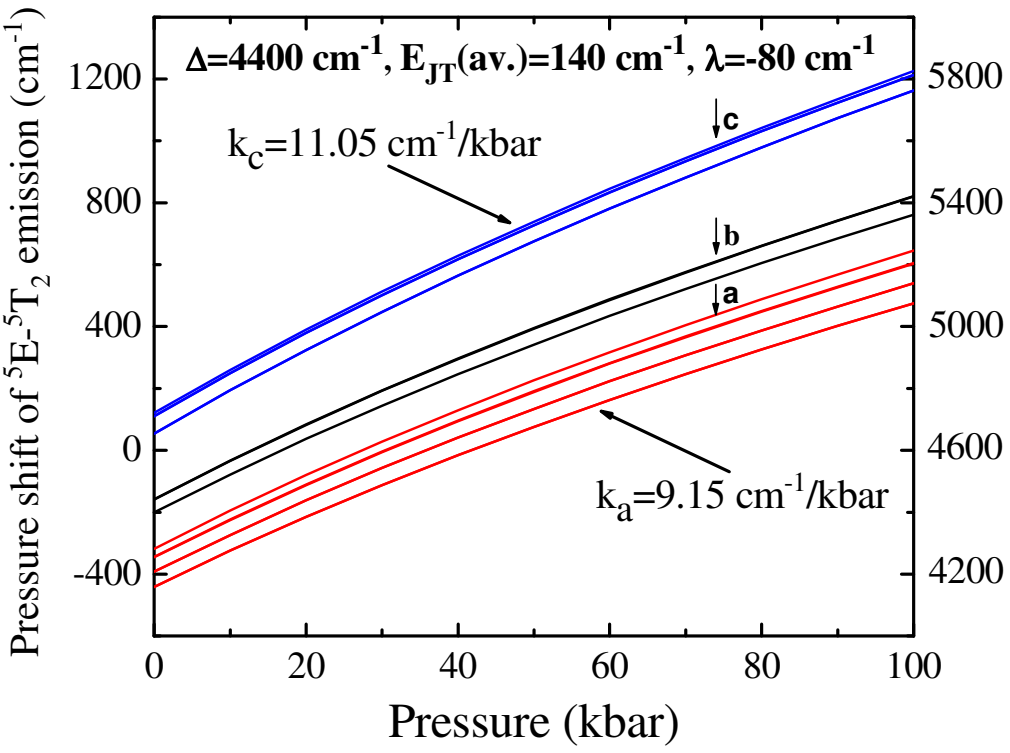

Fig. 35. Theoretical calculation of the pressure dependence of $^5E \rightarrow {}^5T_2$ transition in ZnTe:Cr (left scale). Zero energy at ambient pressure (left scale) corresponds to Δ= 4600 cm^{-1}. The right scale is given in absolute values. The values of the parameters used in the calculations are given in the graph.

Qualitatively, the pressure dependence of calculated emission shows the main feature observed in the experiment, shown in Fig. 30, and Fig. 31. The splitting into three bands having different pressure coefficients is well reproduced. However, the calculated pressure coefficients differ slightly from those observed in the experiment. In view of the provided discussion one cannot say firmly, that the used parameters λ and $E_{JT}(av)$ (extracted from those determined in literature $E_{JT}(T)$ and $E_{JT}(E)$ are the most suitable. Perhaps, one needs to use more parameters but, as we already mentioned, the methods of their determination are not very sensitive to the features of the experimental spectra.

In the above adduced interpretations the theoretical model developed by doc. dr hab. S.W.Biernacki was used.

6.3. Conclusions I.

1. Low-temperature PL spectra of ZnS:Cr sample is characterized by a broad two-band shape. A spin-orbit interaction in ZnS:Cr was found to be so weak, that it didn't reveal itself significantly on the PL spectra neither at ambient nor at high hydrostatic pressure.

2. Ambient pressure ZnSe:Cr spectra reveals two-band shape due to $^5E \rightarrow {}^5T_2$ transition and JT distortion as well. The increased admixture of the ligand wave functions into the central ion wave functions with applied pressure has been found responsible for the changes in the value of the spin-orbit parameter and appearance of the additional band in the $^5E \rightarrow {}^5T_2$ luminescence spectra of ZnSe:Cr at higher pressures.

3. High-pressure luminescence measurements at low temperature unambiguously indicate that the 1.25 eV luminescence band in ZnSe:Cr is associated with the intrashell $^3T_1 \rightarrow {}^5T_2$ transitions of the Cr^{2+} ion.

4. The stress effect on luminescence spectra of Cr^{2+} in ZnTe exhibits a strong difference in comparison with ZnS:Cr^{2+} and ZnSe:Cr^{2+}. Observed ZnTe:Cr^{2+} pressure coefficients of emission peaks associated with $^5E \rightarrow {}^5T_2$ transitions differ from each other, what has not been observed in the case of Cr^{2+}-doped ZnSe and ZnS crystals. This effect can be explained by the pressure dependent modification of the spin-orbit interaction constant associated with the admixture of *Te* ligand wave function to the wave function of the central Cr^{2+} ion. Much smaller spin-orbit constant for *S* and *Se* ligands does not produce such an effect, what is in a total compliance with (2.40) relation.

6.4. Ambient-pressure studies of the InP-based multi quantum structures

6.4.1. Preliminary PL studies

Preliminary PL spectra of the InP-based quantum structures were taken at ambient pressure, at T=10 K in the Oxford 1204 cryostat equipped with a temperature controller for low temperature measurements. The measurements were performed using DIGIKROM 240 monochromator equipped with a Judson J13TE2 thermoelectrically cooled PbS detector and a SR 530 model Standford Research lock-in amplifier. The spectra were excited with the 514.5 nm line of argon-ion laser.

All the samples are characterized with intense exciton emission. Rather sharp photoluminescence lines are centered at 0.887, 1.023 and 1.177 eV for $InAs_xP_{1-x}$/InGaP, $InAs_xP_{1-x}$/InGaAsP and $InAs_xP_{1-x}$/InP structure respectively (Fig. 36)). The full-width at half-minimum (FWHM) of all the bands do not exceed 7.5 meV, what is lower than half-widths of InAsP QWs reported in the literature [154-156]. Inasmuch as at low temperatures the PL linewidth is manly due to interface roughness, alloy disorder and well width fluctuations, low FWHM value can argue about the high quality epitaxy of the grown quantum structures. The intense emission of the samples forebodes their significant PL signal at high stress conditions as well, what makes them appropriate candidates for high-pressure DAC sensors.

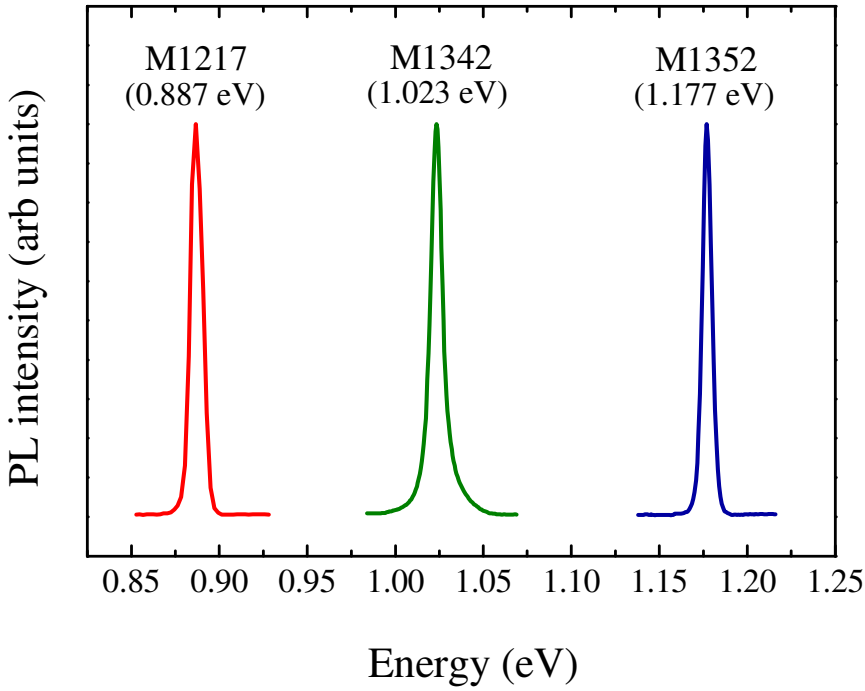

Fig. 36. Ambient-pressure PL spectra of the InP-based MQWs taken at T=10 K.

6.4.2. The composition of the MQWs

The composition of the studied MQWs can be determined experimentally on the basis of ambient-pressure PL measurements.

It is known, that quantum confinement effects are important, when for the width b of the structure the following criterion is fulfilled [157]:

$$b \leq \sqrt{\frac{\hbar^2}{m^* k_B T}}, \tag{6.23}$$

where m^* is the effective mass of the electron, k_B and T are Boltzmann constant and temperature, respectively [158]. While substituting into (6.23) the effective mass of InAsP ($m^* \approx 0.07 m_0$ [159]), one can obtain the temperature dependence of the maximum InAsP layer widths b, for which the quantum effects are essential (Fig. 37).

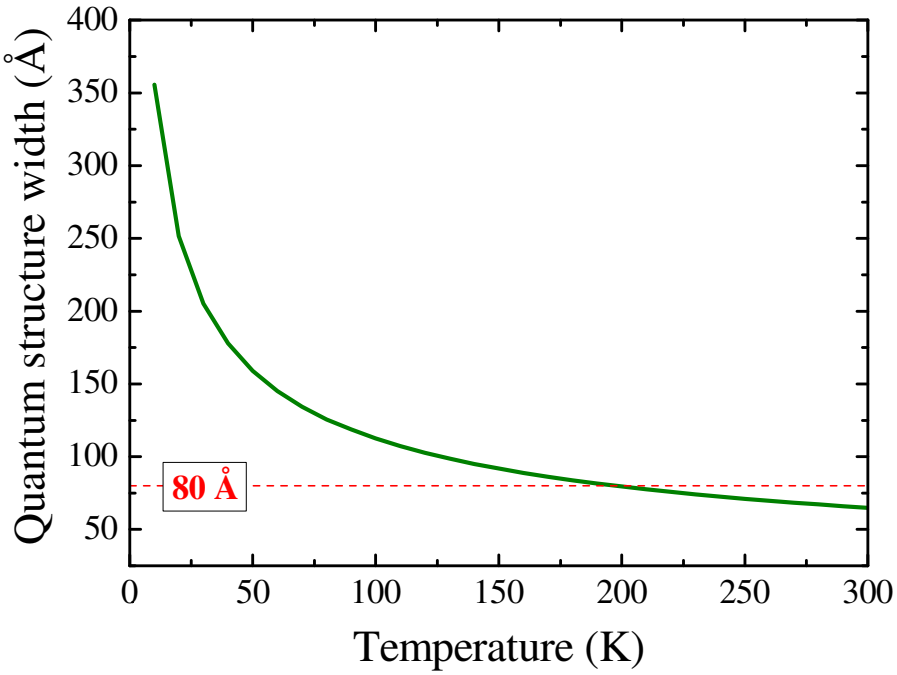

Fig. 37. Temperature dependence of the quantum structure width b, for which the quantum effects are essential, calculated for InAsP.

As the width of the studied QWs is 80 Å (Tables 6-8), one can conclude, that for $T \geq 200K$ the quantum effect in the examined InAsP layers should be negligible.

For the rough estimation of the InAs mole fraction in the $InAs_xP_{1-x}$ MQWs one can use the liniar approximation of the energy gap E_g dependence on content x (the extension of Vegards' law) [160,161]:

$$x = \frac{E_g(InP) - E_{PL\ peak}^{QW}(InAsP)}{E_g(InP) - E_g(InAs)}. \quad (6.24)$$

While taking into account, that at T=0 K $E_g(InP)$ = 1.42 eV and $E_g(InAs)$ = 0.43 eV [162], the following approximate values of InAs mole fraction can be obtained: x=0.54, 0.4 and 0.25 for InAsP/InGaP (M1217), InAsP/InGaAsP (M1342) and InAsP/InP (M1352) quantum wells respectively (Table 9). However, in the studied MQWs the bound states of electrons are localized above the bottom of the conduction band, whereas those of holes are located under the top of the valence band. In such a way $E_{PL\ peak}^{QW}(InAsP) > E_g(InAsP)$, what reduces the numenator in the expression (6.24). Thus, one should note that the values of InAs mole fraction (x), obtained via the described above method are somewhat understated.

The compositional bandgap dependence for ternary InAsP alloys at T=77 K was proposed by G.A. Anytpas and T.O. Yep [163]. Having been improved by M. Wada et al. [164], this dependence is expressed by the following formula:

$$E_g = 1.407 - 1.703x + 0.089x^2 \quad (6.25)$$

The approximate E_g values at T=77 K can be obtained from the fitting curve of the PL temperature dependences, which are described in detail in the following 6.4.3 Section. Thus, these values are 0.881 eV, 1.015 eV and 1.17 eV for the InAsP/InGaP (M1217), InAsP/InGaAsP (M1342) and InAsP/InP (M1352) samples respectively, and the proper mole fractions x of InAs in the $InAs_xP_{1-x}$ QWs were found to be 0.51, 0.38 and 0.23. These results are in a good correlation with the alloy compositions, determined from the Vegard's low extension (Table 9), and most likely can be considered as more accurate.

Table 9. The composition of $InAs_xP_{1-x}$ MQWs determined by two different methods

Sample No.:	.Sample structure:	InAs mole fraction (x) in the MBE process	PL peak at T=10 K, eV	InAs mole fraction (x) determined from the Vegard's law extension	PL peak at T=77 K, eV	InAs mole fraction (x) determined from the empirical equation (6.25)
M1217	$InAs_xP_{1-x}$/InGaP	0.6	0.887	0.54	0.882	0.51
M1342	$InAs_xP_{1-x}$/InGaAs	(?)	1.023	0.40	1.015	0.38
M1352	$InAs_xP_{1-x}$/InP	(?)	1.177	0.25	1.17	0.23

6.4.3. Temperature dependences of the PL spectra

Ambient pressure temperature dependences were studied in the range (10–165) K, (10–105) K and (10–300) K dependently for the M1217, M1342 and M1352 samples respectively. The superior limits of the temperature ranges were determined by the decrease of the PL signal intensity with the temperature increase. The obtained PL spectra and the corresponding PL peak positions versus temperature are shown in Fig. 38-43.

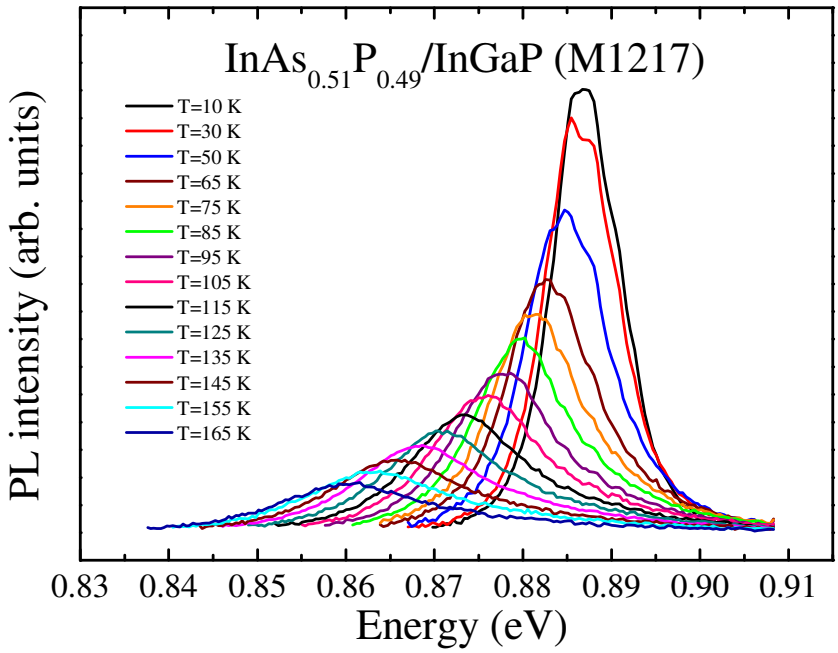

Fig. 38. PL spectra of $InAs_{0.51}P_{0.49}$/InGaP (M1217) sample, taken at T=(10–165) K.

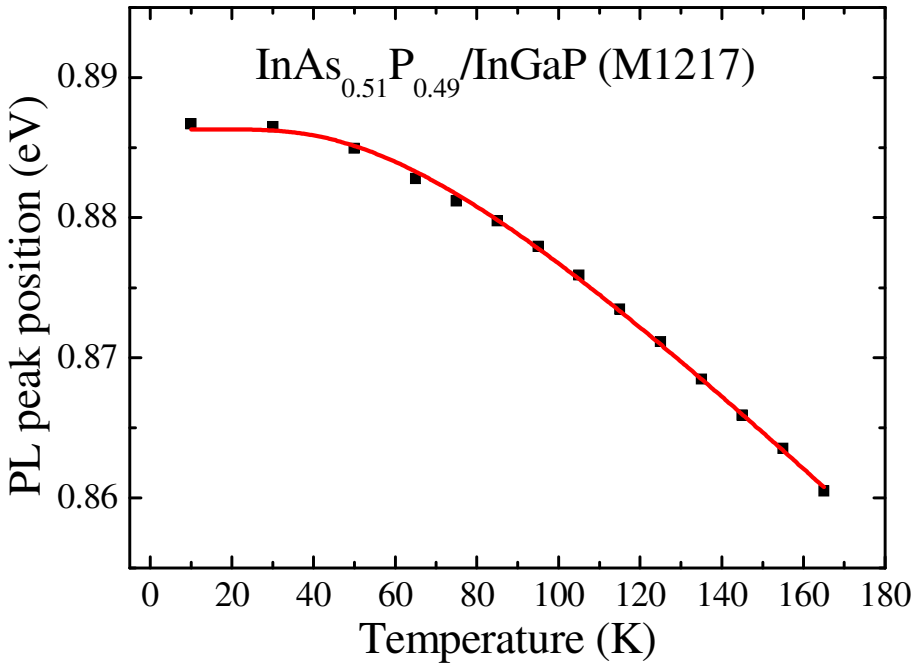

Fig. 39. Variation of PL band position of $InAs_{0.51}P_{0.49}$/InGaP (M1217) sample with temperature change.

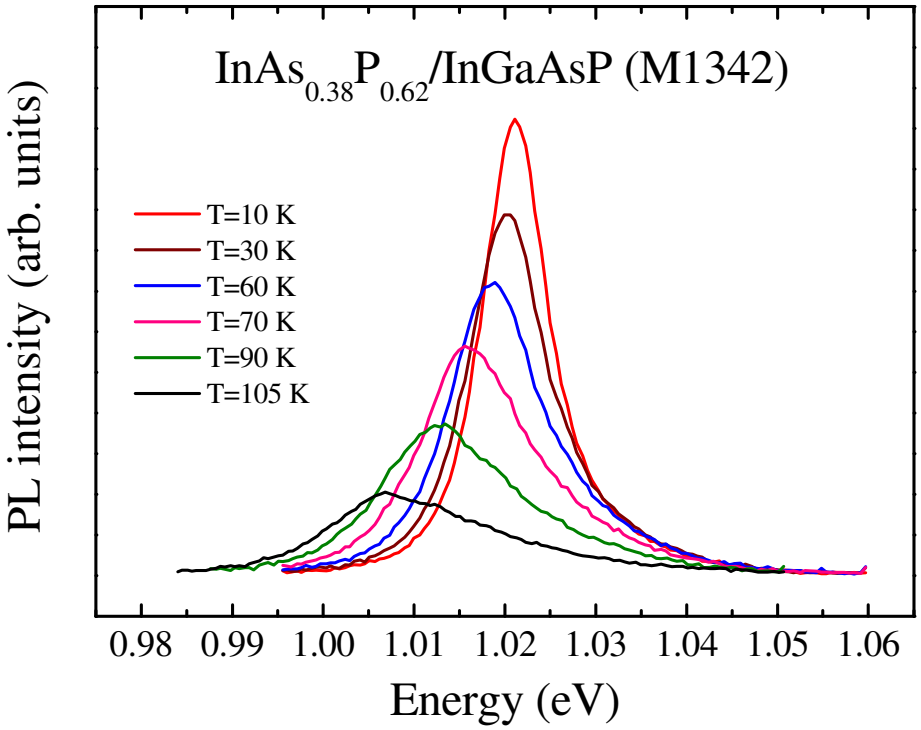

Fig. 40. PL spectra of $InAs_{0.38}P_{0.62}$/InGaAsP (M1217) sample, taken at T=(10−105) K.

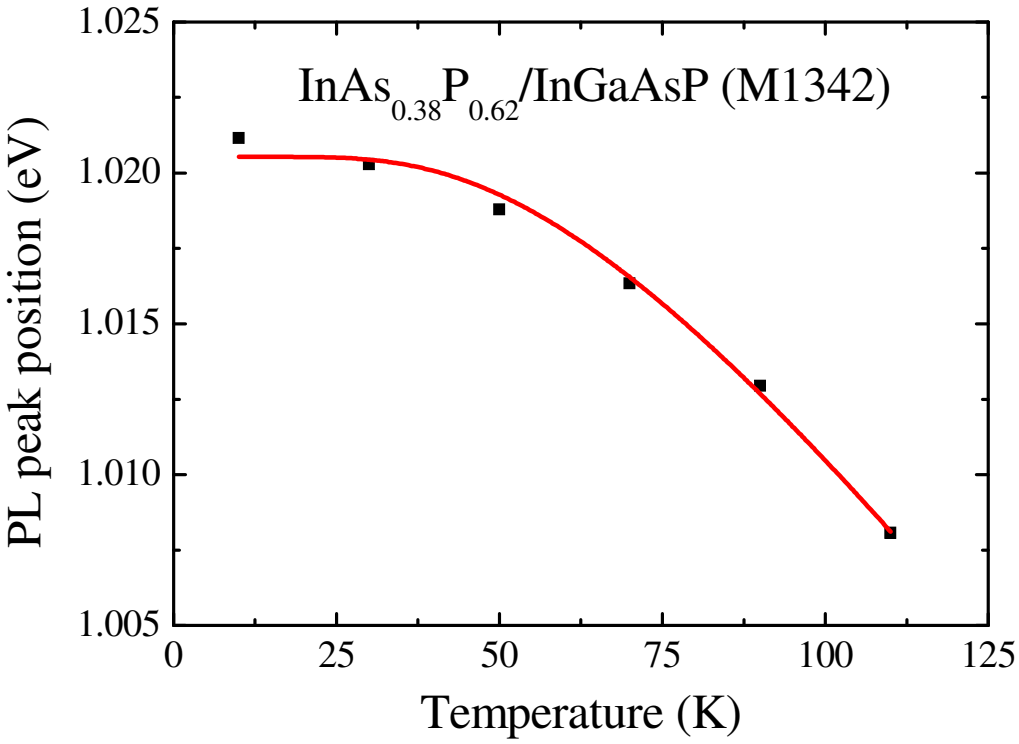

Fig. 41. Variation of PL band position of $InAs_{0.38}P_{0.62}$/InGaAsP (M1342) sample with temperature change.

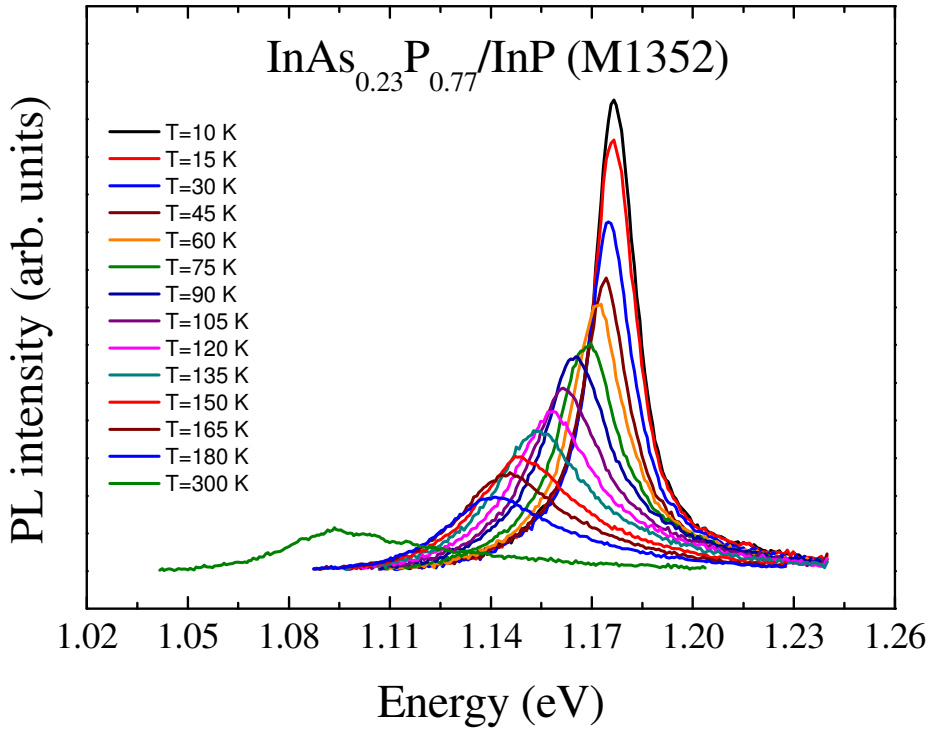

Fig. 42. PL spectra of $InAs_{0.23}P_{0.77}$/InP (M1352) sample, taken at T=(10–300) K.

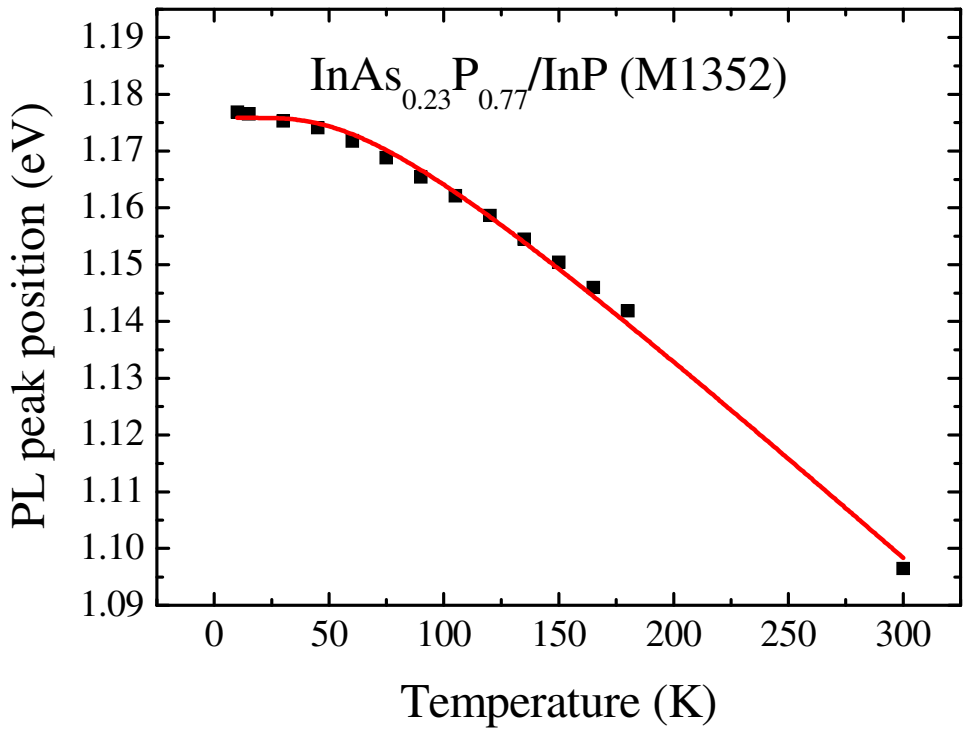

Fig. 43. Variation of PL band position of $InAs_{0.23}P_{0.77}$/InGaAsP (M1352) sample with temperature changes.

The excitation power of the argon-ion laser line was constant and equal to about 90 mW (λ_{exc}=514.5 nm). One can see that at higher temperatures the PL intensity decreases significantly and undergoes a red-shift (Fig. 39, 41, 43). Such temperature dependence of semiconductor bandgap is prevalently described by Varshni relation [165]:

$$E_g(T) = E_0 - \frac{\alpha T^2}{(T+\beta)}, \tag{6.26}$$

where α and β are fitting parameters, being characteristic of a given material. This expression is widely quoted in the literature [166-168], though it does not have a strong theoretical basis, and possesses some disadvantages. Thus, β parameter, which is supposed to be related to the Debye temperature in some cases may be negative [165]. Moreover, at low temperatures the equation (6.26) predicts a quadratic temperature dependence of E_g, whereas the experimental data reveal that E_g is almost independent on T, what can be seen in Fig. 39, 41, 43.

K.P.O'Donnel and X.Chen have proposed another expression for the temperature dependences of semiconductor band gaps, which improves upon the Varshi equation numerically and theoretically [169]. First, it gives better fits to the data (particulary at low temperatures), and, second, the parameters of the fits may be related to an intrinsic interaction of semiconductors, namely the electron-phonon coupling. This equation can be written as follows:

$$E_g(T) = E_g(0) - S\langle\hbar\omega\rangle\left[\coth\left(\langle\hbar\omega\rangle / 2kT\right) - 1\right], \tag{6.27}$$

where $E_g(0)$ is the band gap at zero temperature, S is a dimensionless coupling constant, $\langle\hbar\omega\rangle$ is an average phonon energy and k is a Boltzmann constant.

In Fig. 39, 41, 43 red curves represent the fits, performed with the use of (6.27) equation. The best values of fitting parameters E_g, S and $\langle\hbar\omega\rangle$ are listed in the Table 10.

Table 10. Parameters, showed the best fit for temperature dependence of $InAs_xP_{1-x}$ MQWs

Sample No.	Sample structure	Temperature range, K	$E_g(0)$, eV	S	$\langle\hbar\omega\rangle$, meV
M1217	$InAs_{0.51}P_{0.49}$/InGaP	10–165	0.886	1.72	16.8
M1342	$InAs_{0.38}P_{0.62}$/InGaAs	10–105	1.021	1.8	18.8
M1352	$InAs_{0.23}P_{0.77}$/InP	10–300	1.176	2.04	17.3

One can see, that $E_g(0)$ fit value correlates very well with the energy position of PL peak at T=10 K, obtained experimentally (Table 9). Moreover, S and $\langle \hbar\omega \rangle$ parameters are in a good agreement with those, obtained by M. Wada et al. [164] for $InAs_xP_{1-x}$ samples.

Fig. 38, 40 and 42 give an indication that PL signals of all three samples become broader with temperature. This tendency can be clearly observed on the PL FWHM temperature dependences, presented in Fig. 44–46.

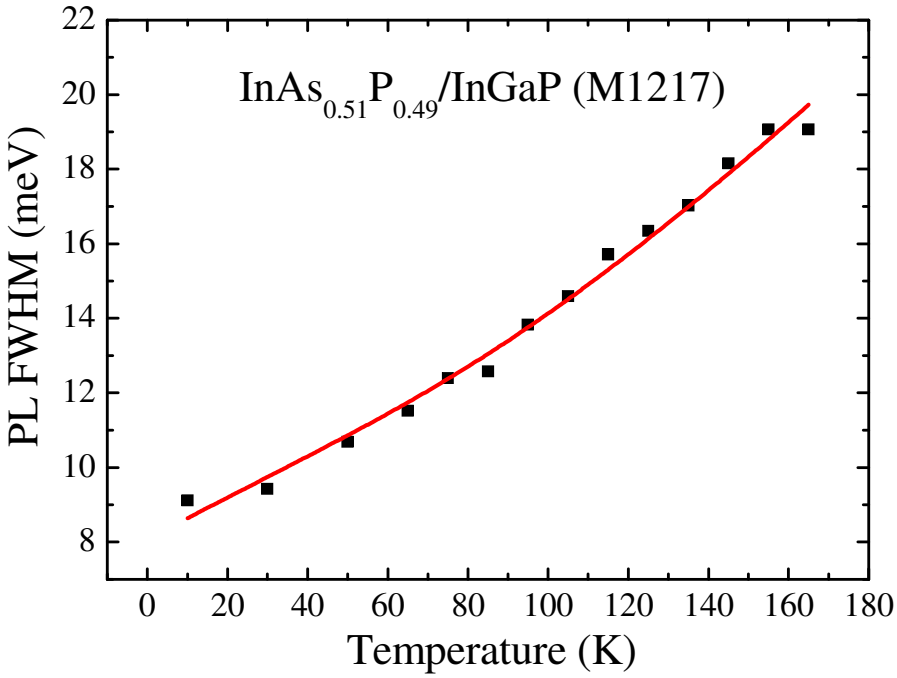

Fig. 44. Temperature dependence of the line width of PL spectra of the $InAs_{0.51}P_{0.49}$/InGaP (M1217) sample.

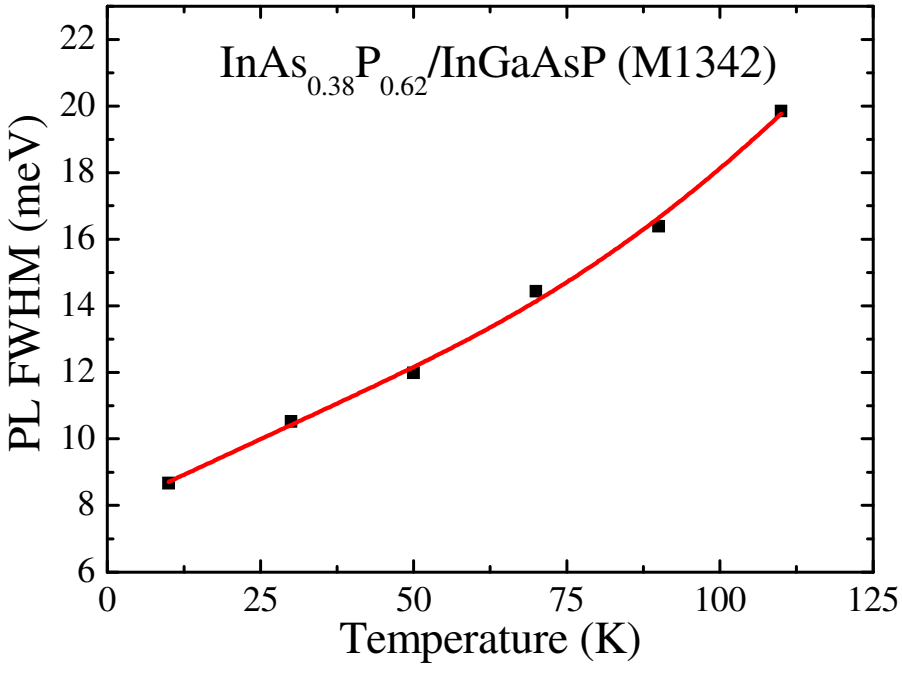

Fig. 45. Temperature dependence of the line width of PL spectra of the $InAs_{0.38}P_{0.62}$/InGaAsP (M1342) sample.

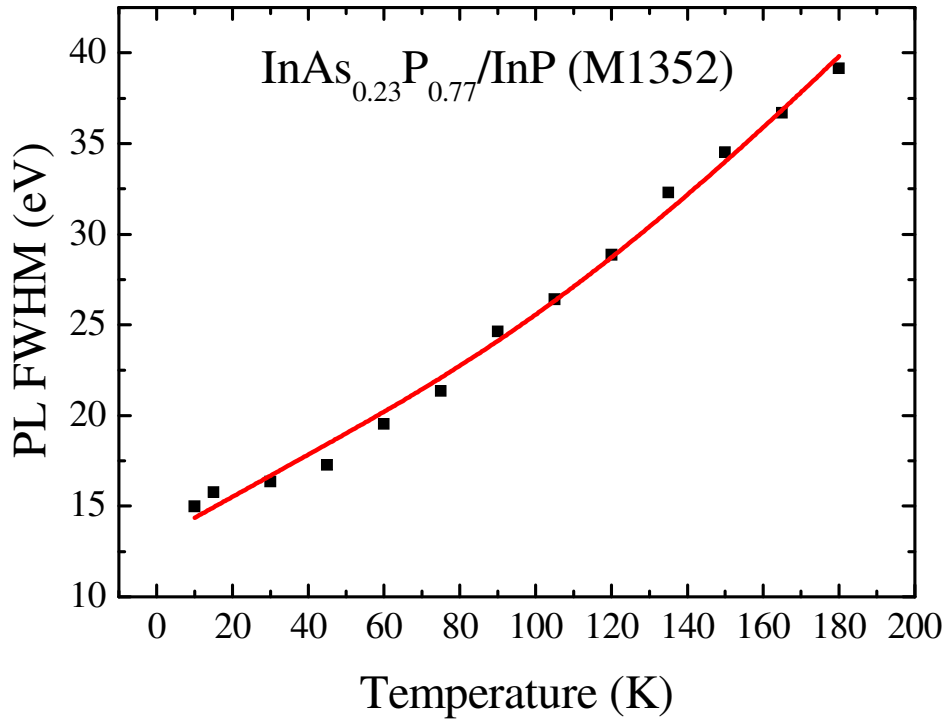

Fig. 46. Temperature dependence of the line width of PL spectra of the $InAs_{0.23}P_{0.77}$/InP (M1352) sample.

It is known, that the PL line shape is a convolution of inhomogeneous part and a temperature dependent homogeneous part. Inhomogeneous line width in MQWs is mainly due to alloy disorder, well width fluctuations compositional fluctuations in wells and barriers and the hetero-interface roughness [170]. Homogeneous part can be ascribed to the scattering between phonons and excitons, the carrier life broadening [170] and the interaction between carriers and excitons [171].

Thus, FWHM can be well-fitted to the exciton-photon coupling model [172]:

$$\Gamma = \Gamma_i + \Gamma_a T + \frac{\Gamma_b}{\exp(E_{LO}/k_B T) - 1}, \tag{6.28}$$

where Γ_i is inhomogeneous part, Γ_a, Γ_b are the corresponding coupling strengths with acoustic and longitudinal optical (LO) phonon, respectively, E_{LO} is the energy of LO phonon, and k_B is the Boltzmann constant. The least-square fitting procedure was applied to the PL line width data with the use of (6.28) equation. The results of the fittings are presented with red curves in Fig. 44–46, and the parameters, that shown the best fit for FWHM temperature dependence are listed in the Table 11. While comparing the experimental data and the fitting curves, one

can conclude, that model of exciton scattering with acoustic and longitudinal optical phonons describes well the thermal dynamics involved in the $InAs_xP_{1-x}$ MQWs.

Table 11. Parameters for fitting of the PL FWHM temperature dependences of $InAs_xP_{1-x}$ MQWs.

Sample No.	Sample structure	Γ_i, meV	Γ_a, meV/K	Γ_b, meV	E_{LO}, meV	InAs mole fraction (x) in the InAsP MQWs
M1217	$InAs_{0.51}P_{0.49}$/InGaP	8.09	0.055	22.9	32.89	0.51
M1342	$InAs_{0.38}P_{0.62}$/InGaAs	7.85	0.086	98.1	35.01	0.38
M1352	$InAs_{0.23}P_{0.77}$/InP	13.20	0.12	58.78	37.6	0.23

The inhomogeneous part Γ_i of all the samples are rather small, what may be evidence, that the samples were well epitaxed. The contributions of acoustic phonon scattering into homogeneous broadening practically do not differ from each other, whereas the coupling strengths with LO phonons differ significantly. The latter fact can be associated with different strains, involved in the well layers of the samples. The larger strength of exciton scattering with LO phonons corresponds to the more strained sample [156]. The E_{LO} values of all the samples are close to those for InAsP/InP and InAsP/InGaAsP samples reported in the literature [155,156]. As for bulk InAs and InP materials the LO phonon energy values are 29.6 meV and 42.8 meV respectively [173], the found E_{LO} values correspond with the mole fractions of InAs in the InAsP MQWs (Table 11).

Inasmuch as the FWHW of all the studied samples is strongly temperature-dependent, and at T>100 K the sharpness of the lines decreases intensively due to failure of the quantum confinement cryterium (6.23), the application of high-pressure sensors, based on InP-structures is confined with temperature. Thus, the high-pressure calibration of the potential InP-based pressure sensors should be performed only for the definite temperature range $T = (10 \div 150)$ K. On the other hand, the pressure range of the calibration process $p = (0 \div 100)$ kbar is limited by the estreme decrease of the PL intensity at about $p \approx 105$ kbar, which is irreversible and probably due to the phase transition of the InAsP material.

6.4.4. Excitation power dependences of the PL spectra

The emission dependences on excitation power were measured in order to test the applicability range of the potential pressure sensors. During stress measurements the studied samples in the DAC sometimes need to be excited with higher powers, especially at high pressure values, when PL signal usually becomes weak. In such a case it would be very convenient to have a pressure sensor, which could be excited with the same laser power, as the sample.

Two samples were chosen to test their emission bands behavior with excitation power increase. The PL spectra of the M1217 ($InAs_{0.51}P_{0.49}$/InGaP) and M1342 ($InAs_{0.38}P_{0.62}$/InGaAs) samples were taken at the excitation power range of (20–210) mW and (10–230) mW respectively. The measurements were carried out at T=10 K, and the temperature was strictly controlled during the experiment.

In order to estimate the power density of the excitation laser beam on the sample, one should take into account the following. In compliance with the technical characteristics of the optical devices, applied in the experiment, the total losses at one mirror, two CaF_2 lenses, a glass cryostat windows and, finally, a diamond do not exceed 10% of the initial laser power value. In order to estimate the diameter of the first diffraction ring (so called, Airy disc) of the laser beam the following formula is usually used:

$$D_{Airy} = 2.44 \cdot \lambda \cdot \frac{f}{D}, \tag{6.29}$$

where f is a focal length, D is a diameter of the free opening, and λ is an excitation wavelength. However, due to the minimal refraction effects occurred on the lenses, cryostat windows and diamonds, the laser beam spot, focused on the sample in the DAC usually was ellipse-shaped. The lengths of the major and minor ellipse axes can be approximately estimated from the typical size of the sample. They are assumed to be equal to 90 μm and 20 μm respectively. Then, the area of the laser beam spot on the sample is $1.414 \cdot 10^{-5}$ cm^2. While taking into consideration the mentioned above power losses, the laser power density on the sample can be calculated by the following formula:

$$\omega \left[\frac{mW}{cm^2} \right] \approx 7.07 \cdot 10^3 \cdot P_{exc}^{initial} \left[mW \right]. \tag{6.30}$$

The dependences of the emission spectra on the excitation power value are shown in Fig. 47, 48. The plotted PL peak intensities versus initial laser excitation power ($P_{cxc}^{initial}$) and

the corresponding laser power density on the sample are presented in Fig. 49. In order to study the change of the PL band sharpness dependently on excitation power, the FWHM=$f(P_{exc})$ was studied as well (Fig. 50).

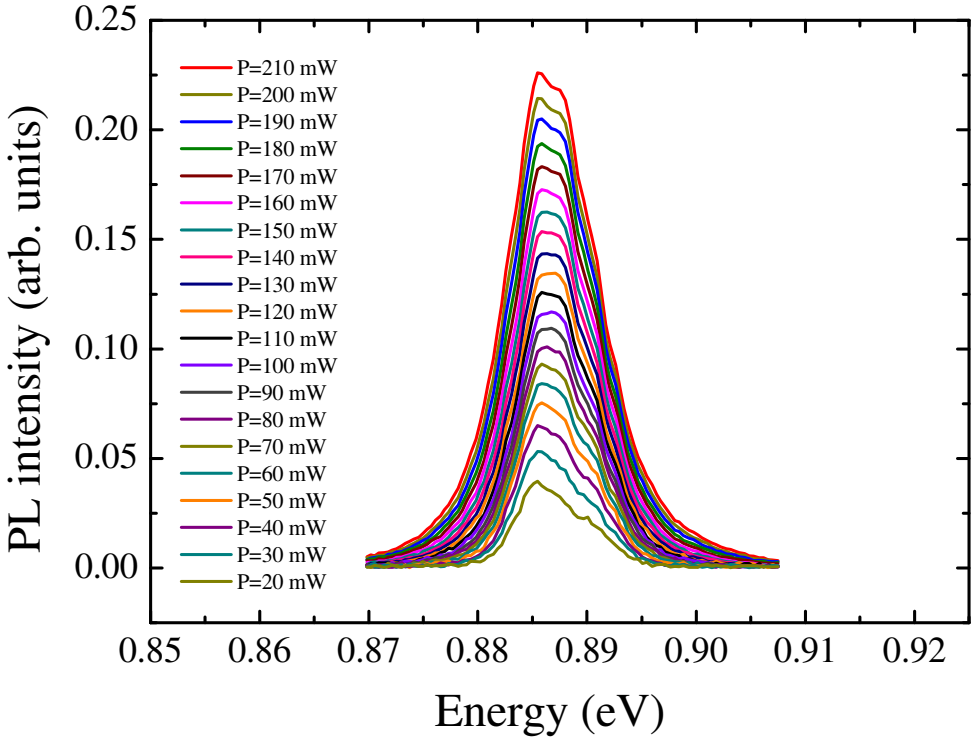

Fig. 47. The excitation power dependent PL spectra of the $InAs_{0.51}P_{0.49}$/InGaP (M1217) sample measured at T=10 K.

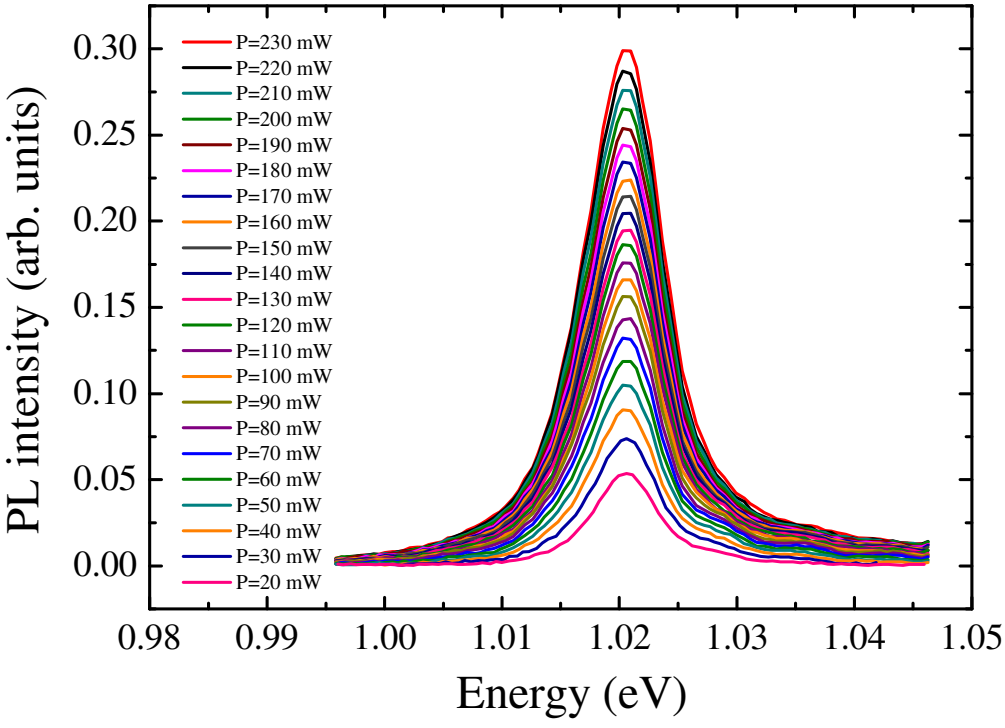

Fig. 48. The excitation power dependent PL spectra of the $InAs_{0.38}P_{0.62}$/InGaAsP (M1342) sample measured at T=10 K.

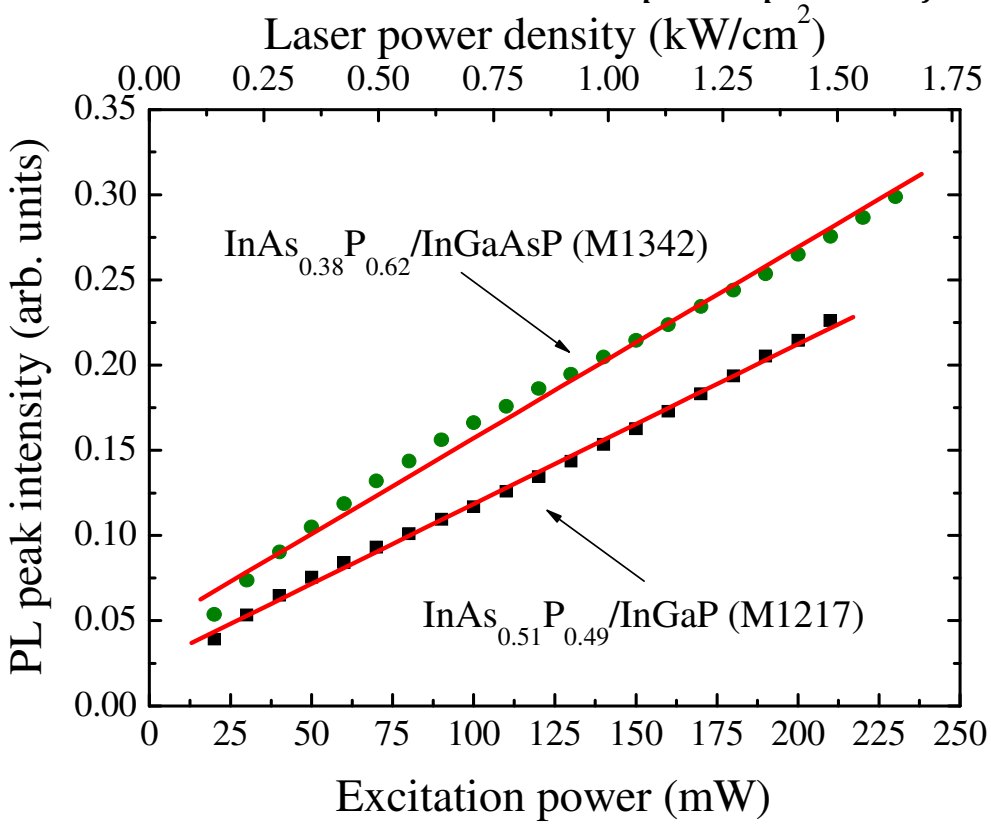

Fig. 49. The dependences of PL peak intensities on excitation power of the$InAs_{0.51}P_{0.49}$/InGaP (M1217) and $InAs_{0.38}P_{0.62}$/InGaAsP (M1342) samples. The corresponding laser power density values are shown on the upper abscissa axis.

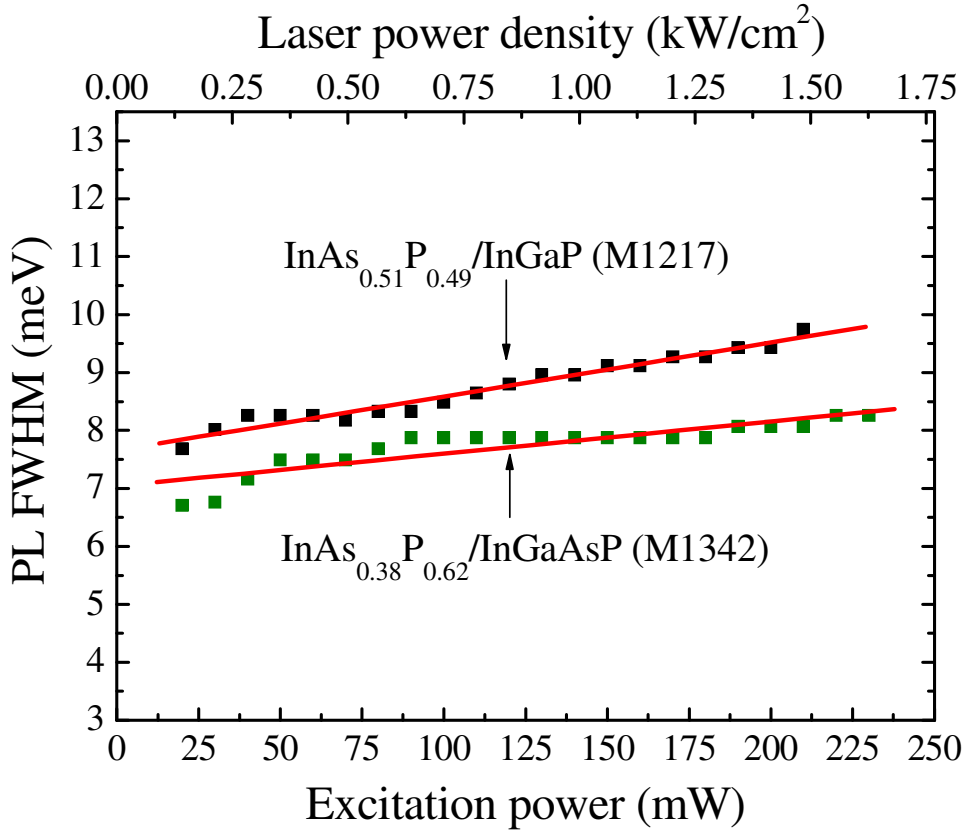

Fig. 50. Excitation power dependence of the line width of PL spectra of the $InAs_{0.51}P_{0.49}$/InGaP (M1217) and $InAs_{0.38}P_{0.62}$/InGaAsP (M1342) samples. The corresponding laser power density values are shown on the upper abscissa axis.

It is clearly seen, that with the excitation power increase the emission peak remains at the same energy (Fig. 47, 48), and the PL intensity rises significantly. Fig. 49 shows, that the emission intensity reveals a linear dependence on laser excitation power (with an insignificant deviation from linearity to within the experimental error). Fig. 50 indicates, that the line widths reveal very small linear change with the excitation power increase: 9.3 μeV/mW and 5.6 μeV/mW for M1217 ($InAs_{0.51}P_{0.49}$/InGaP) and M1342 ($InAs_{0.38}P_{0.62}$/InGaAs) samples respectively.

In order to calculate the error pressure, originating from the temperature change due to illumination process, occurred in the samples, one should execute the following procedure.

1. To obtain from the Fig. 50 the change of the mean FWHM values, corresponding to the variation of the excitation power from $P_{exc1} = 10$ mW up to $P_{exc2} = 230$ mW.
2. To use the equation (6.28) for the numerical calculation of the corresponding changes of the temperature.
3. While using the $E_g=f(T)$ dependences (Fig. 39 and Fig. 41), to determine the ΔE_g values corresponding to the ΔT changes.
4. To calculate the absolute error of the pressure value reading, with the use of the (6.31) equation (which will be detaily introduced and substantiated in the following Section). The results of these estimations are listed in the Table 12.

Table 12. The estimation of the pressure reading errors due to the illumination process of the stress gauges based on the InAsP quantum wells.

Sample No.	Sample structure	$\Delta\Gamma_{(10–230)\ mW}$, meV	$\Delta T_{(10–230)\ mW}$, K	$\Delta E_{g\ (10–230)\ mW}$, meV	$\Delta p_{(10–230)\ mW}$, kbar
M1217	$InAs_{0.51}P_{0.49}$/InGaP	2.046	31	0.88581	0.61
M1342	$InAs_{0.38}P_{0.62}$/InGaAs	1.225	5.5	1.02053	1.89

Thus, if one assumes, that the temperature insignificantly varies due to the illumination processes, the absolute reading errors do not exceed 2 kbar for the wide excitation power range P_{exc}=(10…230) mW (in the applied experimetnal setup). These investigations lead up to the essential conclusion about the possibility to use the studied MQWs as DAC high-pressure sensors, which can be operable as well at high excitation power densities.

6.5. High-pressure calibration of the MQWs

High-pressure PL measurements of all the samples were performed in the pressure range of (0−100) kbar at 10, 50 and 100 K. The obtained PL spectra were found to be very similar; hence, the plots of PL intensity versus pressure are presented for two boundary cases: 10 K (Fig. 51, 55, 59) and 100 K (Fig. 53, 57, 61). At the same time the variation of PL peak positions with pressure are shown for 10 K (Fig. 52, 56, 60), 100 K (Fig. 54, 58, 62) and also for 50 K (Fig. 63−65). As one can notice, the latter dependencies have a slightly bowing shape, and they were fitted with the use of the equation (3.9):

$$E_{PL\ peak} = E_0 + Bp + Cp^2 .$$

The red curves in Fig. 52, 54, 56, 58, 60, 62, 63−65 represent the performed fittings, and the parameters, which showed the best fits, are listed in the Table 13.

Table 13. Parameters, showed the best fits for the pressure dependences of the PL peak position of the studied InP-based MQWs.

Sample No.	Sample structure	Temperature, K	Fit parameters		
			E_0, eV	B, meV/kbar	$C\times10^{-2}$, meV/kbar^2
M1217	$InAs_{0.51}P_{0.49}$/InGaP	10	0.896 ±0.002	7.65 ±0.103	−1.033 ±0.099
		50	0.894 ±0.003	8.14 ±0.00	−1.0 ±0.057
		100	0.892 ±0.003	7.73 ±0.00	−1.0 ±0.063
M1342	$InAs_{0.38}P_{0.62}$/InGaAs	10	1.027 ±0.004	7.39 ±0.17	−0.607 ±0.162
		50	1.023 ±0.003	7.27 ±0.14	−0.954 ±0.139
		100	1.016 ±0.007	7.72 ±0.33	−0.830 ±0.323
M1352	$InAs_{0.23}P_{0.77}$/InP	10	1.184 ± 0.003	8.14 ±0.12	−1.567 ±0.110
		50	1.183 ±0.004	7.99 ±0.17	−1.510 ±0.162
		100	1.176 ±0.003	8.28 ±0.14	−1.572 ±0.132

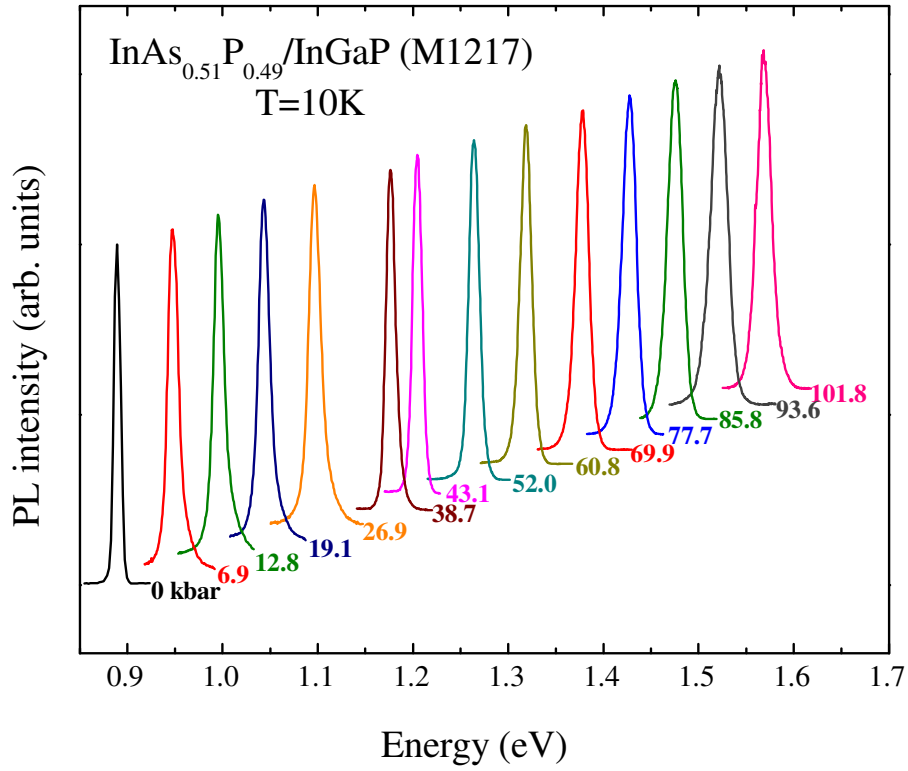

Fig. 51. Pressure dependence of PL spectra of the $InAs_{0.51}P_{0.49}$/InGaP (M1217) sample at T=10 K.

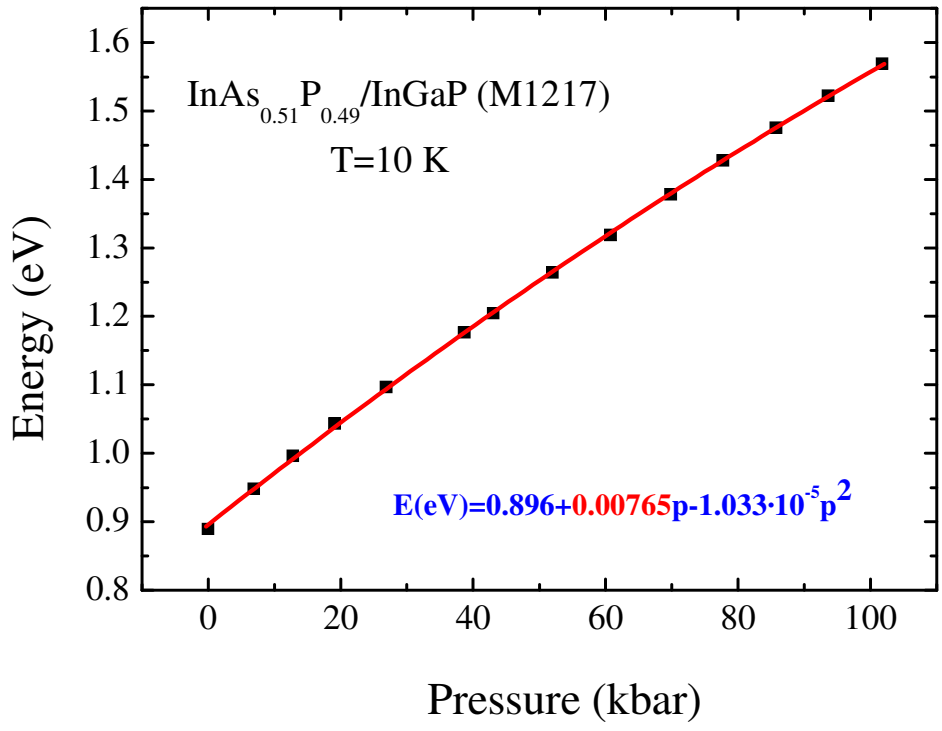

Fig. 52. Pressure dependence of the PL peak position of the $InAs_{0.51}P_{0.49}$/InGaP (M1217) MQW at T=10 K.

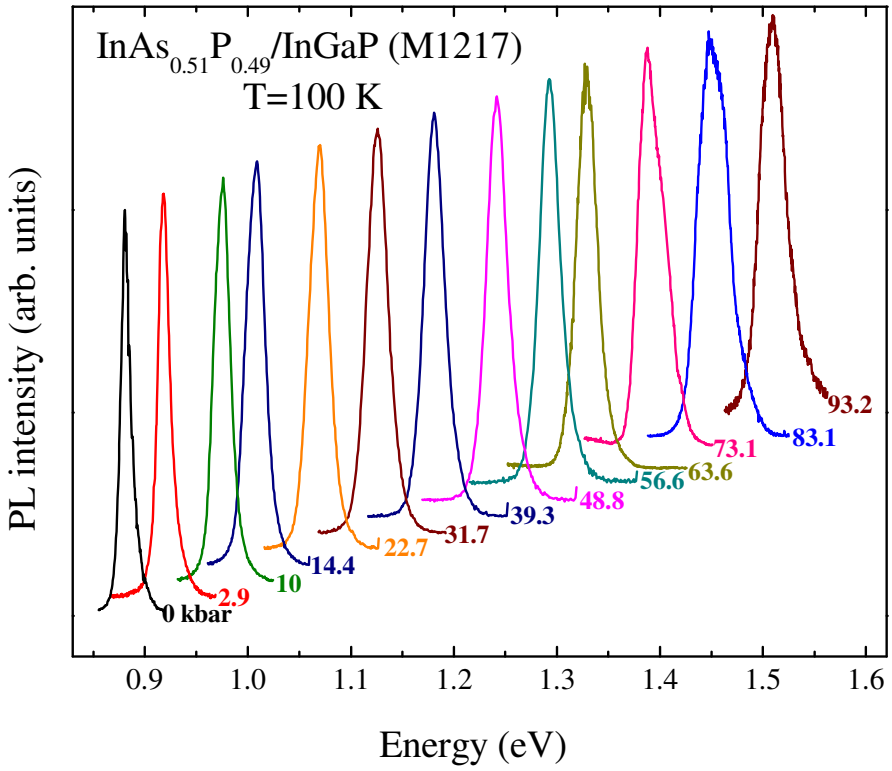

Fig. 53. Pressure dependence of PL spectra of the $InAs_{0.51}P_{0.49}$/InGaP (M1217) sample at T=100 K.

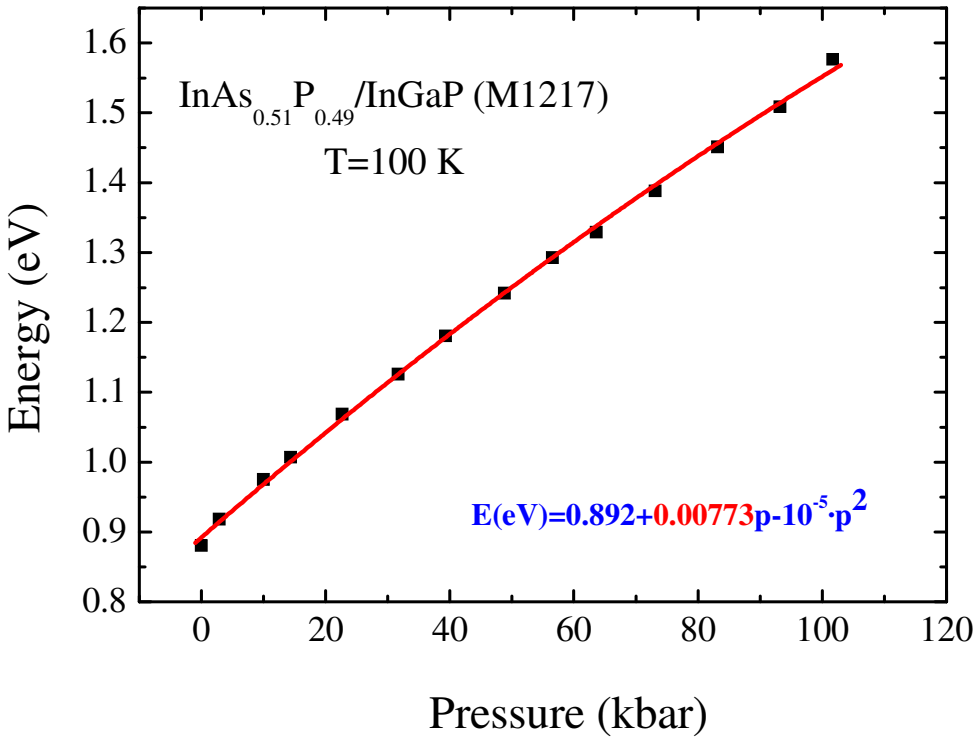

Fig. 54. Pressure dependence of the PL peak position of the $InAs_{0.51}P_{0.49}$/InGaP (M1217) MQW at T=100 K.

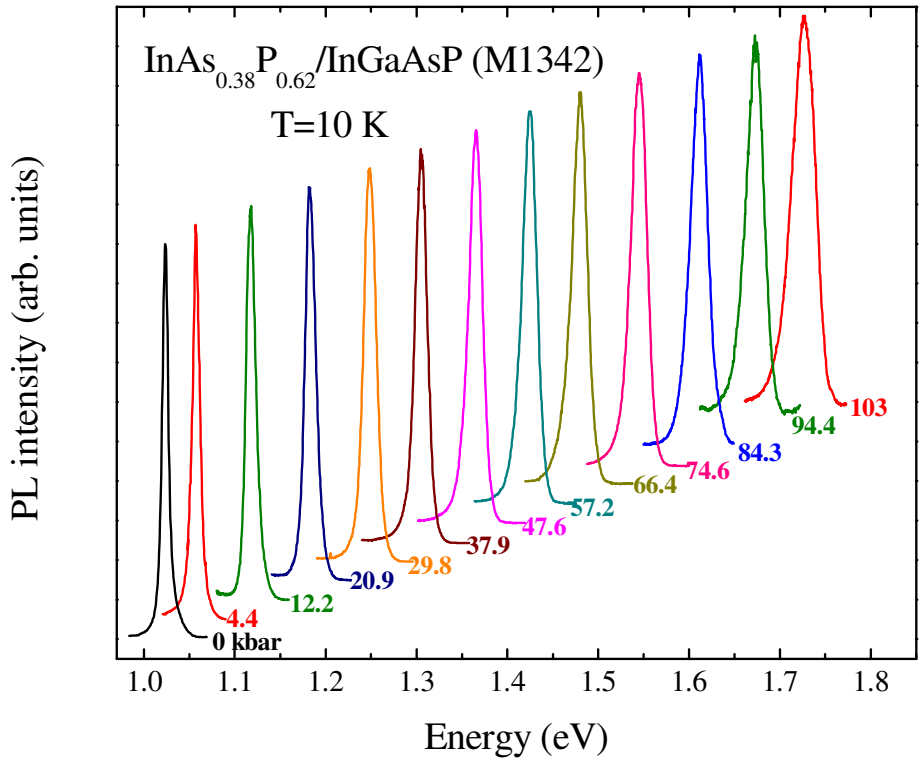

Fig. 55. Pressure dependence of PL spectra of the $InAs_{0.38}P_{0.62}$/InGaAsP (M1342) sample at T=10 K.

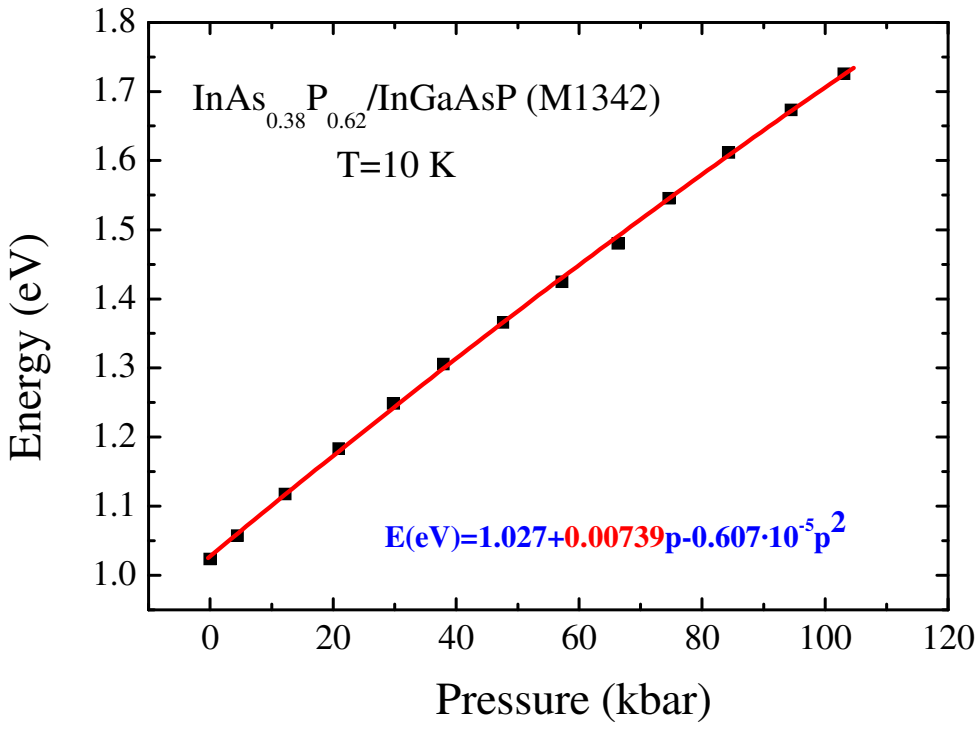

Fig. 56. Pressure dependence of the PL peak position of the $InAs_{0.38}P_{0.62}$/InGaAsP (M1342) MQW at T=10 K.

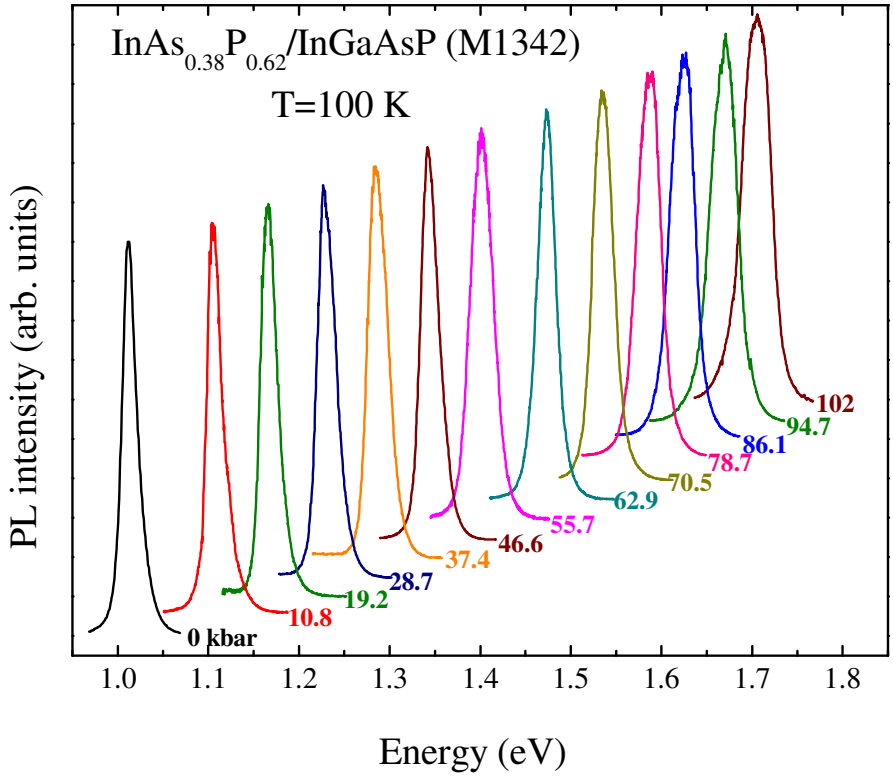

Fig. 57. Pressure dependence of PL spectra of the $InAs_{0.38}P_{0.62}$/InGaAsP (M1342) sample at T=100 K.

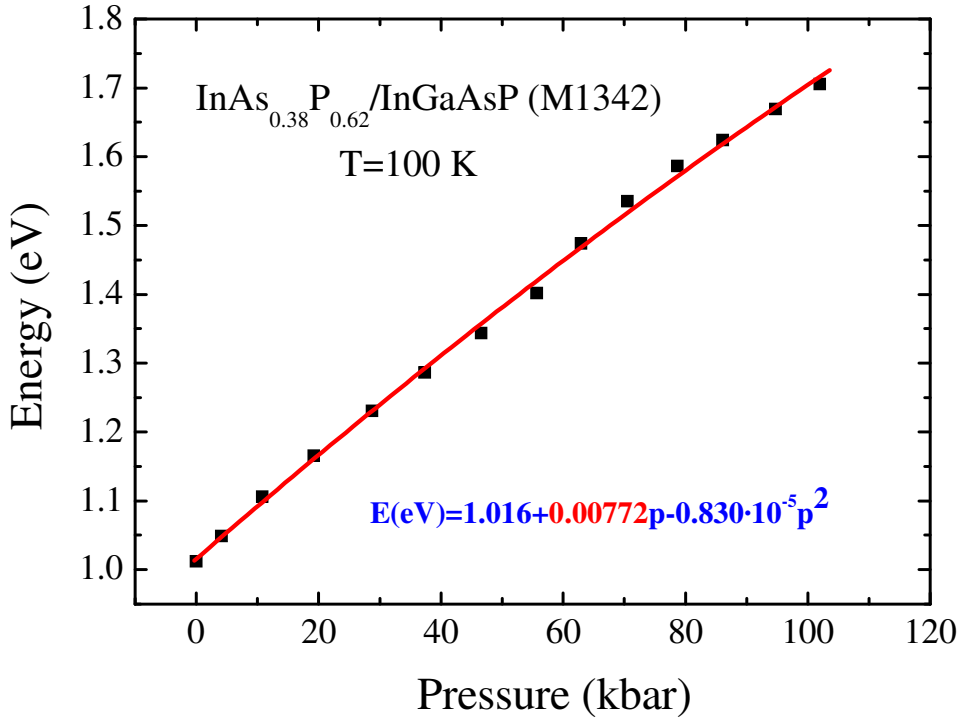

Fig. 58. Pressure dependence of the PL peak position of the $InAs_{0.38}P_{0.62}$/InGaAsP (M1342) MQW at T=100 K.

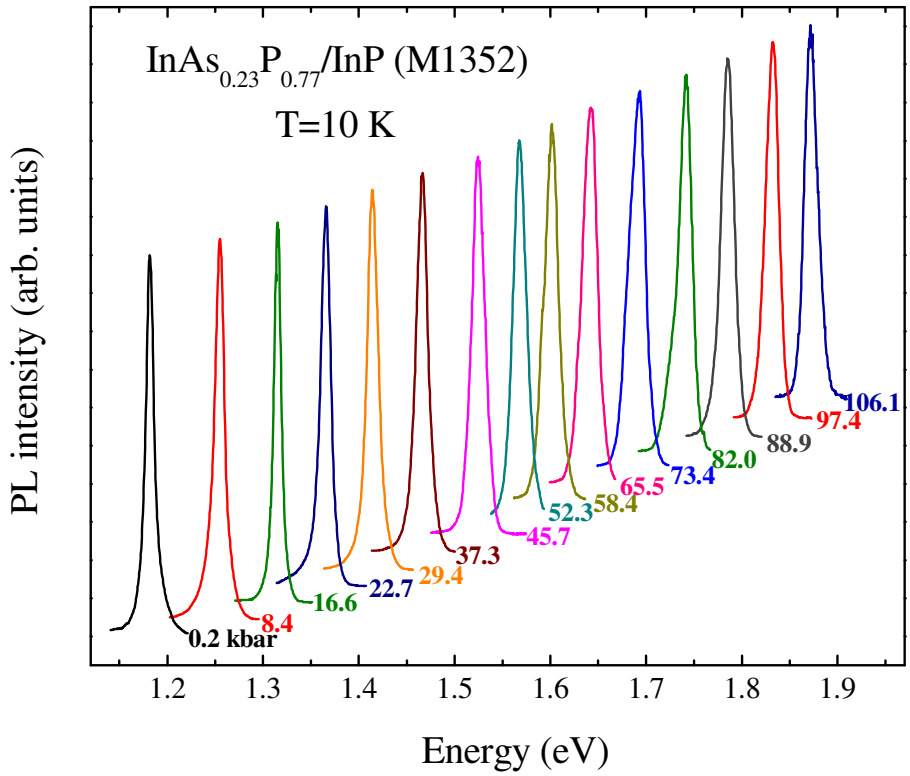

Fig. 59. Pressure dependence of PL spectra of the $InAs_{0.23}P_{0.77}$/InP (M1352) sample at T=10 K.

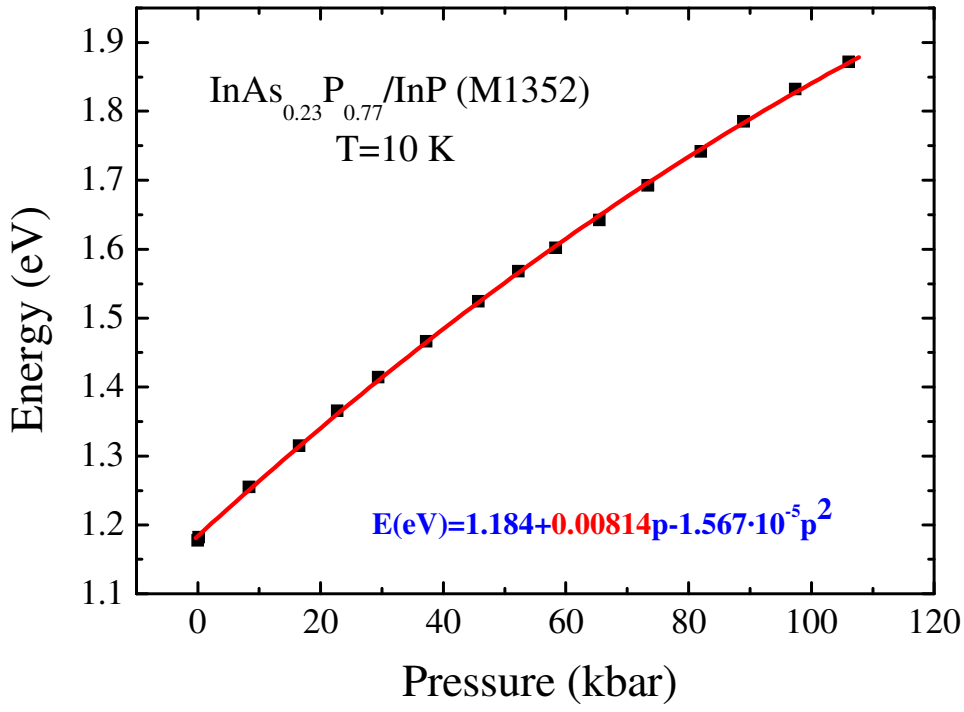

Fig. 60. Pressure dependence of the PL peak position of the $InAs_{0.23}P_{0.77}$/InP (M1352) MQW at T=10 K.

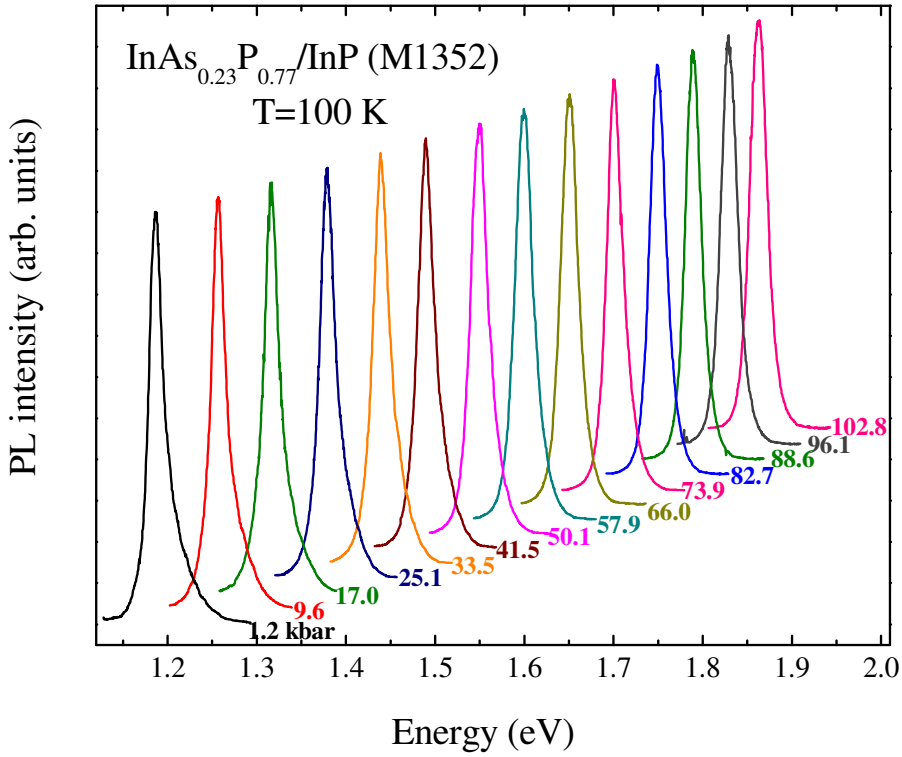

Fig. 61. Pressure dependence of PL spectra of the $InAs_{0.23}P_{0.77}$/InP (M1352) sample at T=100 K.

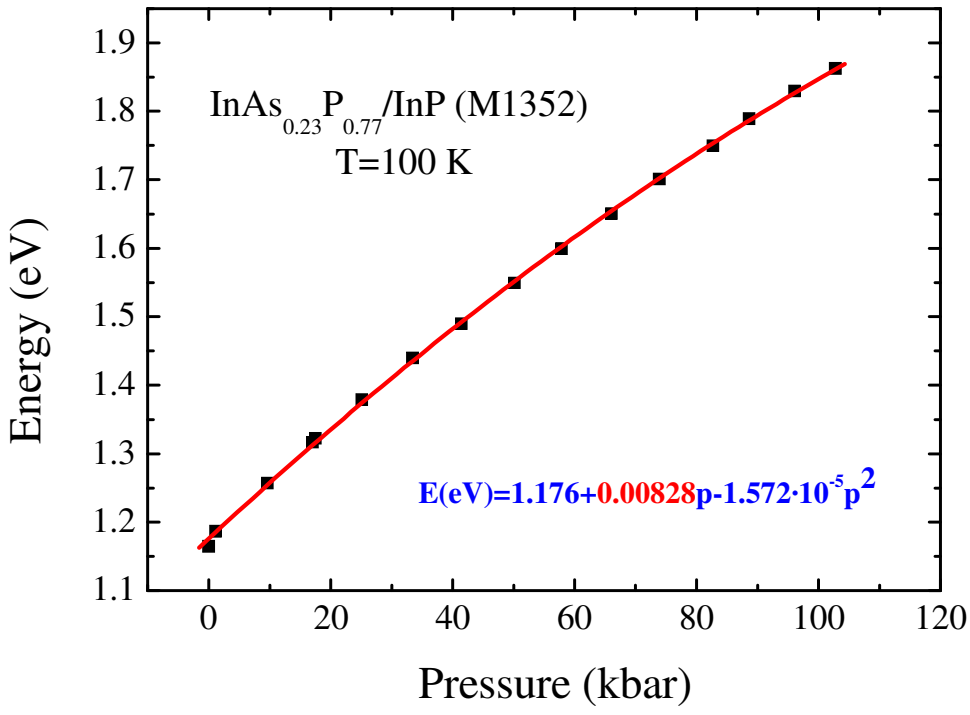

Fig. 62. Pressure dependence of the PL peak position of the $InAs_{0.23}P_{0.77}$/InP (M1352) MQW at T=100 K.

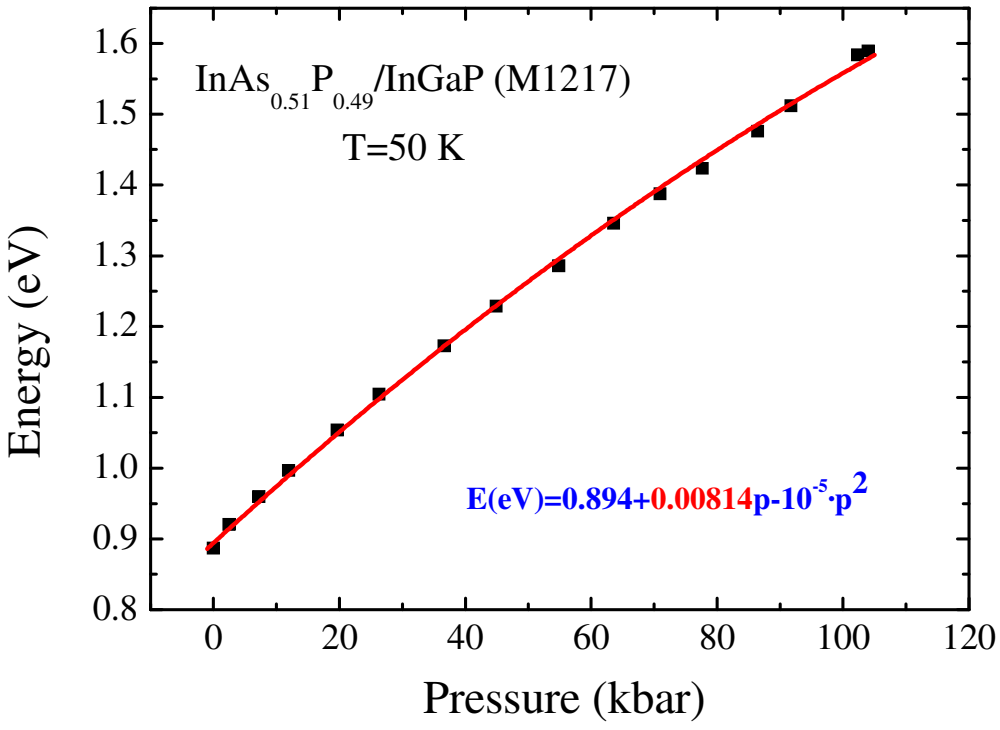

Fig. 63. Pressure dependence of the PL peak position of the $InAs_{0.51}P_{0.49}$/InGaP (M1217) MQW at T=50 K.

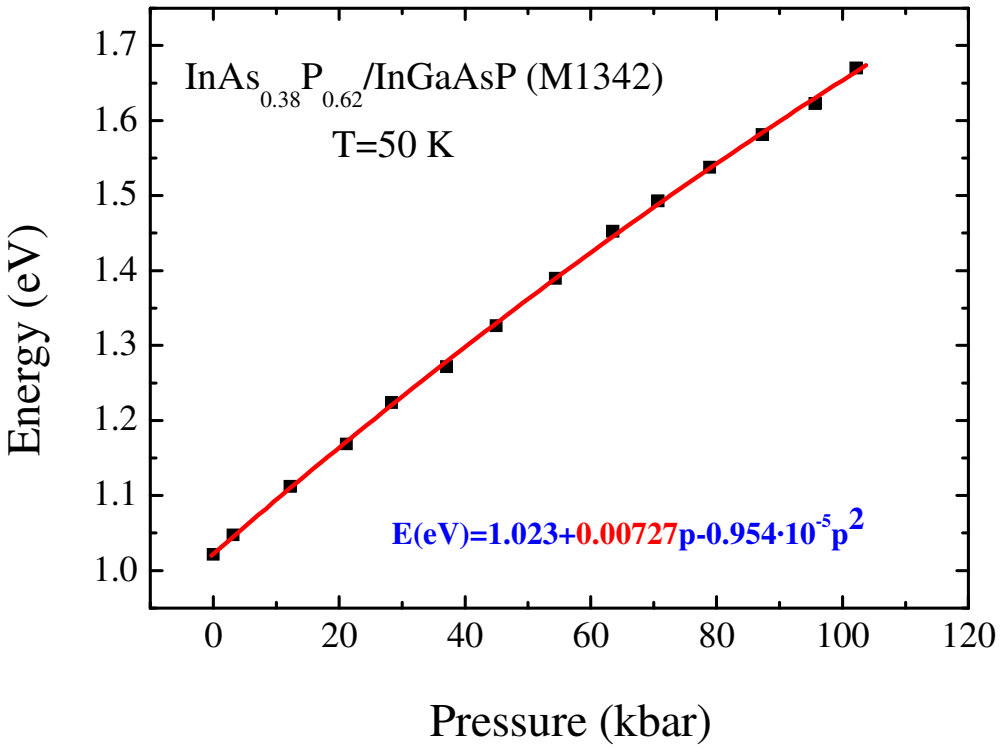

Fig. 64. Pressure dependence of the PL peak position of the $InAs_{0.38}P_{0.62}$/InGaAsP (M1342) MQW at T=50 K.

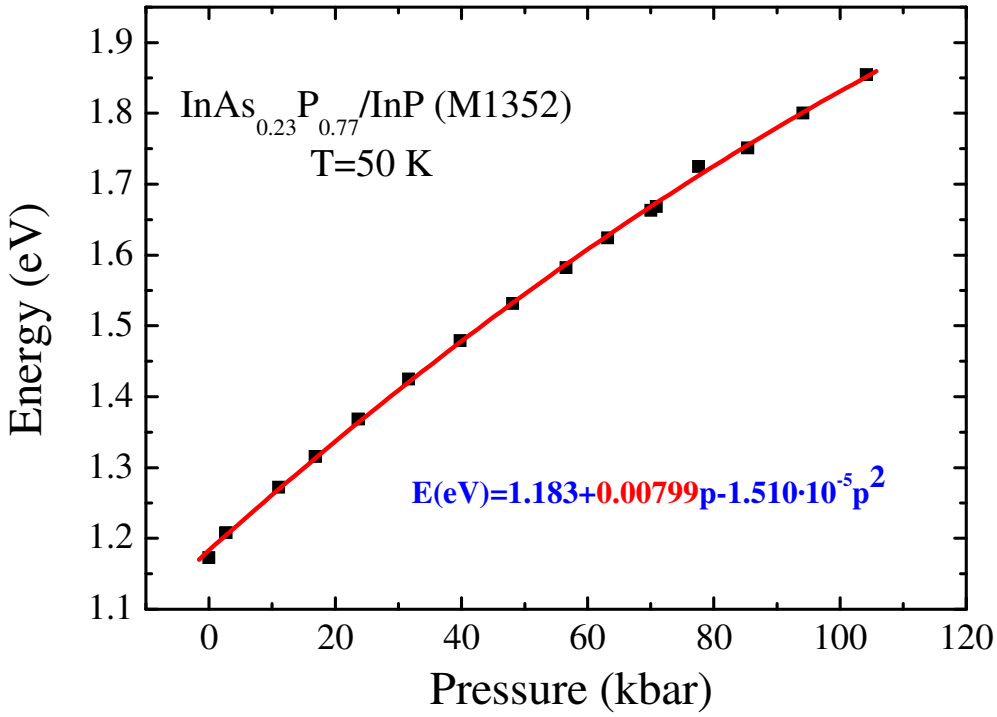

Fig. 65. Pressure dependence of the PL peak position of the $InAs_{0.23}P_{0.77}$/InP (M1352) MQW at T=50K.

The theoretical reports with the comprehensive quantitative analysis of the PL behaviour under high pressure for InAsP-based MQWs are not known to the author. Nevertheless, the main factors, which can be resposible for the observed PL band shift are the following [136].

1. The increase of the energy gap with pressure.

   This factor has already been partially discussed in the Section 3.1. With regard to the quantum structures, some authors declare the dE_g/dp value to be lower in comparison with the appropriate bulk materials [174-176].
2. The lowering of the quantization energy of electrons due to the effective mass increase with pressure.
3. The change of quantization energy for holes due to the variation of the light-hole effective mass with pressure.

As the pressure coefficient of the PL band position for all the InAsP-based MQWs (Table 13, fit parameter – B) is close to the dE_g/dp value, reported for InAsP/InP quantum well (9.5 meV/kbar [177]), one can assume, that the bandgap change with pressure is the factor, which mostly defines the PL peak behaviour at high stress application to the studied samples. A detailed theoretical analysis of this matter could clarify the matter, although it is beyond the scope of the present Thesis.

One should notice (Table 13) that for each sample the fit parameters except E_0 value are close to each other, and the insignificant difference in their proper values can be explained by the experimental error. This observation motivated the author to perform the following operation. The pressure dependences of PL peak position for each sample and different temperatures (T=10 K, 50 K, 100 K) were plotted on one frame of axis and fitted with the use of (3.9) equation. The green curves in Fig. 66 represent the performed fits (which will be mentioned below as "Fits-1"), and the parameters, which showed the best fits, are listed in the Table 14.

One can see (Table 14) that the pressure coefficients B for all the samples are equal to about 8meV/kbar and the bowing parameter C is very small (about 10^{-5} meV/kbar). This circumstance served as a motivation to try to find the common parameters B_1 and C_1 for all the samples in order to propose the explicit form of the equation (3.9), which would be valid for the PL peak pressure dependences of all three InP-based MQWs. For this purpose the PL peak positions of all the samples and for all the temperatures were plotted on one frame of axis and fitted by means of least-square fitting procedure with the use of (3.9) formula. The red curve, shown on Fig. 66 presents the result of this fitting by which the common

Table 14. The common fitting parameters of the pressure dependences of the MQWs PL peak position measured at different temperatures (T=10, 50, 100 K).

Sample No.:	Sample structure:	Temperature, K	Fit parameters		
			E_0, eV	B, meV/kbar	$C\times10^{-2}$, meV/kbar^2
M1217	$InAs_{0.51}P_{0.49}$/InGaP	10, 50, 100	0.898 ±0.003	7.59 ±0.12	−0.981 ±0.163
M1342	$InAs_{0.38}P_{0.62}$/InGaAs	10, 50, 100	1.022 ±0.006	7.46 ±0.28	−0.808 ±0.265
M1352	$InAs_{0.23}P_{0.77}$/InP	10, 50, 100	1.181 ± 0.021	8.12 ±0.10	−2.000 ±0.097

parameter B_1=7.95 meV/kbar and C_1=0.01meV/kbar^2 were found. Afterwards the pressure dependences of the PL peak positions for each sample and all three temperatures (T=10 K, 50 K, 100 K) were fitted with the use of the found B_1 and C_1 parameters. These fits will be mentioned below as "Fits-2" and their results are present in Fig. 67 and Table 15.

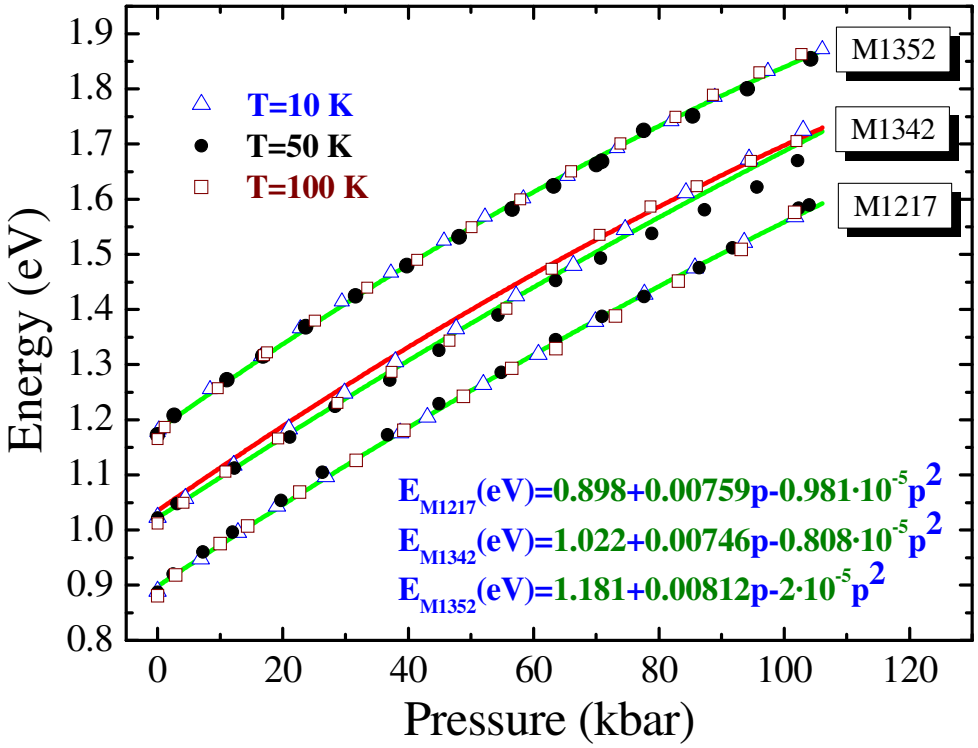

Fig. 66. Pressure dependence of the PL peak position of the $InAs_{0.51}P_{0.49}$/InGaP (M1217), $InAs_{0.38}P_{0.62}$/InGaAsP (M1342) and $InAs_{0.23}P_{0.77}$/InP (M1352) samples at T=10, 50, 100 K fitted with the use of (3.9) equation for each sample (green curves) separately. The red curve represents the result of the least-square fitting procedure applied to PL peak position data of all the samples for all pressure values and temperatures.

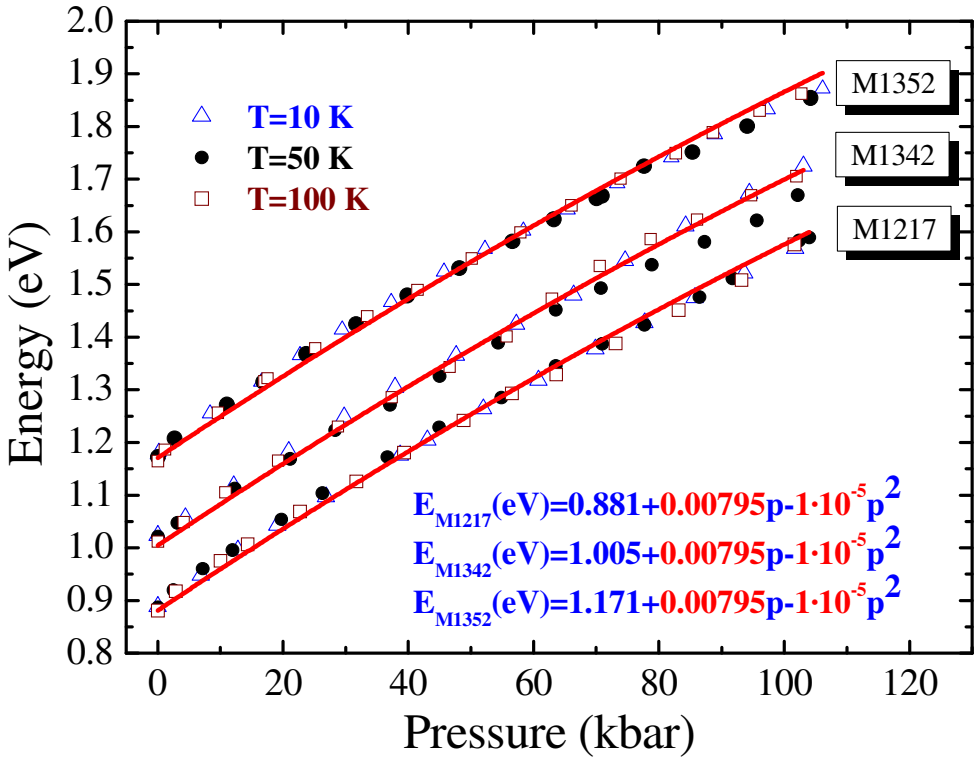

Fig. 67. Pressure dependence of the PL peak position of the $InAs_{0.51}P_{0.49}$/InGaP (M1217), $InAs_{0.38}P_{0.62}$/InGaAsP (M1342) and $InAs_{0.23}P_{0.77}$/InP (M1352) samples at T=10, 50, 100 K fitted with the use of (3.9) with the common B_1=7.95 meV/kbar and C_1=0.01meV/kbar^2 parameters.

Table 15. The E_0 parameter obtained as a result of the fitting of pressure dependences of the MQWs PL peak position measured at different temperatures (T=10, 50, 100 K). (The fitting procedure was performed with the common B_1 and C_1 parameters).

Sample No.:	Sample structure:	Temperature, K	Fit parameters		
			E_0, eV	B_1, meV/kbar	$C_1\times10^{-2}$, meV/kbar^2
M1217	$InAs_{0.51}P_{0.49}$/InGaP	10, 50, 100	0.881 ±0.002	7.95	1
M1342	$InAs_{0.38}P_{0.62}$/InGaAs	10, 50, 100	1.005 ±0.003		
M1352	$InAs_{0.23}P_{0.77}$/InP	10, 50, 100	1.171 ± 0.002		

The misoverlapping of the curves, obtained in Fits-1 and Fits-2 result in the difference of E_0 values, listed in the Tables 13 and 15. Fig. 68 (left scale) presents the subtraction of Fits-1 and Fits-2 energy values ΔE for the pressure range (0–100) kbar. These plots (Group 1) make it possible to determine the maximum deviation of the fitted values (and the relative error) which were found to be 17.6 meV (2.53%) 17.2 meV (2.45%) and 26.2 meV (3.8%) for $InAs_{0.51}P_{0.49}$/InGaP (M1217), $InAs_{0.38}P_{0.62}$/InGaAsP (M1342) and $InAs_{0.23}P_{0.77}$/InP (M1352) samples respectively.

In order to estimate the absolute error, which is made as a result of using of Fits-2 curves instead of Fits-1 ones, the equation (3.9) has to be solved for the p values (with the subtstituted E_0, B and C constants taken from Table 14) and $E_{PL\,peak}$ assumed as

$$E_{PL\,peak} = E_0 + |\Delta E|.$$

Here E_0 and $|\Delta E|$ values have to be taken from the Table 14 and from the Group 1 curves (Fig. 68) for each sample relatively. The absolute values of the solutions of the equation (3.9) are plotted as Group 2 curves in the Fig. 68. Thus, the maximum errors of the pressure values, defined with the use of the Fits-2 calibration curves can be obtained. They were found to be 2.21 kbar, 2.17 kbar and 3.31 kbar for $InAs_{0.51}P_{0.49}$/InGaP (M1217), $InAs_{0.38}P_{0.62}$/InGaAsP (M1342) and $InAs_{0.23}P_{0.77}$/InP (M1352) samples respectively.

As the relative and maximum absoulute errors are rather small, the accuracy of the Fits-2 can be considered sufficient for the parameters B_1 and C_1 to be used for the construction of the high-pressure calibration curves for the analogous InP-based MQWs.

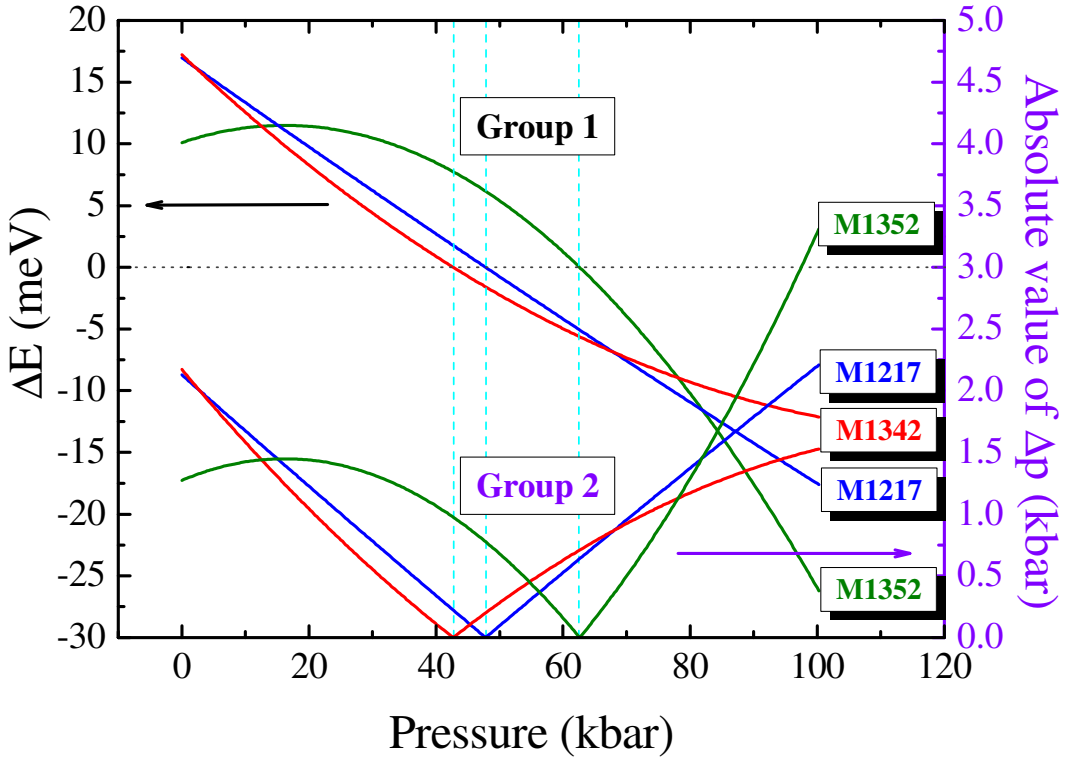

Fig. 68. The difference between the PL peak position energies obtained as a result of Fits-1 and Fits-2 subtraction for the pressure range of (0–100) kbar (Group 1 curves, left ordinate axis); and the absolute error, made as a result of using of Fits-2 curves instead of Fits-1 ones (Group 2 curves, right ordinate axis).

Thus, it is enough to measure the PL peak position of the appropriate quantum structure at ambient pressure and temperature range (10–100) K, and considering the obtained value as E_0, one can use the equation

$$E(eV) = E_0 + 7.95 \cdot 10^{-3} p - 10^{-5} p^2 \tag{6.31}$$

for the construction of the calibration curve of the pressure sensor.

While analizing the latter function, one can notice, that the derivative

$$\left(\frac{dE}{dp}\right)_{MQWs} = 7.95 \cdot 10^{-3} - 2 \cdot 10^{-5} p \tag{6.32}$$

takes the maximum and minimum values at pressure values equal 0 and 100 kbar respectively. For the sake of simplicity one can assume, that

$$\left.\left(\frac{dE}{dp}\right)\right|_{p=0kbar} \approx \left.\left(\frac{dE}{dp}\right)\right|_{0kbar<p<100kbar} = 7.0\frac{meV}{kbar}.$$

For ruby pressure sensor the $\frac{dE}{dp}$ value is taken from [126] and listed in the Table 5: $\frac{dE}{dp} = 0.094 \frac{meV}{kbar}$. Thus, one can roughly estimate that InP-based MQW pressure sensors comparably to the ruby pressure gauges are characterized by the sensitivity gain, equal

$$\frac{\left(\frac{dE}{dp}\right)_{MQWs}}{\left(\frac{dE}{dp}\right)_{ruby}} = \frac{7.0}{0.094} \approx 74.5 .$$

Meanwhile, the sensitivity gain value is reduced by the greater PL FWHM values of the studied MQWs as compared to ruby. Besides, due to the nonhydrostatic effects in the DAC, the line width of the PL band additionally increases with pressure growth. Fig. 69–71 present the plots of PL FWHM versus hydrostatic stress, and, as one can see, these changes reveal a non-monotonic growth with pressure. The average PL FWHM values at ambient and high pressures of the studied MQWs as well ruby, used in the experiment as pressure gauge are listed in the Table 16.

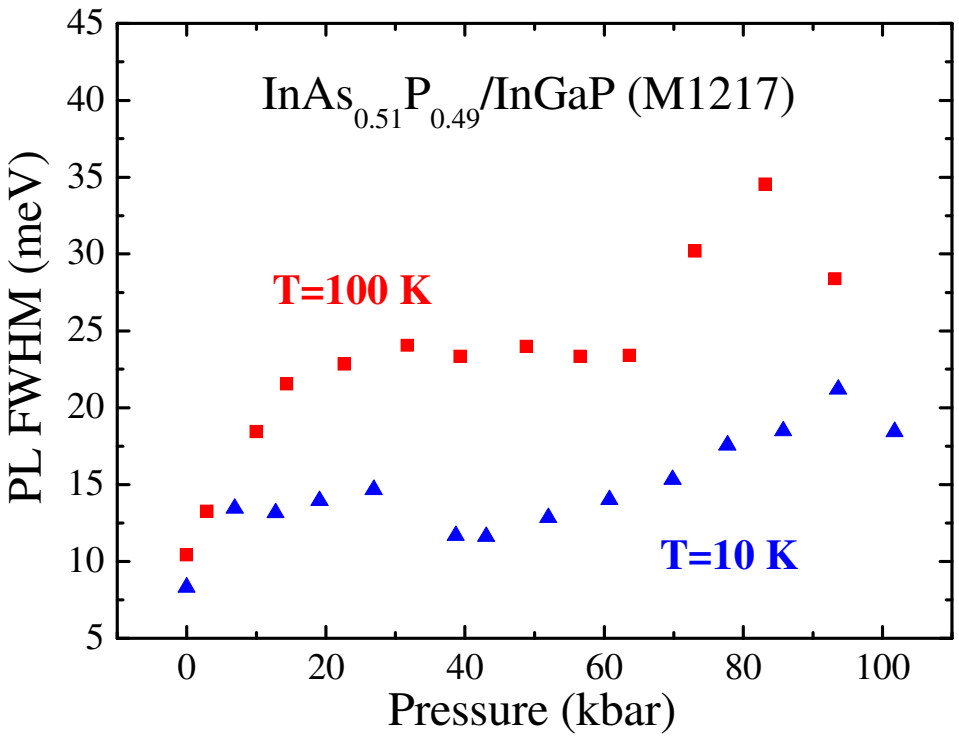

Fig. 69. Pressure dependence of the line width of the PL spectra of $InAs_{0.51}P_{0.49}$/InGaP (M1217) sample

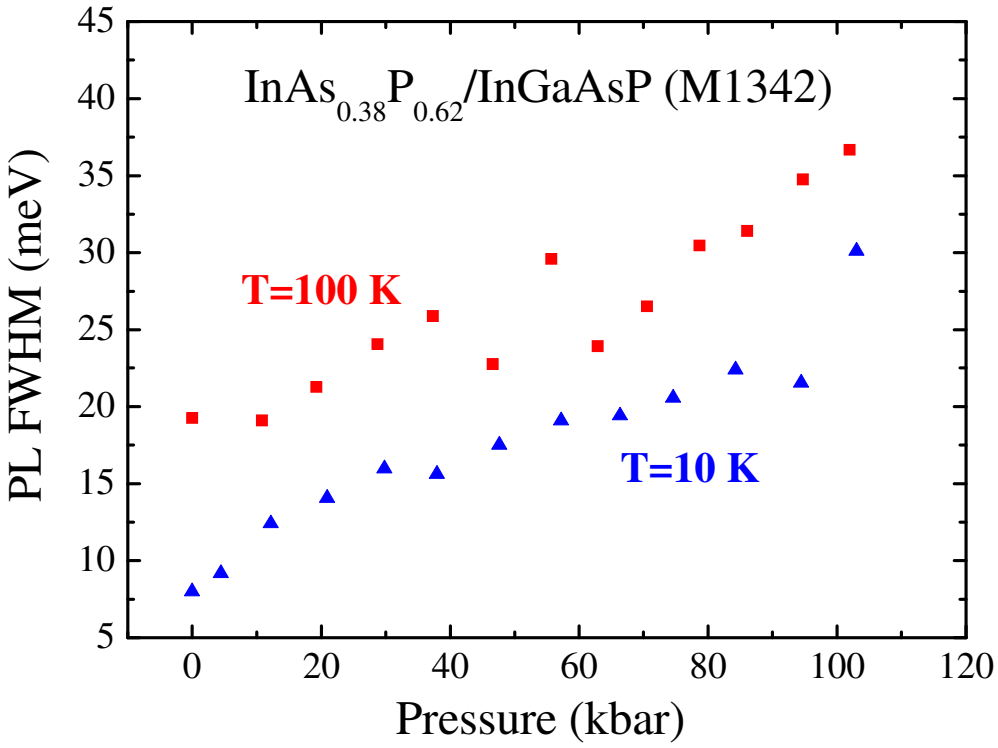

Fig. 70. Pressure dependence of the line width of the PL spectra of $InAs_{0.38}P_{0.62}$/InGaAsP (M1342) MQW

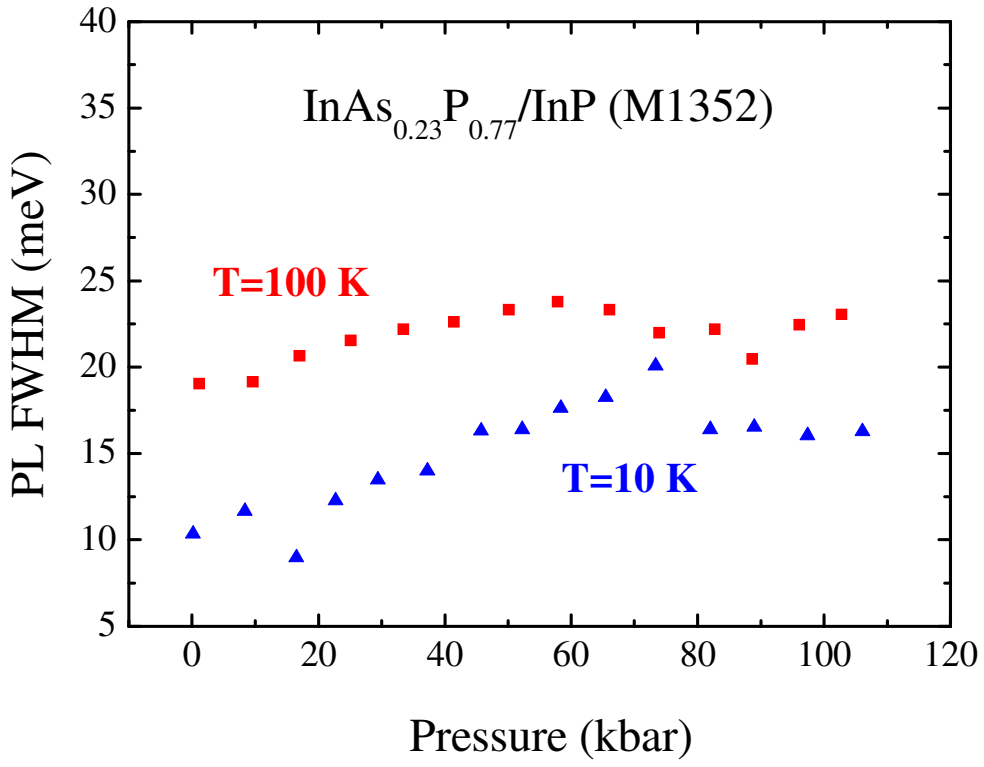

Fig. 71. Pressure dependence of the line width of the PL spectra of $InAs_{0.23}P_{0.77}$/InP (M1352) MQW.

Table 16. PL FWHM values of the MQWs compared to ruby at ambient and high pressures at T=10 K, 100 K.

Sample No.:	Average PL FWHM $(<\Gamma>_{PL\ FWHM})$ at ambient pressure, meV		Average PL FWHM $(<\Gamma>_{PL\ FWHM})$ at high pressures, meV	
	T=10 K	T=100 K	T=10 K	T=100 K
M1217	8.32	10.44	15.12	23.94
M1342	7.99	19.25	18.15	27.20
M1352	10.33	19.03	15.3	22.05
All MQWs (mean value)	8.88	16.24	16.19	24.4
Ruby	0.39	0.42	0.59 [a)]	0.56 [a)]

a) In the case of ruby the PL FWHM at T=100 K is smaller, than FWHM at T=10 K, as at high pressures the nonhydrostatic effects can be more significant at lower temperatures, than at higher ones.

In order to determine the real sensitivity gain of the InP-based pressure sensors compared to ruby gauges, one should calculate the figures of merit, defined by the following expression:

$$k = \frac{\left(\frac{dE}{dp}\right)_{MQWs}}{<\Gamma>_{PL\ FWHM\ MQWs}} \cdot \frac{<\Gamma>_{PL\ FWHM\ ruby}}{\left(\frac{dE}{dp}\right)_{ruby}} \quad (6.33)$$

The sensitivity gains obtained with the use of (6.33) formular for T=10 K and 100 K, for ambient and high pressures are presented in the Table 17.

As it follows from the Table 17, the proposed new pressure sensors appreciably exceed in sensitivity the commonly used ruby gauges throughout the entire temperature T=(10−100) K and pressure p=(0−100) kbar operating ranges.

Table 17. Sensitivity gains of the InP-based MQW pressure sensors comparably to the ruby gauges in different operating ranges.

Operating range of the pressure gauge	Ambient pressure		High pressures	
	T=10 K	T=100 K	T=10 K	T=100 K
Sensitivity gain	3.3	1.9	2.7	1.7

6.6. Conclusions II.

1. Three InP-based quantum structures – InAsP/InGaP, InAsP/InGaAsP and InAsP/InP with ambient-pressure PL peak positions at 0.887 eV (1398 nm), 1.023 eV (1212 nm) and 1.177 eV (1053 nm) respectively are proposed as possible pressure sensors for the diamond anvil cell.

2. The operating temperature range of the InP-based pressure gauges is (4–100) K. Temperature dependences of PL peak position of the $InAs_xP_{1-x}$ MQWs can be described by the expression (6.27), proposed by K.P.O'Donnel and X.Chen [169]. PL line width changes with temperature according to the exciton-phonon coupling model [172].

3. In the standard optical set-up for high-pressure measurements the operating laser power density range of the proposed pressure sensors is around (0.14÷1.6) kW/cm^2, which is characterized by negligibly small non-radiative emission mechanism of the $InAs_xP_{1-x}$-based quantum structures.

4. The calibration curve of all three proposed InP-based stress sensors can be described by the formula:

$$E(eV) = E_0 + 7.95 \cdot 10^{-3} p - 10^{-5} p^2,$$

where *E(eV)* is a peak position of the PL band and *p* is a pressure value, expressed in kbar. As the studied quantum structures were chosen randomly, the mentioned above dependence is seemed to be universal for any $InAs_xP_{1-x}$ MQWs with rather high range of accuracy (up to 97%).

5. The sensitivity of the proposed pressure sensors is around 2-3 times higher (dependently on the working temperature) than that of the ruby gauges.

7. SUMMARY

Recently Cr-doped II-VI semiconductors were studied intensively due to their wide potential application for the construction of the tunable laser sources, operable in the mid-infrared. Such lasers are expected to be widely used in medicine (ophthalmology, surgery), environmental diagnostics and coal-mining industry.

The results of the numerous studies have not spared the knowledge about II-VI Cr-doped materials some ambiguities (spin-orbit interaction intensity) and controversies (1.25 eV PL band nature in ZnSe:Cr). High-pressure PL technique was found to be a good tool to solve the mentioned above contradictory facts.

The peculiarities of the vibronic and spin-orbit interactions in II-VI Cr-doped semiconductors were investigated on the ZnX:Cr^{2+} (X=S, Se, Te) crystals. The anion type was found to be critical in the intensity of the spin-orbit interaction in compliance with the relation, based on the quantum-mechanical ideas: $\lambda \propto Z^4$ (where λ is a spin-orbit parameter and Z is the atomic number). This fact makes it possible to reconsider the previously published reports about the negligibly small spin-orbit interaction in ZnSe:Cr^{2+} crystals in comparison with ZnS:Cr^{2+} ones.

The nature of the 1.25 eV emission band in ZnSe:Cr^{2+} samples was a matter of the discussions in the literature, as the various experimental data led to the contradictory conclusions about its origin. The use of high-pressure photoluminescence technique has made it possible to claim unambiguously, that the near-infrared PL band, centered at ~1.25 eV is due to the intrashell $^3T_1 \rightarrow {}^5T_2$ transition of Cr^{2+} ion in ZnSe:Cr^{2+} crystals.

A significant factor, which prolonged and complicated high-pressure measurements in the near infrared was the lack of the proper pressure gauge, being operable in the same spectral range. InAsP MQWs were found to be the best candidates to be applied for this purpose. Apart from the higher sensitivity in comparison with traditionally used pressure sensor – ruby balls, InAsP MWQs are characterized with the common calibration curve for the samples with different InAs mole fractions x in the $InAs_xP_{1-x}$ MQWs. This makes it possible to consider the proposed sensor "tunable", as one can use the found calibration for the series of stress sensors, manufactured in compliance with the experimental needs, i. e. with an ambient-pressure band position of the studied sample.

Consequently, the presented in the Thesis experimental results enriched the knowledge about the energy structure of the Cr-doped II-VI semiconductor compounds. Furthermore, it

has been proposed the way, leading to the significant modernization of the high-stress experimental method via increase the accuracy and decrease the duration of the DAC-used high-pressure measurements in the infrared spectral range.

8. REFERENCES

[1] B.Jean and T.Bende *Springer Topics in Applied Physics* **89**, 141 (2003)

[2] I.T.Sorokina *Optical materials* **26**, 395 (2004)

[3] J.T.Vallin and G.D.Watkins *Phys. Rev. B* **9**, 2051 (1974)

[4] M.Kamińska, J.M.Baranowski, S.M.Uba, and J.T.Vallin *J. Phys. C: Solid State Phys.* **12**, 2197 (1979)

[5] J.T.Vallin, G.A.Slack, and S.Roberts, and A.E.Hughes *Phys. Rev. B* **2**, 4313 (1970)

[6] B.Nygren, J.T.Vallin, and G.A.Slack *Solid State Commun.* **11**, 35 (1972)

[7] J.S.Griffith, *The Theory of Transition-Metal Ions*. Cambridge University Press, Cambridge, 1961.

[8] S.Biernacki and H.-J.Schulz *Z. Phys. B* **65**, 429 (1987)

[9] J.C.Slater *Phys. Rev.* **165**, 655 (1968)

[10] L.A.Hemstreet and J.O.Dimmock *Phys. Rev. B* **20**, 1527 (1979)

[11] A.Fazzio, M.J.Caldas, and A.Zunger *Phys. Rev. B* **B30**, 3430 (1984)

[12] S.Sugano, Y.Tanabe, and H.Kamimura, *Multiplets of Transition Metal Ions in Crystals*. Academic, New York, 1970.

[13] M.Born and K.Huang, *Dynamical Theory of Crystal Lattices*. Clarendon Press, Oxford, 1951.

[14] M.Born and R.Oppenheimer *Ann. Phys.* **84**, 457 (1927)

[15] J.Garcia Sole, L.E.Bausa, and D.Jaque, *An Introduction to the Optical Spectroscopy of Inorganic Solids*. John Wilej and Sons, Ltd, 2005.

[16] I.B.Bersuker, *Stroenie i svoystva koordinatsionnykh soedineniy. (The Structure and Properties of the Coordination Compounds)*. Khimiya, Leningrad, 1971.

[17] L.D.Landau and E.M.Liphshitz, *Kvantovaya Mekhanika. Nerelativistskaya Teoriya. (Quantum mechanics. Nonrelativistic theory)*, Moscow, 1974.

[18] B.Henderson and G.F.Imbusch, *Optical Spectroscopy of Inorganic Solids*. Clarendon Press, Oxford, 1989.

[19] E.Wilson, G.Deshius, and P.Cross., *Teoriya kolebatel'nykh spektrov molekul. (The theory of the vibration spectra)*, Moscow, 1960.

[20] M.V.Volkenshtein, M.A.Yel'yashevich, and B.I.Stepanov, *Kolebaniya molekul. (Molecule vibrations)*. Gostekhteoretizdat, Moscow-Leningrad, 1949.

[21] E.Teller. *A historical note*, in: *The Jahn-Teller Effect in Molecules and Crystals*, Edited by R.Englman. London, 1972.

[22] H.A.Jahn and E.Teller *Proc. R. Soc. London, Ser. A* **161**, 220 (1937)

[23] H.A.Jahn *Proc. R. Soc. London, Ser. A* **164**, 117 (1938)

[24] I.B.Bersuker, *The Jahn-Teller Effect and Vibronic Interactions in Modern Chemistry*. Plenum Press, New York, 1984.

[25] I.B.Bersuker *Russian Chemical Review* **55**, 581 (1986)

[26] H.Bethe *Ann. Phys.* **3**, 194 (1929)

[27] J.H.Van Vleck *Phys. Rev.* **7**, 61, 72 (1939)

[28] U.Opik and M.H.L.Pryce *Proc. Roy. Soc.* **A238**, 425 (1957)

[29] A.D.Liehr and C.J.Ballhausen *Ann. Phys.* **3**, 304 (1958)

[30] I.B.Bersuker *Reports of the Academy of Sciences of the USSR* **132**, 587 (1960)

[31] I.B.Bersuker *Journal of Structure Chemistry* **2**, 350, 734 (1961)

[32] I.B.Bersuker, *Abstract of the Habilitation thesis*, 1964.

[33] I.B.Bersuker and V.Z.Polinger, *Vibronic Interactions in Molecules and Crystals*. Springer-Verlag Berlin Heidelberg, 1989.

[34] B.Beagley, A.Eriksson, J.Lindgren, I.Persson, L.G.M.Pettersson, M.Sandstrom, U.Wahlgren, and E.W.White *J. Phys. : Condens. Matter* **1**, 2395 (1989)

[35] W.Penney and R.Schlapp *Phys. Rev.* **41**, 194 (1932)

[36] W.Penney and R.Schlapp *Phys. Rev.* **43**, 486 (1933)

[37] J.H.Van Vleck *J. Chem. Phys.* **3**, 803, 807 (1935)

[38] A.Gołębiewski, *Elements of quantum mechanics and chemistry*. PWN, Warsaw, 1982.

[39] Brian N.Figgis and Michael A.Hitchman, *Ligand Field Theory and Its Applications*. Wiley-VCH, New York, 2000.

[40] E.Kondon and G.Shortly, *Teoriya atomnykh spektrov. (The Theory of the Atomic Spectra)*. Inostrannaya Literatura, Moscow, 1949.

[41] I.I.Sobelman, *Vvedenie v teoriu atomnykh spektrov (Introduction into the Theory of the Atomic Spectra)*. Fizmatgiz, Moscow, 1963.

[42] Y.Tanabe and S.Sugano *J. Phys. Soc. Japan* **9**, 753 (1954)

[43] S.Sugano, *Lecture Notes in Theory of Multiplets and Crystalls - Ligand Field Theory (Preprint)*, 1967.

[44] A.Twardowski, T.Fries, Y.Shapira, P.Eggenkamp, H.J.M.Swagten, and M.Demianiuk *J. Appl. Phys.* **73**, 5745 (1993)

[45] G.H.McCabe, Y.Shapira, V.Bindilatti, N.F.Oliveira, Jr, A.Twardowski, W.Mac, J.E.J.McNiff, and M.Demianiuk *Solid State Communications* **95**, 841 (1995)

[46] W.Mac, A.Twardowski, P.J.T.Eggenkamp, H.J.M.Swagten, Y.Shapira, and M.Demianiuk *Phys. Rev. B* **50**, 14144 (1994)

[47] W.Mac, A.Twardowski, M.E.J.Boonman, A.Wittlin, R.Krevet, M.von Ortenberg, and M.Demianiuk *Physica B* **211**, 384 (1995)

[48] Wojciech Mac, *Semimagnetic Semiconductors with Chromium, Ph.D. Thesis.* Physics Department of the University of Warsaw, 1996.

[49] A.Burger *et al* *Journal of Crystal Growth* **225**, 249 (2001)

[50] M.U.Lehr, B.Litzenburger, J.Kreiss, U.W.Pohl, H.R.Selber, H.-J.Schulz, A.Klimakow, and L.Worschech *J. Phys. : Condens. Matter* **9**, 753 (1997)

[51] Yu.F.Vaksman, V.V.Pavlov, Yu.A.Nitsuk, Yu.N.Purtov, A.S.Nasibov, and P.V.Shapkin *Fizika i tekhnika poluprovodnikov* **39** (2005)

[52] A.Abraham and B.Bleaney, *Electron paramagnetic resonance of transition metal ions*. Clarendon Press, Oxford, 1970.

[53] M.Herbich, W.Mac, A.Twardowski, K.Ando, Y.Shapira, and M.Demianiuk *Phys. Rev. B* **58**, 1912 (1998)

[54] W.Mac, A.Twardowski, and M.Demianiuk *Phys. Rev. B* **54**, 5528 (1996)

[55] F.S.Ham *Phys. Rev.* **138**, A1727 (1965)

[56] F.S.Ham *Phys. Rev.* **166**, 307 (1968)

[57] G.Grebe and H.-J.Schulz *Z. Naturforsch. Teil A* **29**, 1803 (1974)

[58] G.Grebe, G.Roussos, and H.-J.Schulz *J. Lumin.* **12/13**, 701 (1976)

[59] A.L.Natadze and A.I.Ryski *Solid State Communications* **24**, 147 (1977)

[60] A.I.Belogorokhov, M.I.Kulakov, V.A.Kremerman, A.L.Natadze, Yu.B.Rozenfeld, and A.I.Ryskin *Zh. Eksp. Teor. Fiz. (Journ. of Exper. and Theor. Phys.)* **94**, 174 (1988)

[61] V.A.Kremerman, V.P.Kuznetsov, Yu.B.Rozenfeld, and A.I.Ryskin *Opt. Spektroskop.* **61**, 201 (1986)

[62] E.U.Condon and G.H.Shortley, *The Theory of Atomic Spectra*. University Press, Cambridge, 1953.

[63] J.T.Vallin and G.D.Watkins *Solid State Communications* **9**, 953 (1971)

[64] J.T.Vallin and G.D.Watkins *Phys. Rev. Letters* **37A**, 297 (1971)

[65] R.N.Bhargava *Optoelectron. Dev. Technol.* **7(1)**, 19 (1992)

[66] S.Shionoya and H.Kobayashi. H.Ulchiike, in: Electroluminescence Proceedings of the Fourth International Workshop. Berlin, 1989, p. 238.

[67] S.Taniguchi, T.Hino, S.Itoh, K.Nakano, N.Nakayama, A.Ishibashi, and M.Ikeda *Electron Lett.* **32**, 552 (1996)

[68] A. Zunger, in: Solid State Physics, vol. 89. New York, 1986, p. 275.

[69] J.T.Vallin, G.A.Slack, S.Roberts, and A.E.Hughes *Solid State Communications* **7**, 1211 (1969)

[70] G.Goetz, H.Zimmermann, and H.-J.Schulz *Z. Phys. B.* **91**, 429 (1993)

[71] A.E.Hughes and J.T.Vallin. Unpublished data. See also Ref. [40].

[72] C.Stuart Kelley *J. Chem. Phys.* **59**, 5737 (1973)

[73] T.H.Keil *Phys. Rev.* **140**, A601 (1965)

[74] J.W.Allen, *Deep centers in semiconductors. A state of the art approach.*, New York, 1986.

[75] Ming Luo, B.L.VanMil, R.P.Tompkins, T.H.Myers, and N.C.Giles *J. Appl. Phys.* **97**, 013518 (2005)

[76] J.M.Baranowski and P.Vogl *Proc. Conf. Physics 6. 12th Conf. Physcis Semiconducting Compounds, Jaszowiec*, 74 (1983)

[77] S.W.Biernacki and H.-J.Schulz *Phys. Status Solidi* **B103**, K163 (1981)

[78] D.W.Palmer, www.semiconductors.co.uk, last updated: 03, 2008.

[79] D.Long, *Energy Bands in Semiconductors*. Interscience, 1968.

[80] V.Yu.Ivanov, A.A.Shagov, A.Szczerbakow, and M.Godlewski *Physica B* **308-310**, 942 (2001)

[81] S.Bhaskar, P.S.Dobal, B.K.Rai, R.S.Katiyar, H.D.Bist, J.-O.Ndap, and A.Burger *J. Appl. Phys.* **85**, 439 (1999)

[82] H.Pradella and U.W.Pohl *Phys. Status Solidi (b)* **141**, K143 (1987)

[83] M.U.Lehr, B.Litzenburger, J.Kreissl, U.W.Pohl, H.R.Selber, H.-J.Schulz, A.Klimakow, and L.Worschech *J. Phys. : Condens. Matter* **9**, 753 (1997)

[84] M.Godlewski and M.Kaminska *J. Phys. C* **13**, 6537 (1980)

[85] T.Suski and W.Paul, *High Pressure in Semiconductor Physics I*. Academic Press, San Diego, USA, 1998.

[86] G.Bastard, J.A.Brum, and R.Ferreira, *Solid State Physics*. Academic Press, San Diego, 1991.

[87] M.Altarelli, *Heterojunctions and Semiconductors Superlattices*. Springer, Heidelberg, 1985.

[88] A.R.Goni, K.Syassen, Y.Zhang, K.Ploog, A.Cantarero, and A.Cros *Phys. Rev. B* **45**, 6809 (1992)

[89] D.J.Wolford, T.F.Kuech, J.A.Bradley, M.A.Gell, .Ninno, and M.Jaros *J. Vac. Sci. Technol. B* **4**, 1043 (1986)

[90] J.C.Maan *Surf. Sci.* **196**, 518 (1988)

[91] L.M.Claessen, J.C.Maan, M.Altarelli, P.Wyder, L.L.Chang, and L.Esaki *Phys. Rev. Lett.* **57**, 2556 (1986)

[92] H.M.Cheong, W.Paul, M.E.Flatte, and R.H.Miles *Phys. Rev. B* **55**, 4477 (1997)

[93] A.Jayaraman *Reviews of Modern Physics* **55**, 65 (1983)

[94] H.G.Drickamer *Solid-State Physics* **17**, 1 (1965)

[95] H.G.Drickamer *Solid-State Physics* **19**, 135 (1966)

[96] J.C.Jamieson, A.W.Lawson, and N.D.Nachtrieb *Rev. Sci. Instrum.* **30**, 1016 (1959)

[97] C.E.Weir, E.R.Lippincott, A.Van Valkenburg, and E.N.Bunting *J. Res. Natl. Bur. Stand. , Sec. A* **63**, 55 (1959)

[98] J.Xu, H.K.Mao, and P.M.Bell *Science* **232**, 1404 (1986)

[99] J.Xu, H.K.Mao, and P.M.Bell *Acta Physica Sinica* **36**, 501 (1986)

[100] Ji-an Xu, *Science and Technology of New Diamond*. KTK Scientific Publishers/Terra Scientific Publishing Company, 1990.

[101] http://www.diamond.ac.uk, last updated: 11, 2009.

[102] D.J.Dunstan and I.L.Spain *J. Phys. E:Sci. Instrum.* **22**, 913 (1989)

[103] G.J.Piermarini, S.Block, and J.S.Barnett *J. Appl. Phys.* **44**, 5377 (1973)

[104] I.Fujishiro, G.J.Piermarini, S.Block, and R.G.Munro, *Hight Pressure in Research and Industry, Proceedings of the 8th AIRAPT Conference Uppsala*. ISBN, Sweden, 1982.

[105] D.H.Liebenberg, R.L.Mills, and J.C.Bronson, *High Pressure Science and Technology*. Plenum, New York, 1979.

[106] H.K.Mao and P.M.Bell *Science* **203**, 1004 (1979)

[107] M.Nicol, K.R.Hirsch, and W.B.Holzapfel *Chem. Phys. Lett.* **68**, 49 (1979)

[108] P.M.Bell and H.K.Mao, *Carnegie Institution of Washington Year Book*, 1975.

[109] R.LeSar, S.A.Ekberg, L.H.Jones, R.L.Mills, L.A.Schwalbe, and D.Schiferl *Solid State Communications* **32**, 131 (1979)

[110] I.L.Spain and D.J.Dunstan *J. Phys. E:Sci. Instrum.* **22**, 923 (1989)

[111] http://encyclopedia.airliquide.com, last updated: 2009.

[112] A.Kaminska, *High Pressure Studies of the Chromium Impurity Electron Structure in Laser Materials, Ph.D. Thesis*. IF PAS, Warsaw, 2001.

[113] H.Hua and Y.K.Vohra *Appl. Phys. Let.* **71**, 2602 (1997)

[114] R.A.Forman, G.J.Piermarini, J.D.Barnett, and S.Block *Science* **176**, 284 (1972)

[115] G.J.Piermarini, S.Block, J.D.Barnett, and R.A.Forman *J. Appl. Phys.* **46**, 2774 (1975)

[116] R.A.Noack and W.B.Holzapfel, *High Pressure Science and Technology*. Plenum, New York, 1979.

[117] B.A.Weinstein *Rev. Sci. Instrum.* **57**, 910 (1979)

[118] H.E.King Jr and .T.Prewitt *Rev. Sci. Instrum.* **51**, 1037 (1980)

[119] H.K.Mao and P.M.Bell *Science* **191**, 851 (1976)

[120] H.K.Mao and P.M.Bell *Science* **200**, 1145 (1978)

[121] A.Lacam and C.Chateau *J. Appl. Phys.* **66**, 366 (1989)

[122] H.Arashi and M.Ishigame *Jpn. J. Appl. Phys.* **21**, 1647 (1982)

[123] N.J.Hess and G.J.Exarhos *High Pressure Research* **2**, 57 (1989)

[124] Y.Chi, S.Liu, W.Shen, L.Wang, and G.Zou *Physica* **139&140B**, 555 (1986)

[125] Y.Chi, S.Liu, Q.Wang, L.Wang, and G.Zou *High Pressure Research* **3**, 150 (1990)

[126] Y.R.Shen, T.Gregorian, and W.B.Holzaphel *High Pressure Research* **5**, 73 (1991)

[127] J.D.Barnett, S.Block, and G.J.Piermarini *Rev. Sci. Instrum.* **44**, 1 (1973)

[128] S.Kobyakov, A.Kamicska, A.Suchocki, D.Galanciak, and M.Malinowski *Appl. Phys. Lett.* **88**, 234102 (2006)

[129] H.Muller, R.Trommer, and M.Cardona *Phys. Rev. B* **21**, 4879 (1980)

[130] T.Kobayashi, T.Tei, K.Aoki, K.Yamamoto, and K.Abe, *Physics on Solids under Pressure*. North-Holland, Amsterdam, 1981.

[131] K.Kobayashi, T.Tei, K.Aoki, K.Yamamoto, and K.Abe *J. Lumin.* **24/25**, 347 (1981)

[132] C.S.Menoni, H.D.Hochheimer, and I.L.Spain *Phys. Rev. B* **33**, 5896 (1986)

[133] S.W.Tozer, D.J.Wolford, J.A.Bradley, D.Bour, and G.B.Stringfellow, *Proc. of the 19th Int. Conf. on Phys. of Semicond.* Institute of Physics, PAS, Warsaw, 1988.

[134] W.Trzeciakowski, P.Perlin, H.Teisseyre, C.A.Mendonca, M.Micovic, P.Ciepielewski, and E.Kamicska *Sensors and Actuators A* **32**, 632 (1992)

[135] U.Venkateswaran, M.Chandrasekhar, H.R.Chandrasekhar, B.A.Vojak, F.A.Chambers, and J.M.Meese *Phys. Rev. B* **33**, 8416 (1986)

[136] P.Perlin, W.Trzeciakowski, E.Litwin-Staszewska, J.Muszalski, and M.Micovic *Semicond. Science and Technology* **9**, 2239 (1994)

[137] T.P.Sosin, W.Trzeciakowski, P.Stкpicski, and M.Hopkinson, *Proceedings of the Joint XV AIRAPT&XXXIII EHPRG Int.Conf., Warsaw, Poland, September 11-15, 1995.*, Warsaw, 1995.

[138] K.Graham, S.Mirov, V.Fedorov, M.E.Zvanut, A.Avanesov, V.Badikov, B.Ignat'ev, V.Panutin, and G.Shevirdyaeva, *OSA Trends in Optics and Photonics on Advanced Solid-State Lasers.* Optical Society of America, Washington DC, 2001.

[139] Abebe Belay and A.V.Gholap *International Journal of Physical Sciences* **4**, 722 (2010)

[140] L.D.DeLoach, R.H.Page, G.D.Wilke, S.A.Payne, and W.F.Krupke *IEEE J. Quantum Electron.* **32**, 885 (1996)

[141] G.Karczewski, M.Sawicki, V.Ivanov, C.Ruester, G.Grabecki, F.Macukura, L.W.Molenkamp, and D.Dietl *Journal of Supeconductivity: Incorporating Novel Magnetism* **16**, 55 (2003)

[142] R.Valiente and F.Rodriguez *J. Phys. : Condens. Matter* **10**, 9525 (1998)

[143] F.D.Murnaghan *Proc. Nation. Acad. Sci.* **30**, 244 (1944)

[144] M.Rabah, B.Abbar, Y.Al-Douri, B.Bouhafs, and B.Sahraoui *Mater. Sci. Eng. B* **100**, 163 (2003)

[145] R.G.Greene, H.Luo, and A.L.Ruoff *J. Phys. Chem. Solids* **56**, 521 (1995)

[146] C.K.Jorgensen *Progr. Inorg. Chem.* **4**, 73 (1962)

[147] S.W.Biernacki, A.Kamicska, A.Suchocki, and L.Arizmendi *Appl. Phys. Lett.* **81**, 442 (2002)

[148] K.Świątek, M.Godlewski, and T.P.Surkova *Phys. Status Solidi c* **1**, 281 (2004)

[149] K.Mahofer, K.Hochberger, and W.Gebhardt *J. Phys. C:Solid State Phys.* **21**, 4393 (1988)

[150] S.Trushkin, S.W.Biernacki, Le Van Khoi, A.Kamicska, and A.Suchocki *New Journal of Physics* **10**, 013023 (2008)

[151] H.Watanabe, *Operator Methods in Ligand Field Theory*. Prentice-Hall, Englewood Cliffs, NJ, 1966.

[152] W.A.Harrison, *Electronic Structure and the Properties of Solids*. Freeman, San Francisco, 1980.

[153] C.Froese-Fischer *At. Data* **4**, 301 (1972)

[154] Zhi-Biao Hao, Zai-Yuan Ren, Bing Xiong, Wen-Ping Guo, and Yi Luo *Journal of Crystal Growth* **234**, 364 (2002)

[155] Meng Cao, Hui-Zhen Wu, Yan-Feng Lao, Chun-Fang Cao, Cheng Liu, and Gu-Jin Hu *Journal of Alloys and Compounds* **491**, 595 (2010)

[156] H.P.Lei, H.Z.Wu, Y.F.Lao, M.Qi, A.Z.Li, and W.Z.Shen *Journal of Crystal Growth* **256**, 96 (2003)

[157] M.Fox, *Optical Properties of Solids*. Oxford University Press, Oxford, New York, 2003.

[158] Mark Fox, *Optical Properties of Solids*. Oxford University Press, New York, 2003.

[159] R.Y.-F.Yip, Aït-Ouali, A.Bensaada, P.Desjardins, M.Beaudoin, L.Isnard, J.L.Brebner, J.F.Currie, and R.A.Masut *J. Appl. Phys.* **81** (1997)

[160] L.Vegard *Zeitschrift fur Physik* **5**, 17 (1921)

[161] A.R.Denton and N.W.Ashcroft *Phys. Rev. A* **43**, 3161 (1991)

[162] C.Kittel, *Introduction to Solid State Physics, 6th Ed.* John Wiley, New York, 1986.

[163] G.A.Antypas and T.O.Yep *J. Appl. Phys.* **42**, 3201 (1971)

[164] M.Wada, S.Araki, T.Kudou, T.Umezawa, and S.Nakajima *Appl. Phys. Lett.* **76**, 2722 (2000)

[165] Y.P.Varshni *Physica* **34**, 149 (1967)

[166] S.M.Sze, *Semiconductor devices*, New York, 1985.

[167] Jacques I.Pankove, *Optical processes in semiconductors*. Dover, New York, 1975.

[168] Z.M.Fang, K.Y.Ma, D.H.Jaw, R.M.Cohen, and G.B.Stringfellow *J. Appl. Phys.* **67**, 7034 (1990)

[169] K.P.O'Donnel and X.Chen *Appl. Phys. Lett.* **58**, 2924 (1991)

[170] L.M.Woods, P.Silvestre, P.Thiagarajan, G.A.Patrizi, G.Y.Robinson, K.M.Jones, and M.AL.Jassim *J. Electron. Mater.* **23**, 1229 (1994)

[171] A.Venu Gopal, Rajesh Kumar, A.S.Venguriekar, A.Bosacchi, S.Franch, and L.N.Pfeiffer *J. Appl. Phys.* **87**, 1858 (2000)

[172] T.Takeuchi, S.Sota, M.Katsuragawa, and M.Komori *Jpn. J. Appl. Phys.* **Part 26**, L382 (1997)

[173] The Landolt-Bornstein Database, www.springermaterials.com, last updated: 2010.

[174] I.E.Itskevich, M.Henini, H.A.Carmona, L.Eaves, and P.C.Main *Appl. Phys. Lett.* **70**, 505 (1997)

[175] B.S.Ma, X.D.Wang, F.H.Su, Z.L.Fang, K.Ding, Z.C.Niu, and G.H.Li *J. Appl. Phys.* **95**, 933 (2004)

[176] M.D.Frogley, J.R.Downes, and D.J.Dunstan *Phys. Rev. B* **62**, 13612 (2000)

[177] J.R.P.Schneider and B.W.Wessels *J. Electron. Mater.* **20** (1991)

SCIENTIFIC ACTIVITY throughout Thesis preparation

Publications

1. **S. Trushkin**, S.W. Biernacki, Le Van Khoi, and A.Suchocki, ***"High pressure study of ZnSe:Cr^{2+} crystals: the origin of the 1.25 eV luminescence"***, J.Phys.: Condens. Matter 19 096213 (2007).

2. V. Khranovskyy, R. Minikayev, **S. Trushkin**, G. Lashkarev, V. Lazorenko, U. Grossner, W. Paszkowicz, A. Suchocki, B.G. Svensson and R. Yakimova, ***"Improvement of ZnO thin film properties by application of ZnO buffer layers"***, Journal of Crystal Growth, **308**, 93–98 (2007).

3. A. Kamińska**,** A. Mycielski, **S. Trushkin**, A. Suchocki*,* ***"ZnO crystals obtained with the chemical vapour transport method – properties and applications"***, Tishreen University Journal for Studies and Scientific Research, **29**, 89 (2007).

4. **S. Trushkin**, S. W. Biernacki, Le Van Khoi, A. Kamińska and A. Suchocki ***"High pressure luminescence of ZnTe:Cr^{2+} crystals"***, New Journal of Physics, **10**, 013023 (2008).

5. A. Kamińska, A. Kozanecki, **S. Trushkin**, A. Suchocki ***„Spectroscopy of ytterbium-doped InP under high hydrostatic pressure"***, Phys. Rev. B, **81,** 165209 (2010).

Poster Presentations and Talks

1. **S. Trushkin**, A. Mycielski, A. Kamińska, K. Świątek, and A. Suchocki ***"Influence of Oxygen Annealing on Optical and Electrical Properties of ZnO Crystals Grown by CVT"*** (poster presentation) – XXXIII International School on the Physics of Semiconducting Compounds "Jaszowiec 2004", May 28 – June 4, 2004, Jaszowiec, Poland.

2. **S. Trushkin**, K. Grasza, A. Mycielski, A. Kamińska, K. Świątek, P. Kaczor, A. Barcz, A. Suchocki ***"Electrical and optical properties of ZnO and ZnO:Cr crystals, grown by CVT method"*** (poster presentation) – EMRS Fall Meeting, September, 6 – 10, 2004 Warsaw, Poland.

3. A. Kamińska**,** A. Mycielski, **S. Trushkin**, A. Suchocki ***"ZnO crystals obtained with the chemical vapour transport method – properties and applications"*** (invited lecture delivered by A. Kamińska) – The 2nd Workshop on Physics of Semiconductor Science, April, 24 – 26, 2005, Lattakia, Syria.

4. **S. Trushkin**, A. Mycielski, A. Kamińska, P. Kaczor, and A. Suchocki ***"Optical properties of ZnO crystals, grown by chemical vapour transport method"*** (poster presentation) – XXXIV International School on the Physics of Semiconducting Compounds "Jaszowiec 2005", June 4 – 10, 2005, Jaszowiec, Poland.

5. **S. Trushkin**, Le Van Khoi, S. Biernacki, A. Kamińska, and A. Suchocki ***"High pressure luminescence studies of ZnSe:Cr^{2+} crystals"*** (poster presentation) – XXXIV International School on the Physics of Semiconducting Compounds "Jaszowiec 2005", June 4 – 10, 2005, Jaszowiec, Poland.

6. **S. Trushkin**, Le Van Khoi, S. Biernacki, A. Kamińska, and A. Suchocki ***"High-Pressure Luminescence Studies of the d^4 Intrashell Transitions of Cr^{2+} in ZnSe:Cr Crystals"*** (poster presentation) – EMRS Spring Meeting 2006, Strasbourg, France.

7. **S. Trushkin**, Le Van Khoi, S. Biernacki, A. Kamińska, and A. Suchocki ***"Nephelauxetic Effect in Zn(Se,S):Cr^{2+} Crystals"*** (poster presentation) – XXXV International School on the Physics of Semiconducting Compounds "Jaszowiec 2006", June 17 – 23, 2006, Jaszowiec, Poland.

8. **S. Trushkin**, Le Van Khoi, S. Biernacki, A. Kamińska, and A. Suchocki ***"High-Pressure Luminescence Studies of Intrashell Transitions of Cr^{2+} Ions in ZnSe:Cr Crystals"*** (poster presentation) – ICPS-28, July 24 – 28, 2006, Vienna, Austria.

9. **S. Trushkin**, Le Van Khoi, S. Biernacki, A. Kamińska, and A. Suchocki ***"High-Pressure Photoluminescence Technique and its Application for the Studies of Intrashell Transitions in ZnSe:Cr Crystals"*** – (invited oral presentation) – Seminar in the Institute of Photonics, Technical University of Wienna, October 24th, 2006, Vienna, Austria.

10. **Trushkin**, I.T. Sorokina, E. Sorokin, S. Biernacki, and A. Suchocki ***"High-Pressure Studies of Jahn-Teller effect in ZnS:Cr^{2+} crystals"*** – (poster presentation) – XXXVI International School on the Physics of Semiconducting Compounds "Jaszowiec 2007", June 9 – 15, 2007 Jaszowiec, Poland.

11. **S. Trushkin,** W. Trzeciakowski, M. Hopkinson, A. Kamińska, and A. Suchocki ***"Calibration of New High-Pressure Sensors Based on InAsP/InP Heterostructures"*** (poster presentation) – XXXVII International School on the Physics of Semiconducting Compounds "Jaszowiec 2008", June 7 – 13, 2008, Jaszowiec, Poland.

12. D. Galanciak, A. Kamińska, **S. Trushkin**, A. Suchocki ***"High Pressure Spectroscopy of $LiNbO_3$ and $Y_3Al_5O_{12}$ (YAG) Crystals Doped with Nd^{3+} Ions"*** (poster presentation) – The Second International Workshop on Advanced Spectroscopy and Optical Materials, July 13–17, 2008, Gdańsk, Poland.

13. **S. Trushkin,** S. Biernacki, I.T. Sorokina, Ye. Sorokin, Le Van Khoi, and A. Suchocki ***"High-Pressure Photoluminescence Studies of ZnS, ZnSe, ZnTe Crystals, Doped With Cr^{2+} Ions"*** (oral presentation) – 13th International Conference on High Pressure Semiconductor Physics (HPSP-13), July 22 – 25, 2008, Fortaleza, Ceara, Brazil.

14. **S. Trushkin,** M.G. Brik, S. Biernacki, L.V. Khoi, I.T. Sorokina, E. Sorokin, A. Kamińska, and A. Suchocki ***"Ligand Influence on Jahn-Teller Effect and Spin-Orbit Interaction, Studied in II-VI Semiconductors Doped with Cr^{2+} Ions"*** (poster presentation) – XXXVIII International School&Conference on the Physics of Semiconductors "Jaszowiec 2009", June 19 – 26, Krynica-Zdrój, Poland.